学位論文

A Study on Ningaloo Niño

(ニンガルー・ニーニョに関する研究)

平成 26 年 12 月 博士 (理学) 申請

東京大学大学院理学系研究科

地球惑星科学専攻

片岡 崇人

Abstract

Sea surface temperature (SST) along the west coast of Australia undergoes large interannual variations. After unprecedented SST warming in austral summer of 2010/11, the phenomenon was named “Ningaloo Niño”. Although this phenomenon has devastating impacts on the regional marine ecosystem, studies on Ningaloo Niño have just begun and there is no systematic understanding of its mechanism. This thesis is devoted to quantitative understanding of generation and decay mechanisms of Ningaloo Niño.

From observational data analysis, it is found that Ningaloo Niño (Niña), which is associated with positive (negative) SST anomalies and atmospheric anomalies off Western Australia, reaches its peak during austral summer. Ningaloo Niño (Niña) events are classified into locally amplified and non-locally amplified cases. The former develops through an intrinsic unstable ocean-atmosphere interaction off Western Australia. Anomalously warm (cool) SSTs generate negative (positive) sea level pressure (SLP) anomalies that accompany northerly (southerly) alongshore wind anomalies. These cause anomalous coastal downwelling (upwelling) and stronger (weaker) southward warm advection, further enhancing the initial SST anomalies. This positive feedback loop is named as the coastal Bjerknes feedback. For the latter case, positive (negative) SST anomalies are induced by coastally-trapped downwelling (upwelling) waves, which are generated by wind anomalies in the western Pacific associated with La Niña (El Niño), or alongshore wind anomalies in the northern coast of Australia.

Warmer (cooler) SSTs in both cases are associated with negative (positive) SLP anomalies off Western Australia. The SLP anomalies in the locally amplified case show a cell-like pattern and have a sharp cross-shore pressure gradient along the west coast of Australia. On the other hand, those in the non-locally amplified case tend to show a zonally elongated pattern. The difference is related to the continental SLP modulated by the Australian summer monsoon. It is also suggested that the Ningaloo Niño/Niña has significant impacts on the precipitation over Australia.

The calculation of mixed-layer temperature (MLT) balance using outputs from an ocean general circulation model reveals that positive meridional advection anomalies associated with the stronger Leeuwin Current and enhanced warming by climatological shortwave radiation owing to anomalously shallow mixed layer contribute to the growth of positive SST anomalies in the near-shore region of both cases for Ningaloo Niño. On the other hand, larger sensible heat flux loss plays an important role in the decay. Since the strengthened meridional current during the developing season weakens meridional temperature gradient, meridional advection anomalies eventually change their sign and contribute to the decay as well.

Positive (Negative) MLT tendency anomalies in the offshore region for both cases are generated by enhanced (suppressed) warming by the climatological shortwave radiation owing to negative (positive) mixed layer depth anomalies during the development (decay) phase.

The generation and decay mechanisms for both cases of Ningaloo Niña are generally close to a mirror image of those for Ningaloo Niño. In particular, negative meridional advection anomalies associated with the weaker Leeuwin Current, and reduced warming by the climatological shortwave radiation play an important role in the near-shore and offshore region, respectively.

Since negative (positive) SLP anomalies off Western Australia are crucial for the

Ningaloo Niño (Niña) development, a series of an atmospheric general circulation model experiments are conducted to investigate the generation mechanisms of atmospheric circulation anomalies accompanied by Ningaloo Niño/Niña. Even when interannual SST anomalies are imposed only in the eastern South Indian Ocean, negative (positive) SLP anomalies are formed off Western Australia in Ningaloo Niño (Niña) years, supporting the existence of the local ocean-atmosphere interaction. Negative (positive) SLP anomalies are also generated in Ningaloo Niño (Niña) years owing to a Matsuno-Gill type response to diabatic heating anomalies in the western tropical Pacific when the model is forced with SST anomalies outside of the southeastern Indian Ocean. Regarding climatic impacts, it is found that even when SST anomalies outside of the eastern South Indian Ocean are removed, wet (dry) conditions are induced over the northwestern part of Australia associated with Ningaloo Niño (Niña).

Finally, to check whether Ningaloo Niño/Niña can develop independent of El Niño/Southern Oscillation (ENSO), a coupled model experiment in which SSTs in the tropical Pacific and maritime continent are strongly relaxed to their daily climatology to suppress ENSO is conducted. It is shown that Ningaloo Niño/Niña develops with the similar magnitude without ENSO through an intrinsic ocean-atmosphere interaction off Western Australia.

Acknowledgments

I am most indebted to the supervisor, Tomoki Tozuka. This thesis would not have been completed without his patient guidance and ceaseless encouragement. Deep gratitude should also be expressed to Toshio Yamagata, who was the adviser during my master's program, for sharing his ideas and for helpful discussions. He has kindly continued to work with me even after his retirement from UT. It has been an honor to be Dr. Tozuka's first and Prof. Yamagata's last student.

I would like to thank the members of my dissertation committee, Toshiyuki Hibiya, Ichiro Yasuda, Hisashi Nakamura, and Yukio Masumoto for their time and helpful comments. I am particularly indebted to Shang-Ping Xie, Sébastien Masson, Yu Kosaka, and Takeshi Izumo for their warm guidance and hospitality during (and even after) my research interns at LOCEAN and Scripps Institution of Oceanography. This study benefited from discussions with Swadhin Behera, Youichi Tanimoto, Shoshiro Minobe, Humio Mitsudera, Atsushi Kubokawa, Takeshi Horinouchi, Masaru Inatsu, Yutaka Yoshikawa, Ping Chang, B. N. Goswami, Hiroaki Miura, Takafumi Miyasaka, and Takeshi Doi. Thanks also to Yoshihiro Niwa, Michio Watanabe, Yuki Tanaka, Pascal Oettli, Takaaki Yokoi, Chaoxia Yuan, Yushi Morioka, Taira Nagai, Takashi Ijichi, Yohei Onuki, Shun Ohishi, Yoko Yamagami, Tsubasa Kohyama, Tamaki Suematsu, Chia-Rui Ong, Satoru Endo, Chiho Tanizaki, Junko Moriyama, and all past and present members of the Oceanic and Atmospheric Sciences Group for their valuable comments, encouragement, and help. I am also grateful to the members of Xie group

and the staff at LOCEAN and Scripps for their hospitality during my visits.

I would like to acknowledge the funding sources. I was supported by the Sasakawa Scientific Research Grant from the Japan Science Society, Research Fellowship of Japan Society for the Promotion of Science (JSPS) for Young Scientists, and the Program for Leading Graduate Schools, MEXT, Japan.

Finally, I wish to thank my family who supported me in all my pursuits. Words cannot express my gratitude to my parents, brother, and late grandmothers for all their warm support, encouragement, and understanding.

Contents

Chapter 1

General introduction

1.1 Is Indian Ocean a passive ocean basin?

One of the most prominent features in the tropical Indian Ocean is its strong seasonal variation; the Asian continent drives the strongest monsoon in the world (e.g. Schott et al., 2009). Because of the monsoonal winds, zonal winds reverse their direction during the course of the year (Ogata and Xie, 2011). As a result, unlike in the tropical Pacific and Atlantic Oceans, easterly trade winds do not prevail on the annual mean so that the thermocline is relatively deep.

On interannual time scales, sea surface temperature (SST) variation in the tropical Indian Ocean is dominated by a basin-wide warming or cooling as shown in Fig. 1.1a. This basin-wide SST variation, now called the Indian Ocean basin mode(Yang et al., 2007) , typically follows and shows a high correlation with El Niño/Southern Oscillation (ENSO) in the Pacific (Fig. 1.1b; Cadet, 1985; Nigam and Shen, 1993). In fact, much of this warming/cooling can be explained by surface heat flux anomalies associated with ENSO (Klein et al., 1999).

These earlier studies gave an impression that the tropical Indian Ocean is inactive in terms of air-sea interaction and this view had been widely accepted until recently. The discovery of the Indian Ocean Dipole (IOD; Saji et al., 1999), however, marked a turning point for the Indian Ocean research. This phenomenon is characterized by a dipole pattern in SST anomaly field with negative (positive) SST anomalies off Sumatra (in the western tropical Indian Ocean) (Fig. 1.2a). Associated with negative SST anomalies, there is a divergence in the lower troposphere. On the other hand, winds in the lower troposphere converge over the anomalously warm SST in the western part resulting in easterly wind anomalies in the tropics. These anomalous easterlies cause coastal and equatorial upwelling anomalies off Sumatra and along the equator, respectively, both of which enhance the initial

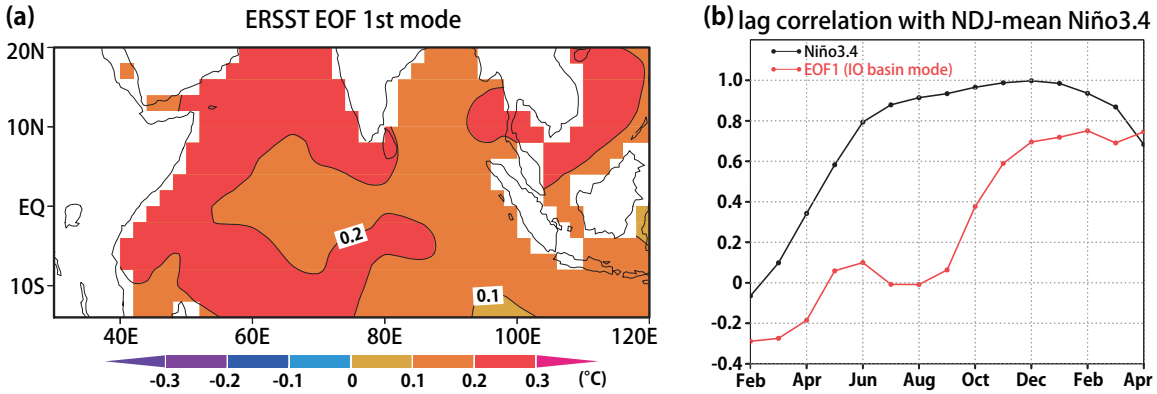

Fig. 1.1 (a) First EOF mode (EOF1) of SST anomalies in the tropical Indian Ocean (40°E-120°E, 15°S-20°N). (b) Lag correlation of Niño3.4 index (black) and the principal component of EOF1 (red) with November-January averaged Niño3.4 index. Niño3.4 index is defined as the area-average of SST anomalies over the region 170°W-120°W, 5°S-5°N. The ERSST version 3b (Smith et al., 2008) for the period of 1950-2011 is used with a linear trend removed.

negative SST anomalies in the east (thermocline feedback). In the western part, on the other hand, easterly wind anomalies pile up surface warm waters and deepen the thermocline. As a result, warm SST anomalies are further enhanced. This positive ocean-atmosphere interaction loop is referred to as the Bjerknes feedback (Bjerknes, 1969; Philander et al., 1984; Yamagata, 1985; Yamagata et al., 2004). In addition to the vertical processes, anomalous horizontal advection contributes as well (zonal advective feedback; e.g. Gill, 1985; Hirst, 1986; Horii et al., 2009). The Bjerknes feedback owes its existence to the change in the sign of the Coriolis parameter across the equator, which acts like a "wall" so that the virtual "wall" traps energy along the equator. Figure 1.2b shows composites of equatorial zonal wind anomalies and the Dipole Mode Index, the latter being a representative of the strength of SST anomalies associated with the IOD. Local ocean-atmosphere coupling in the tropical Indian Ocean is evident from the co-variability of these two indices. Since some IODs did not co-occur with ENSO, the IOD is considered as an intrinsic ocean-atmosphere coupled mode in the tropical Indian Ocean (Yamagata et al., 2003; Saji and Yamagata, 2003b). Behera et al. (2006) further

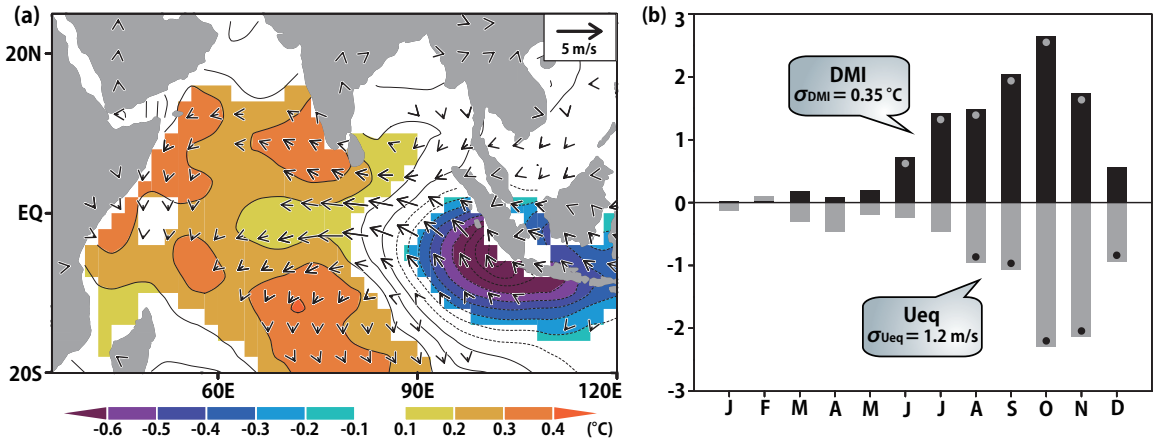

Fig. 1.2 (a) Composite of SST (in °C; contour and shade) and surface wind (in m/s; vectors) anomalies in September-October of the positive IOD year. Anomalies significant at 90% confidence level are shaded. Vectors are drawn when zonal or meridional component is significant at 90%. (b) Composite of the standardized Dipole Mode Index (DMI; black) and the equatorial zonal wind anomalies averaged over the central equatorial Indian Ocean (70-90°E, 5°S-5°N) (gray). Anomalies signigicant at 90% confidence level are marked with circles. The DMI is defined by the difference in SST anomalies between the tropical western Indian Ocean (50-70°E, 10°S-10°N) and the tropical southeastern Indian Ocean (90-110°E, 10°S-Equator). The ERSST version 3b and the NCEP/NCAR reanalysis (Kalnay et al., 1996) are adopted for the period of 1950-2011 for SST and surface winds, respectively. All the time series are detrended.

demonstrated that the IOD can exist even in the absence of ENSO using a coupled general circulation model (CGCM).

After the discovery of the IOD, many studies have shown that the tropical Indian Ocean plays an active role in the global climate system. It is found that the IOD not only influences the surrounding countries (Behera et al., 1999, 2005; Ashok et al., 2003; Zubair et al., 2003; Yuan et al., 2012), but also global climate through atmospheric teleconnections (Saji and Yamagata, 2003a; Yamagata et al., 2004; Behera et al., 2013). The IOD even influences ENSO through the change in the Walker circulation (Izumo et al., 2010). Moreover, the Indian Ocean basin mode, which was thought to be just a response to ENSO, turned out to feedback onto the western Pacific climate (Xie et al., 2009). In addition, Kosaka et al. (2013)

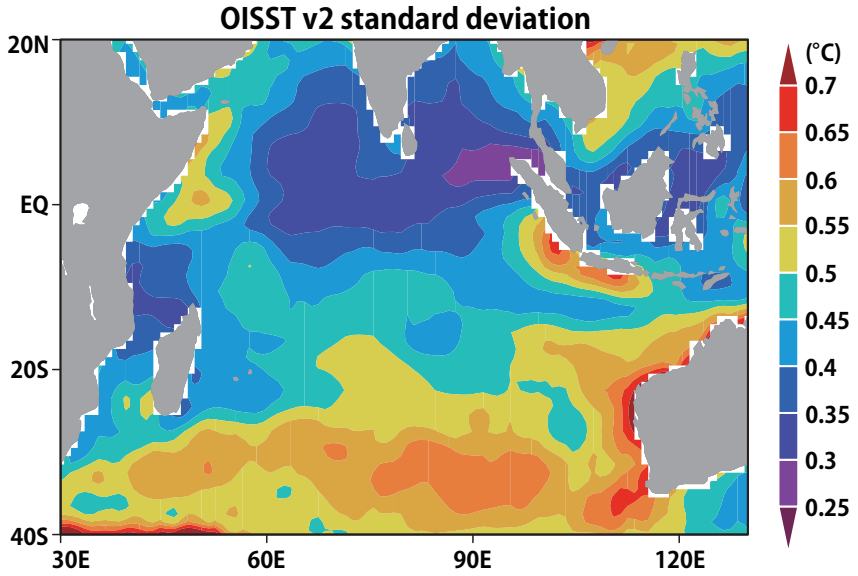

Fig. 1.3 Standard deviation of SST anomalies (in °C) in the Indian Ocean with a linear trend and monthly climatology removed. The OISST version 2 (Reynolds et al., 2002) is used for the period of 1982-2013

reported the coupling of the northern Indian Ocean with atmospheric variability in the Pacific called the Pacific-Japan pattern (Nitta, 1987).

1.2 Southeastern Indian Ocean and discovery of Ningaloo Niño

Although the tropical Indian Ocean climate variability have been studied extensively, the strongest interannual SST variation is seen along the western coast of Australia (Fig. 1.3). The region is quite unique compared with other eastern subtropical basins owing to the existence of the Indonesian Throughflow and the Leeuwin Current.

The Indonesian Throughflow flows from the western Pacific to the eastern Indian Ocean and is the only current that transports water from one basin to another in the lower latitudes (Lukas et al., 1996; Sprintall et al., 2014). The Pacific trade winds pile up water in the

western Pacific and set up pressure gradient between the Pacific and Indian Oceans. This pressure gradient drives the Indonesian Throughflow, which undergoes significant seasonal variation under the strong Asian-Australian monsoon system with the seasonal maximum in austral winter (Masumoto and Yamagata, 1996; Sprintall et al., 2009).

The Leeuwin Current is also very different from other eastern boundary currents in the subtropical basins flowing equatorward; it flows poleward along the western coast of Australia against the prevailing southerly alongshore winds (Cresswell and Golding, 1980; Thompson, 1984). Pressure gradient force associated with strong meridional surface density gradient owing to salinity gradient (Menezes et al., 2013) balances eastward geostrophic flow, part of which forms the Eastern Gyral Current and breaks the wind-driven circulation (e.g. Ekman, 1905; Sverdrup, 1947). Existence of the Australian continent blocks the eastward current, resulting in coastal downwelling. Also, the continental shelf (Weaver and Middleton, 1989; Furue et al., 2013) and vertical mixing (McCreary et al., 1986) trap (or prohibit the westward propagation of) the energy, allowing for the development of the poleward current. Kundu and McCreary (1986) suggested that the Indonesian Throughflow is also a source of the Leeuwin Current.

Because of the existence of these unique ocean currents and the absence of upwelling, SSTs in the eastern South Indian Ocean are higher by $\sim$5°C compared to other eastern boundary regions at the same latitudes (Fig. 1.4). The high SSTs provide a favorable condition for active air-sea interaction (e.g. Graham and Barnett, 1987).

Regarding the interannual variation in the southeastern Indian Ocean, a link with ENSO has been reported (e.g. Pariwano et al., 1986). To explain this relationship, Clarke (1991) investigated very low-frequency equatorial waves incident on "gappy" western boundary (i.e. Indonesian maritime continent) and showed that the equatorial long Rossby wave signals leak to the Australia's western coastline. Since his theory explains observed variability well, oceanic interannual variability off the western coast of Australia had long been considered

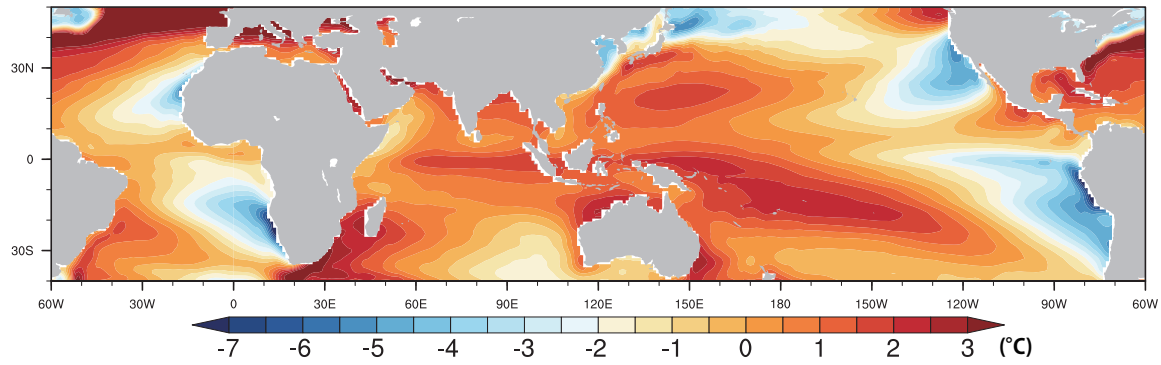

Fig. 1.4 Annual-mean SST deviation (in °C) from the zonal mean obtained from the OISST version 2. The data from 1982 to 2013 is used and a linear trend is removed.

to be explained mostly by ENSO until quite recently (e.g. Clarke and Liu, 1994; Wijffels and Meyers, 2003; Feng et al., 2003, 2008). In austral summer of 2010/11, the eastern South Indian Ocean experienced the highest SSTs on the instrumental records (Fig. 1.5). Because of its similarity with El Niño, it was named Ningaloo Niño (Feng et al., 2013). The thermal stress significantly changed the biodiversity pattern (Wernberg et al., 2012) and caused devastating coral bleaching there (Depczynski et al., 2013). Feng et al. (2013) examined the generation mechanism of this specific event and inferred that it was mainly driven by the anomalously strong Leeuwin Current in response to unusually strong trade winds in the tropical Pacific associated with strong La Niña. They also suggested that a Matsuno-Gill type response to La Niña-related diabatic heating anomalies in the western tropical Pacific generated anomalous negative SLPs off Western Australia and associated northerly-alongshore wind anomalies further strengthened the Leeuwin Current.

1.3 Purposes of this study

The research on Ningaloo Niño has just begun and many important issues remain to be investigated. Among others, Feng et al. (2013) reported that the phenomenon was mainly a response to La Niña by examining a single event in 2010/11, but not all Ningaloo Niño events

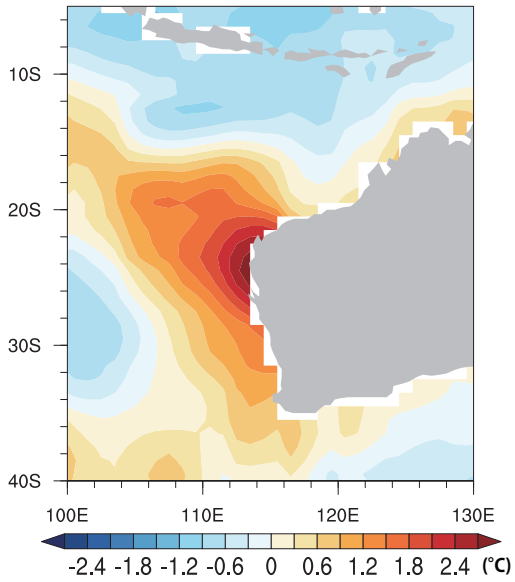

Fig. 1.5 SST anomalies (in °C) in January 2011 obtained from the OISST version 2. Here, anomalies are calculated as deviation from the monthly climatology of 1982-2013 with a linear trend removed.

in the historical records co-occurred with La Niña. Rather, there was a Ningaloo Niño event that co-occurred even with El Niño, suggesting that Ningaloo Niño is not merely a response to ENSO and an intrinsic ocean-atmosphere coupled feedback may exist. In addition, although Feng et al. (2013) suggested the importance of anomalous meridional advection in generating warm SST anomalies, no quantitative analyses were carried out and the precise mechanism is not well understood. Furthermore, potential impacts of Ningaloo Niño on climate have not been discussed so far.

This thesis is organized as follows. In the next chapter, using various observational and reanalysis data, we show the importance of the local air-sea interaction for the evolution of Ningaloo Niño. Ningaloo Niña, the opposite phase of Ningaloo Niño, is introduced and examined as well. To understand the generation mechanism of SST anomalies in detail, mixed-layer heat budget analysis is conducted in Chapter 3. Since spatiotemporal resolution of oceanic observational datasets are not enough, we use outputs from a realistic ocean

general circulation model simulation for this purpose. Then, the relative importance of local and remote SST anomalies in generating SLP anomalies off Western Australia during Ningaloo Niño/Niña is investigated using an atmospheric general circulation model (AGCM). We also examine the influence of Ningaloo Niño/Niña on precipitation over Western Australia by the same AGCM experiments. These results based on the AGCM are presented in Chapter 4. As mentioned above, the observational records suggest that Ningaloo Niño is not just a simple response to ENSO. However, the ENSO influence is not necessarily linear and it cannot be completely removed from observational data. Therefore, we use a CGCM to show that Ningaloo Niño with the similar amplitude can develop even without ENSO in Chapter 5. The final chapter summarizes the main results and discusses the implication of this study.

Chapter 2

On the Ningaloo Niño/Niña:

Observational analysis

This chapter has been published as:

Kataoka, T., T. Tozuka, S. Behera, and T. Yamagata, 2014: On the Ningaloo Niño/Niña. *Clim. Dyn.*, **43**, 1463-1482.

2.1 Introduction

Interannual monthly sea surface temperature (SST) anomalies in the Indian Ocean show the most striking variation along the western coast of Australia as seen in Fig. 2.1a. The origin of this variability is the main focus of this chapter.

This region is known for its unique character. The Leeuwin Current flows poleward against the winds along the western coast as shown in Fig 2.1b (Andrew, 1977; Cresswell and Golding, 1980; McCreary et al., 1986). This current attains its maximum strength of about 0.5 m/s in austral winter when the alongshore equatorward winds are weakest (Smith et al., 1991). The SST variations in this region influence marine lives like western rock lobster (Caputi et al., 1996). A recent strong warming in 2011 led to widespread coral bleaching (Depczynski et al., 2013; Pearce and Feng, 2013; Feng et al., 2013). The SST variations are also expected to induce precipitation anomalies over western Australia, and may influence the agriculture there. Therefore, understanding of the remarkable interannual SST variations, recently named Ningaloo Niño (see Feng et al., 2013) and Ningaloo Niña (the opposite phase of Ningaloo Niño), is important not only from a scientific viewpoint but also from a socioeconomic viewpoint.

On both seasonal and interannual timescales, Feng et al. (2008) showed that the upper ocean temperature off south Western Australia is mainly controlled by heat advection of the Leeuwin Current. They discussed its relation to El Niño/Southern Oscillation (ENSO). In this chapter, we revisit the origin of the strong interannual SST variability off the west coast of Australia and show the importance of local air-sea interaction and modulation of advection by the Leeuwin Current using various observational and reanalysis data.

This chapter is organized as follows. A brief description of the data is given in the next section. In section 2.3, we examine the formation mechanism of the regional climate mode

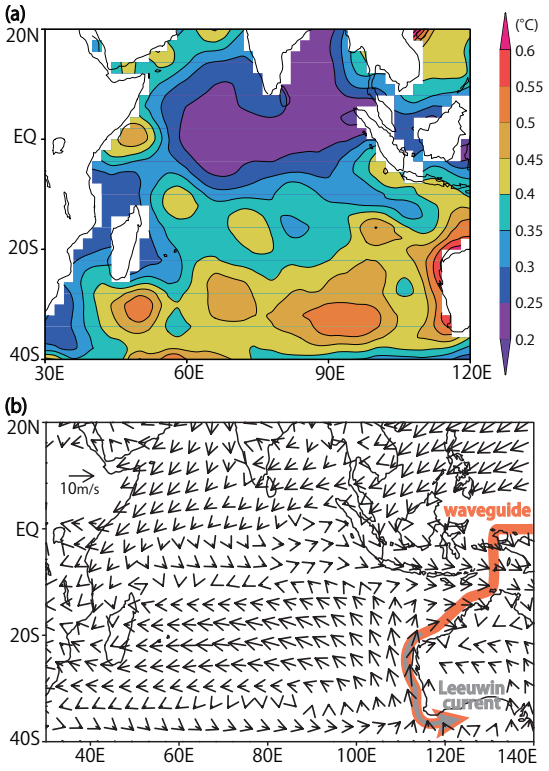

Fig. 2.1 (a) Standard deviation of monthly SST anomalies in the Indian Ocean during 1950-2011. The Extended Reconstructed Sea Surface Temperature (ERSST) version 3b is used. (b) Climatological surface wind averaged from December to February. Schematics of the positions of the Leeuwin current (gray arrow) and waveguide along which equatorial and coastal waves propagate (red arrow) are superposed.

of interest in detail. Their possible influence on the rainfall over Australia is also discussed. The final section provides summary and discussions.

2.2 Data

The Extended Reconstructed Sea Surface Temperature (ERSST) version 3b dataset (Smith et al., 2008) with 2° x 2° resolution from 1950 to 2011 is used. Our research extends back to the 1950s, when the quality of the data is somewhat questionable in some area. However, as shown in Fig. 2.2, relatively large number of data is available because of ship

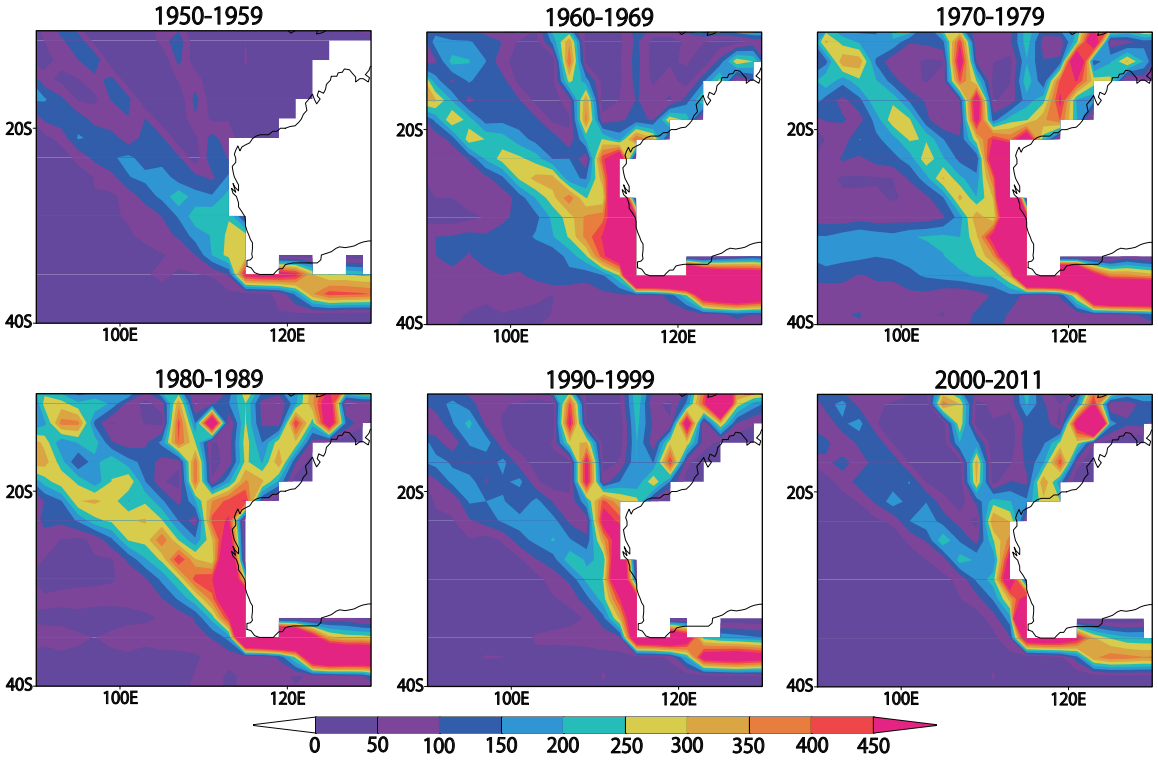

Fig. 2.2 Number of observations in austral summer during each decade (only the lower right panel includes 12 years).

tracks that go through the area and it is reliable enough to capture the variability off Western Australia. We also use the National Centers for Environmental Prediction/National Center for Atmospheric Research (NCEP/NCAR) reanalysis data (Kalnay et al., 1996) for sea level pressure (SLP) and wind at 850 hPa and 10 m for the same period, and datasets from the University of Delaware for precipitation (Legates and Willmott, 1990) from 1950 to 2010. The horizontal resolution is 2.5° x 2.5°, 2.5° x 2.5°, T62 Gaussian grid with 192 x 94 points, and 0.5° x 0.5°, respectively. The sea surface height (SSH), ocean current, and temperature derived from Simple Ocean Data Assimilation (SODA; Carton and Giese, 2008) version 2.2.4 are also adopted from 1950 to 2008. It is available at 0.5° horizontal resolution and has 40 vertical levels with 10 m resolution near the surface. The latent heat flux from the Objectively Analyzed air-sea Fluxes (OAFlux) project with 1° x 1° resolution from 1958 to 2011 is used

(Yu et al., 2008). Unless otherwise noted, linear trends are removed using a least-square fit. We note that almost the same results are obtained using the following datasets. Those are the National Oceanic and Atmospheric Administration (NOAA) Optimum Interpolated Sea Surface Temperature (OISST) V2 dataset (Reynolds et al., 2002) for SST with 1° x 1° resolution from 1982 to 2011, the European Centre for Medium-Range Weather Forecasts (ECMWF) 40-year Re-analysis (ERA-40; Uppala et al., 2005) for the surface wind and latent heat flux with a resolution of 2.5° x 2.5° during 1958-2001, the NCEP Global Ocean Data Assimilation System (GODAS; Behringer and Xue, 2004), which consists of the SSH on 0.333° x 1° for the period 1980-2011, the Climate Prediction Center Merged Analysis of Precipitation (CMAP; Xie and Arkin, 1997) for the rainfall with a horizontal resolution of 2.5° x 2.5° from 1982 to 2011.

2.3 Results

First, we adopt an empirical orthogonal function (EOF) analysis to extract the dominant mode of variability in the monthly SST anomaly over the region 100°E -120°E, 34°S -12°S. Figure 2.3a shows the pattern of the first EOF mode that explains 52% of the total variance. This gravest mode is validated according to the criterion by North et al. (1982) because of its significant separation from the second mode. This result is not sensitive to slight changes in the domain size; almost the same results are obtained even if the domain is extended by 4° to east, west, north, and south. As expected, the large variability is attached to the west coast of Australia, and this captures the pattern shown in Fig. 2.1. We refer to this phenomenon as “Ningaloo Niño” when the anomaly is positive (Feng et al., 2013) and “Ningaloo Niña” when the anomaly is negative.

Based on the EOF analysis, we define the Ningaloo Niño index (NNI) by taking an area-average of SST anomalies in the box (108°E-coast, 28-22°S) shown in Fig. 2.3a. The

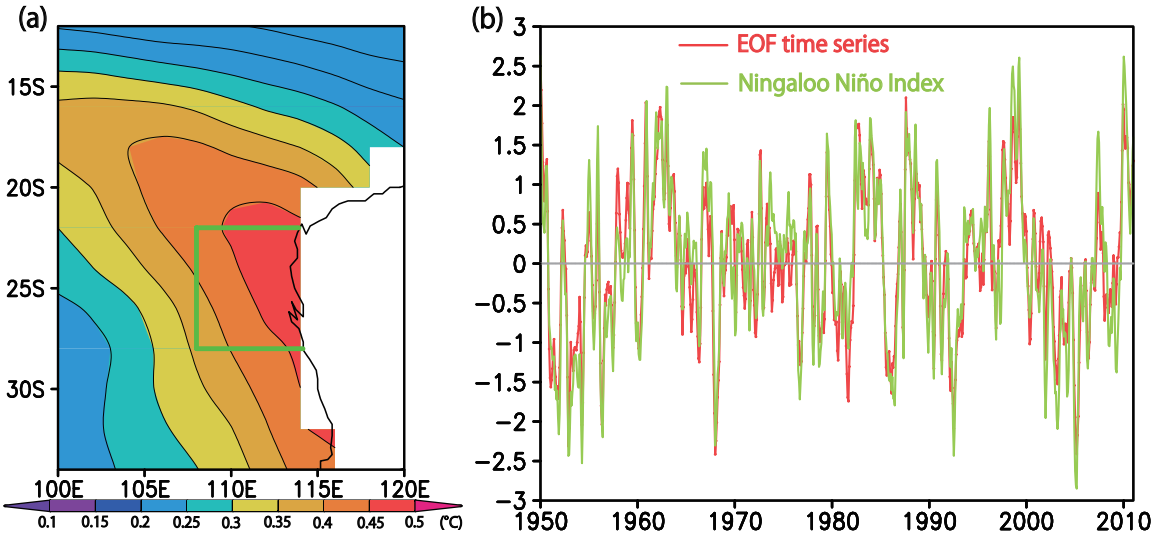

Fig. 2.3 (a) First EOF mode of SST anomaly off Western Australia. The green box indicates the domain used to calculate the NNI (108°E-coast, 28-22°S). (b) Time series of normalized principal component of EOF1 (red) and Ningaloo Niño Index (NNI; green). One sigma of the NNI corresponds to 0.44°C.

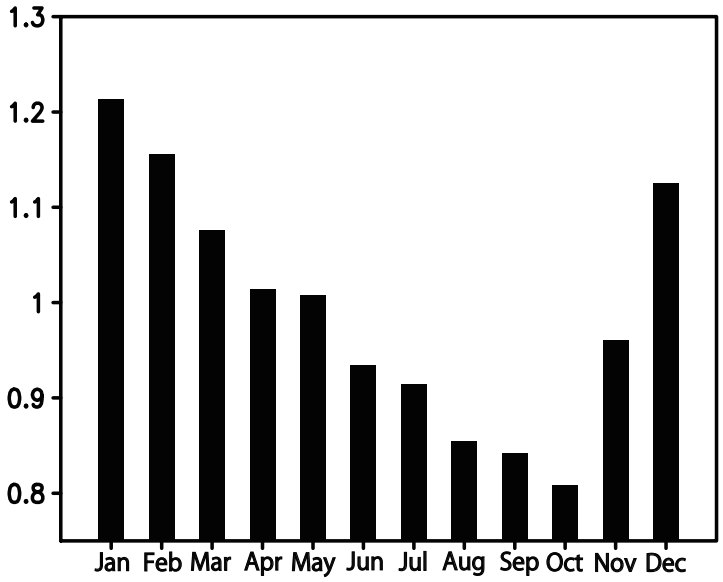

Fig. 2.4 Monthly standard deviation of the normalized NNI.

NNI corresponds well with the time series of the first EOF mode with a correlation coefficient of 0.87. To check whether Ningaloo Niño (Niña) is locked to the annual cycle, the standard deviation of the normalized NNI is given in Fig. 2.4 as a function of calendar month. We find that Ningaloo Niño (Niña) reaches its peak during austral summer from December to February (DJF). It is interesting to note that there is a clear asymmetry in its life cycle; Ningaloo Niño (Niña) grows rapidly from October, reaches its peak in January, and decays gradually. Because of its seasonal phase-locking nature, we define the Ningaloo Niño (Niña) year as the year when the DJF-averaged NNI is above (below) one (negative one) standard deviation. This criterion leads us to define 11 Ningaloo Niño years (1955/56, 60/61, 61/62, 62/63, 66/67, 73/74, 79/80, 82/83, 96/97, 99/00, and 10/11) and 11 Ningaloo Niña years (1951/52, 52/53, 53/54, 76/77, 86/87, 90/91, 91/92, 92/93, 03/04, 04/05, and 05/06). In the analysis hereafter, year 0 means the year when Ningaloo Niño (Niña) develops and year 1 denotes the following year.

To derive the main features of Ningaloo Niño (Niña), we construct composite diagrams of the SST anomaly field. Figure 2.5 shows that significant SST anomalies first appear in October (0) (September (0)), peak around December (0) to February (1), and begin to decay in March (1) with the center of anomalies shifting southward along the coast for Niño (Niña). The composites of surface wind anomalies are also prepared to examine possible regional ocean-atmosphere coupling. Statistically significant wind anomalies that favor coastal downwelling (upwelling) anomalies and thus positive (negative) SST anomalies for Ningaloo Niño (Niña) are rather sporadic off the coast of Western Australia (Fig. 2.6); significant northerly wind anomalies off the western coast of Australia are seen only in January (1) for the Niño composite. However, we need to remember that the composite analysis is effective only when a single mechanism dominates. The above sporadic nature of the relation between wind and SST anomalies may suggest that more than one mechanism may operate; alternative mechanisms that can affect SST are advection by the Leeuwin

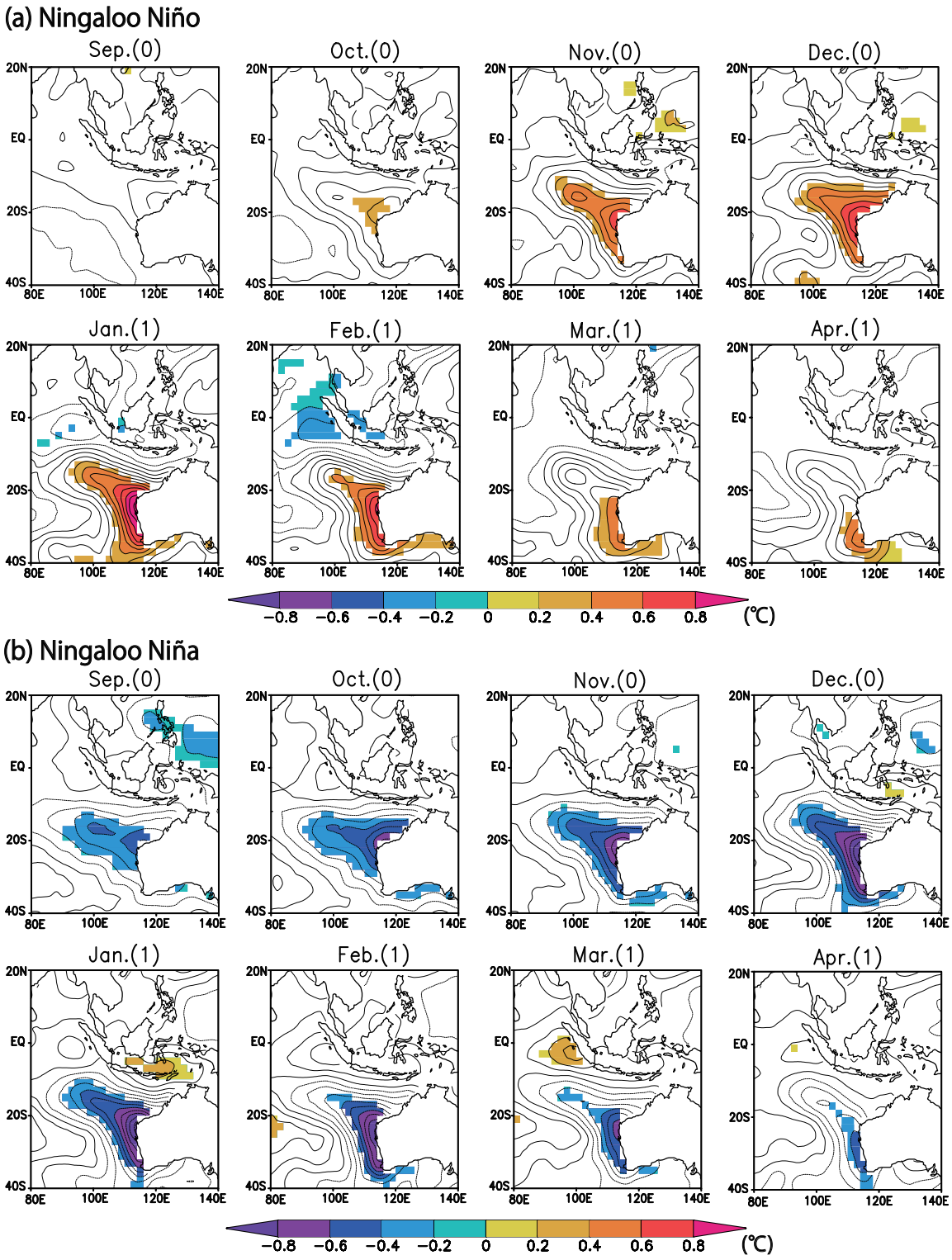

Fig. 2.5 (a) Composites of the SST anomaly (in °C) in the Ningaloo Niño year. The contour interval is 0.1°C. Anomalies exceeding 95% confidence level by a two-tailed t-test are shaded. (b) As in (a), but in the Ningaloo Niña year.

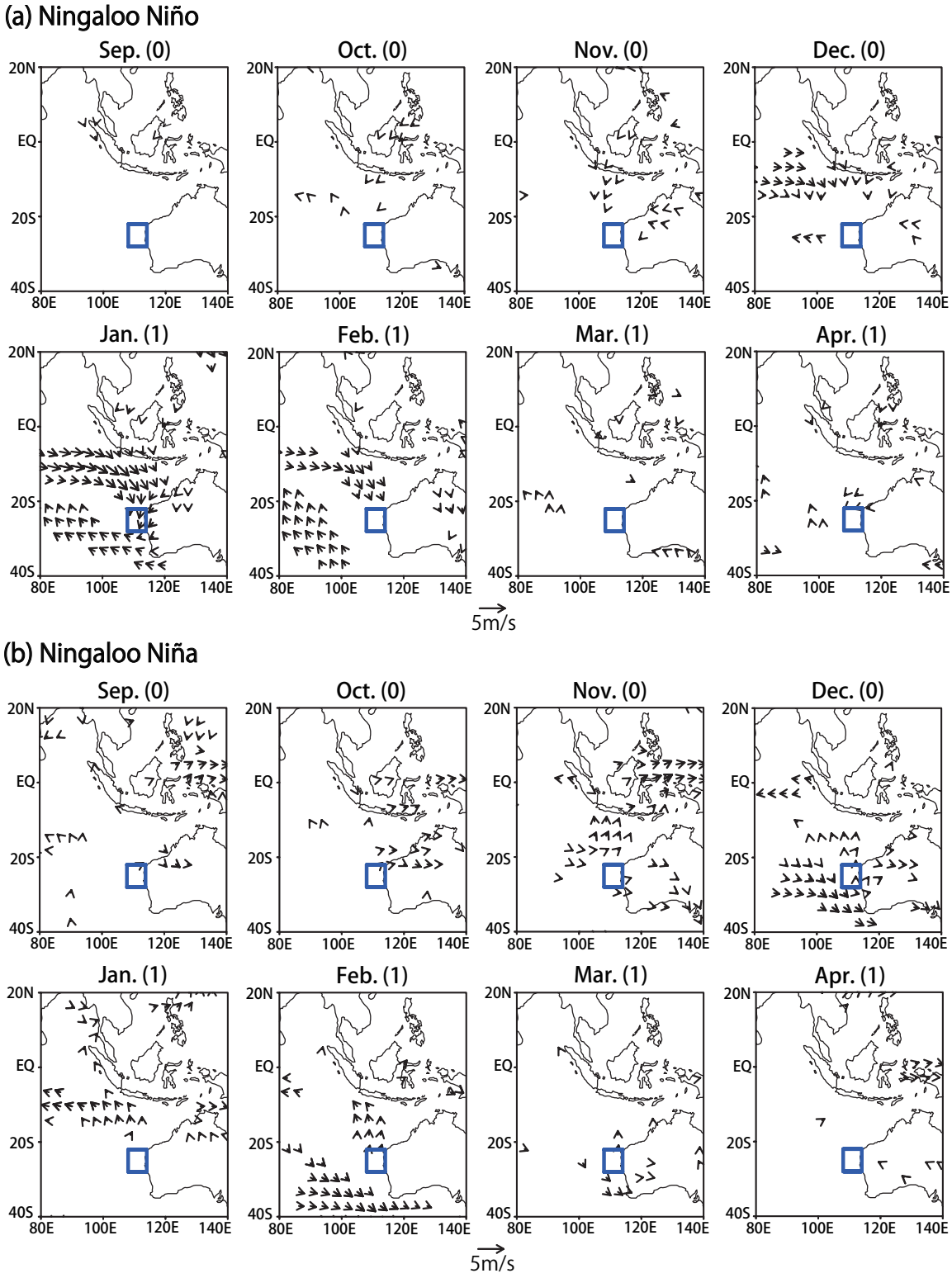

Fig. 2.6 As in Fig. 2.5, but for the surface wind anomaly (in m/s). Anomalies above 95% confidence level by a two-tailed t-test are drawn. The domain used to define the coastal wind index (CWI) is superposed (blue box).

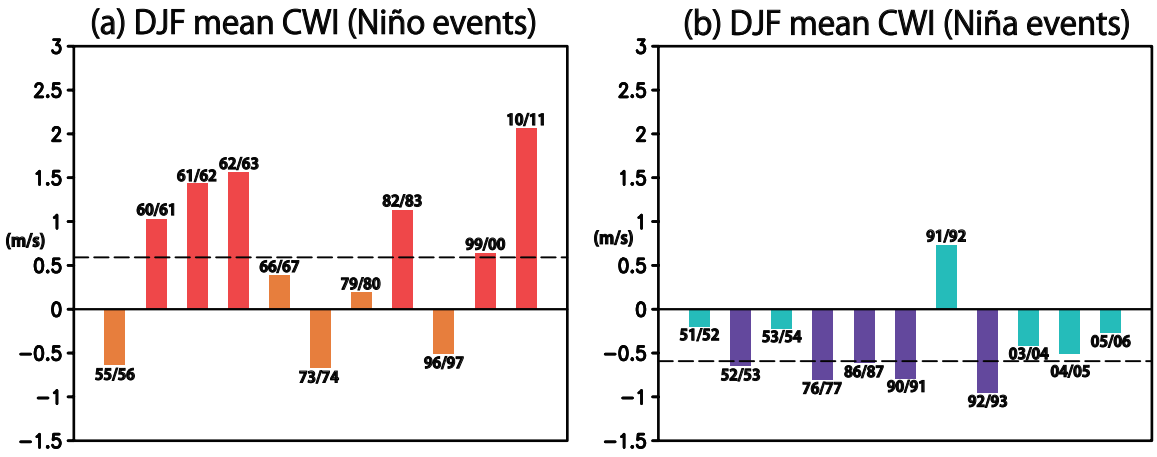

Fig. 2.7 (a) DJF mean CWI in each Ningaloo Niño year. The dashed line indicates 0.9 sigma of the CWI. The "locally amplified" cases are expressed in red, whereas the "non-locally amplified" cases are in orange. (b) As in (a), but for each Ningaloo Niña year. The dashed line represents -0.9 sigma of the CWI. The "locally amplified" cases are drawn in purple, whereas the "non-locally amplified" cases are in light blue.

Current and local air-sea heat fluxes. Therefore, we need to look at each event more precisely.

For this purpose, we introduce the coastal wind index (CWI) by averaging the meridional component of surface wind anomalies over the region 108-114°E, 28-22°S (Fig. 2.6). This CWI is defined to have a positive sign when wind anomalies are northerly and favor coastal downwelling anomalies. As expected, the CWI averaged over the austral summer from December to February (DJF) varies from event to event as illustrated in Fig. 2.7; the Niño events are much more diverse than the Niña events. In some events, the CWI even shows an opposite sign. Therefore, we separate the events into two cases. For Ningaloo Niño (Niña) events with the CWI exceeding 0.9 (falling below -0.9) standard deviations are named the "locally amplified case", whereas the others are named the "non-locally amplified case". The reason for this classification will become clear later.

2.3.1 Ningaloo Niño

Figure 2.8a shows the composite of SST and surface wind anomalies in January (1) for the locally amplified case. We see SST anomalies associated with alongshore-northerly wind anomalies off the western coast of Australia. In fact, as seen Fig. 2.8b, the CWI evolves remarkably together with the NNI with its peak during January (1) to February (1), suggesting the close ocean-atmosphere coupling as seen for the Indian Ocean Dipole Mode in the equatorial Indian Ocean (Fig. 1.2b; Saji et al., 1999; Webster et al., 1999). The NNI reaches its maximum in February (1). We note here that the events appear first in the SST anomaly in September (0), when coastal wind anomalies are not seen. In contrast, for the non-locally amplified case, surface wind anomalies favoring coastal downwelling are not clear (Fig. 2.8c). As expected, the CWI composite shows no significant anomalies and even has a negative sign during the mature season (Figs. 2.8d).

In the locally amplified case, positive SST anomalies are first generated to the west of Australia and produce low SLP anomalies in the overlying atmosphere. Figure 2.9a gives a composite picture of the DJF-averaged geopotential height anomalies for this case. The vertical structure shows a clear baroclinic structure, indicating that it is the local heating that generates negative SLP anomalies off Western Australia. The anomalous low is associated with anomalous northerly winds (Fig. 2.10a), exciting anomalous coastal downwelling (Fig. 2.11a). The anomalous downwelling leads to further amplification of initial warm SST anomalies by the intensification of the Leeuwin Current. This situation is more or less similar to the Bjerknes feedback for El Niño evolution in the equatorial Pacific. Although only vertical processes such as entrainment (i.e. themocline feedback; see Chapter 1) are taken into account in the original paper of Bjerknes (1969), later studies pointed out the importance of anomalous oceanic currents in SST anomaly development (zonal advective feedback; e.g. Gill, 1983; Picaut and Delcroix, 1995). Here, we use the term Bjerknes feedback as an

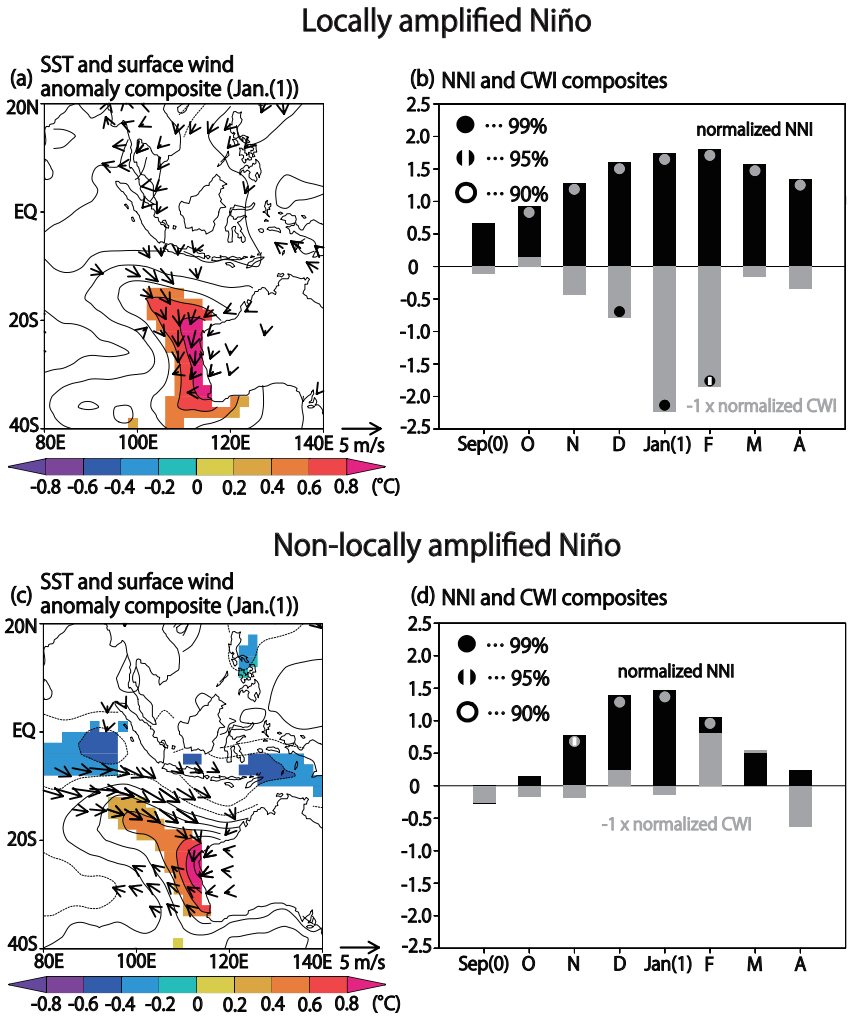

Fig. 2.8 Composite of (a) the SST (in °C) and surface wind anomalies (in m/s) for Jan. (1), (b) the normalized NNI and CWI in the locally amplified Niño year. In (a), SST and wind anomalies over 95% confidence level by two-tailed t-test are shaded and displayed. Open circles, open ovals, and closed circles show anomalies exceeding 90%, 95%, and 99% confidence level, respectively, by a two-tailed t-test in (b). (c), (d) As in (a) and (b) but for the non-locally amplified Niño year.

unstable air-sea coupling either through themocline or zonal advective feedback. Therefore, we may reasonably call this unstable ocean-atmosphere interaction the “coastal Bjerknes feedback”, and this is why we have given this phenomenon the name coastal Niño. Further consideration to the comparison with equatorial processes is given in the final chapter. It is

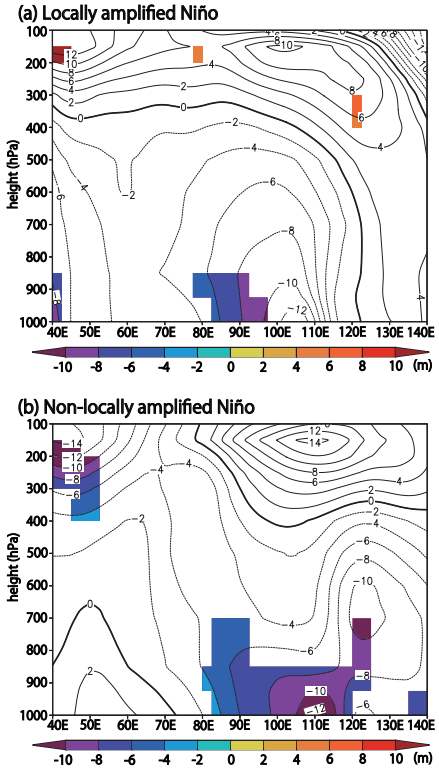

Fig. 2.9 Composites of the DJF mean geopotential height anomaly averaged between 28 and 22°S (in m) in the (a) locally amplified Niño year and (b) non-locally amplified Niño year. The contour interval is 2 m with the zero contour in bold. Anomalies exceeding 80% confidence level by two-tailed t-test are shaded. Note that the western edge of Australian continent at these latitudes is at about 114°E.

worthwhile to note that the DJF mean correlation between the area-averaged anomalies of the atmospheric winds and oceanic mixed-layer flows in the horizontal domain as used to derive the CWI is positive in every locally amplified case except for 99/00 event (figure not shown). Thus, the events satisfy the necessary condition for the Bjerknes instability as derived theoretically by Yamagata (1985) and verified by Goddard and Philander (2000) for El Niño (see Appendix). Here, the mixed-layer flow means the flow averaged within the mixed-layer depth defined as the depth at which the temperature decreases by 0.8°C from the SST (Kara et al., 2000). Thus far we have shown that it is plausible that "coastal Bjerknes feedback" is active in the locally amplified Ningaloo Niño. Further analysis including calculation of

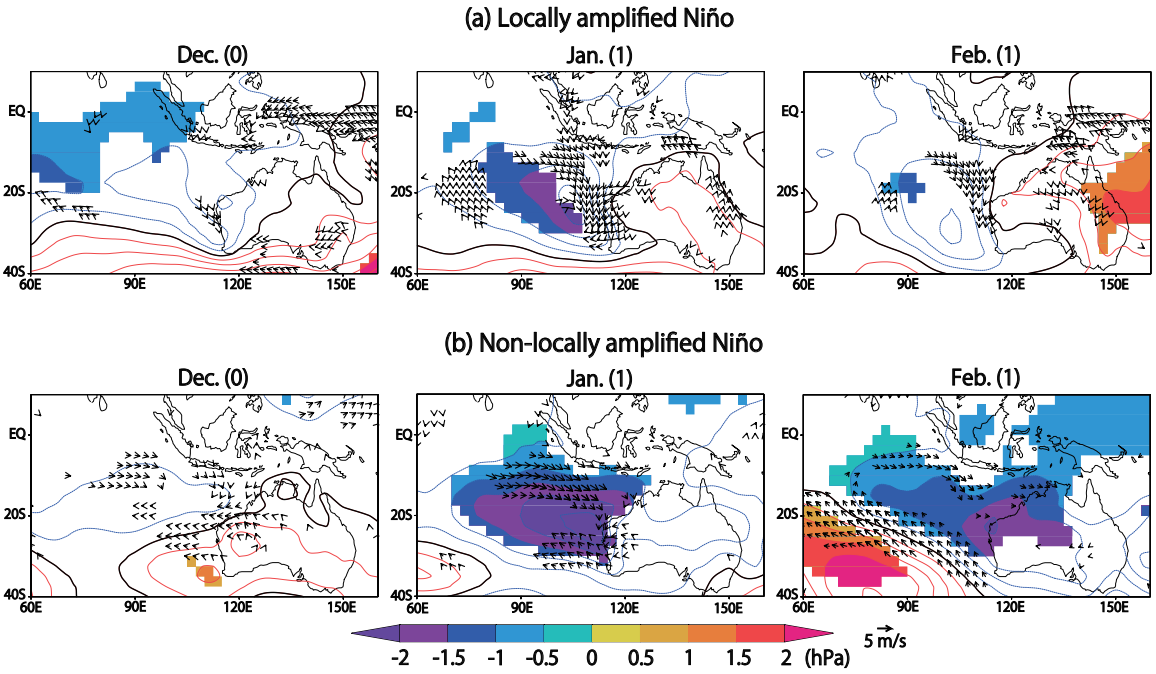

Fig. 2.10 Composites of the SLP (in hPa) and surface wind (in m/s) anomalies for austral summer in the (a) locally amplified Niño year and (b) non-locally amplified Niño year. The contour interval is 0.5 hPa and positive (Negative) contours are drawn in red (blue). Anomalies of the SLP (surface wind) exceeding 85% (95%) confidence level by a two-tailed t-test are shaded (drawn).

mixed-layer heat balance is necessary to quantify the mechanism and this will be conducted in Chapter 3.

For the non-locally amplified case, there are no significant wind anomalies that may cause anomalous coastal downwelling. However, the positive anomaly in the NNI is amplified and peaks during December (0)-January (1). As seen in Fig. 2.11b, positive SSH anomalies in the tropics propagate along the Australian coast as coastal waves. These signals are originated in the western tropical Pacific (Clarke, 1991; Clarke and Liu, 1994; Meyers, 1996) or the northern coast of Australia. The former origin is found to be mostly associated with La Niña (figure not shown). This important mechanism on the intrusion of the tropical Pacific signal into the western coast of Australia by coastal waves is called the Clarke-Meyers effect (Yamagata et al., 2004). Those downwelling coastal waves induce the

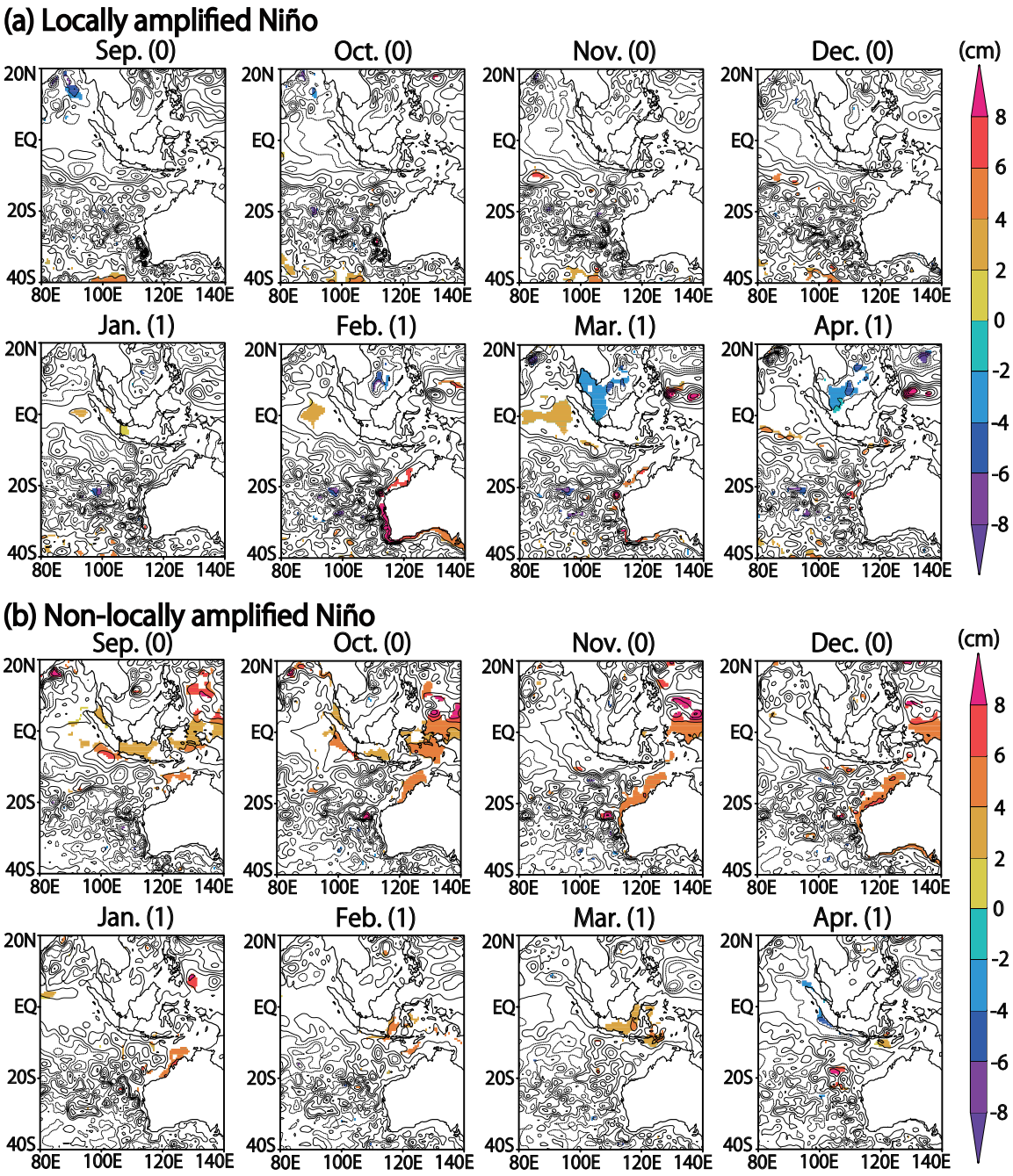

Fig. 2.11 (a), (b) As in Fig. 2.5, but for the SSH anomalies (in cm). The contour interval is 2 cm. Anomalies significant at 95% confidence level are shaded.

higher ocean temperature along the western coast of Australia by intensifying the Leeuwin Current (Feng et al., 2003; Clarke and Li, 2004). We note that the Clarke-Meyers effect may also trigger locally amplified events even though SSH anomalies are not statistically significant (Fig. 2.11a). Surface heat flux anomalies may generate initial SST anomalies as well (e.g. Marshall and Hendon, 2014).

Latent heat flux anomalies generally damp SST anomalies in the coastal region. However, they contribute to the growth of SST anomalies further offshore. Since the anomalous wind is from the lower latitude (Fig. 2.8) against the climatological wind (Fig. 2.1b), the wind speed is reduced. Furthermore, the moist air coming from the tropics decreases the difference in the surface specific humidity and suppresses the latent heat loss. We note that the latent heat anomalies may also contribute the growth of SST anomalies in the coastal region at the peak phase. The spatial pattern of latent heat flux anomalies in the non-locally amplified events resembles that of the locally amplified case (figure not shown).

The atmospheric conditions over the Australian continent for the two cases show a marked difference; the continental SLP anomalies are positive in the locally amplified case, whereas those are negative in the non-locally amplified case (Fig. 2.10). Consequently, the anomalous low in the locally amplified case forms a cell-like pattern and is accompanied by a sharp SLP gradient along the western coast. On the other hand, the anomalous low in the non-locally amplified case forms a zonally elongated band-like pattern extending into the eastern Indian Ocean. As a result, the zonal component dominates in the surface wind anomalies. Conversely, the patterns of SST anomalies associated with Ningaloo Niño in both cases are very similar as seen in Figs. 2.8a and c. We cannot find any significant difference in the composites of SLP anomaly above the ocean during austral summer, too; the SST anomalies in both cases induce negative SLP anomalies in the overlying atmosphere as indicated by their baroclinic structure shown in Fig. 2.9.

The marked difference in the anomalous atmospheric pressure over the Australian

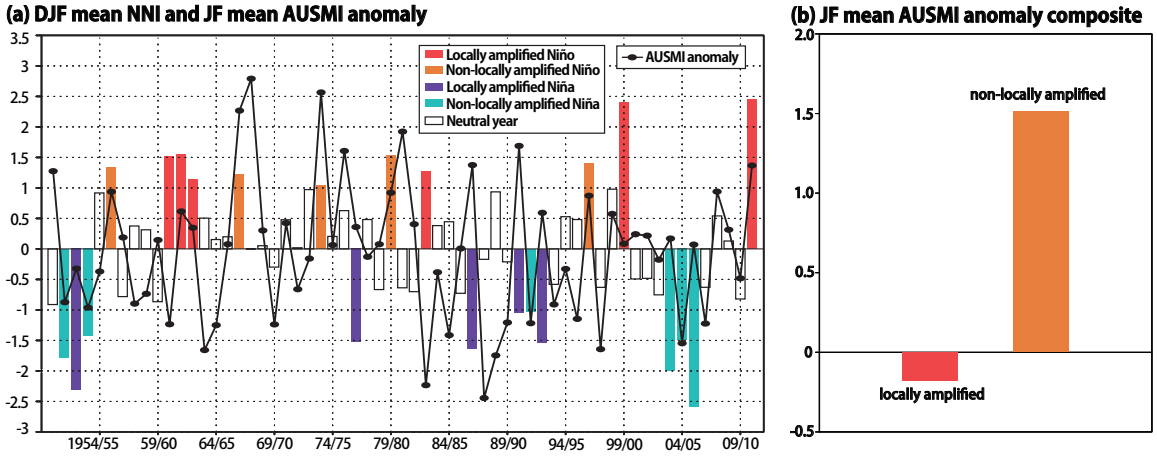

Fig. 2.12 (a) Time series of the normalized NNI averaged from December to February (bars) and the normalized JF mean AUSMI (black line with circles). The locally amplified Niño, non-locally amplified Niño, locally amplified Niña, and non-locally amplified Niña events are expressed as red, orange, purple, and light blue bars, respectively. (b) Composites of the normalized JF mean AUSMI anomaly in both types of Ningaloo Niño year. The difference between the two cases is significant at 95 % confidence level.

continent in the two cases is quite interesting. To clarify possible causes, we have calculated the Australian summer monsoon index (AUSMI; Kajikawa et al., 2009) (Fig. 2.12a) because it is related to Australian continental SLP (Kullgren and Kim, 2006). The AUSMI is defined as the area-averaged westerly wind over the region 15-5°S, 110-130°E at 850 hPa. Since the Australian summer monsoon starts in the latter half of December in the climatological mean (Hendon and Liebmann, 1990; Drosdowsky, 1996; Kajikawa et al., 2009), we exclude December (0) when taking the average (i.e. we only use January (1) and February (1)). As shown in Fig. 2.12b, the Australian summer monsoon is weaker in the locally amplified case. This means that SLP anomalies over the continent are positive (Fig. 2.10a). In contrast, in the non-locally amplified case, the continental SLP anomalies are negative (Fig. 2.10b) with anomalously strong Australian summer monsoon (Fig. 2.12b). Although the confidence level of the continental SLP anomalies is somewhat low (Fig. 2.10), we note that the difference between the two cases in the JF-mean continental SLP anomaly is significant (figure not

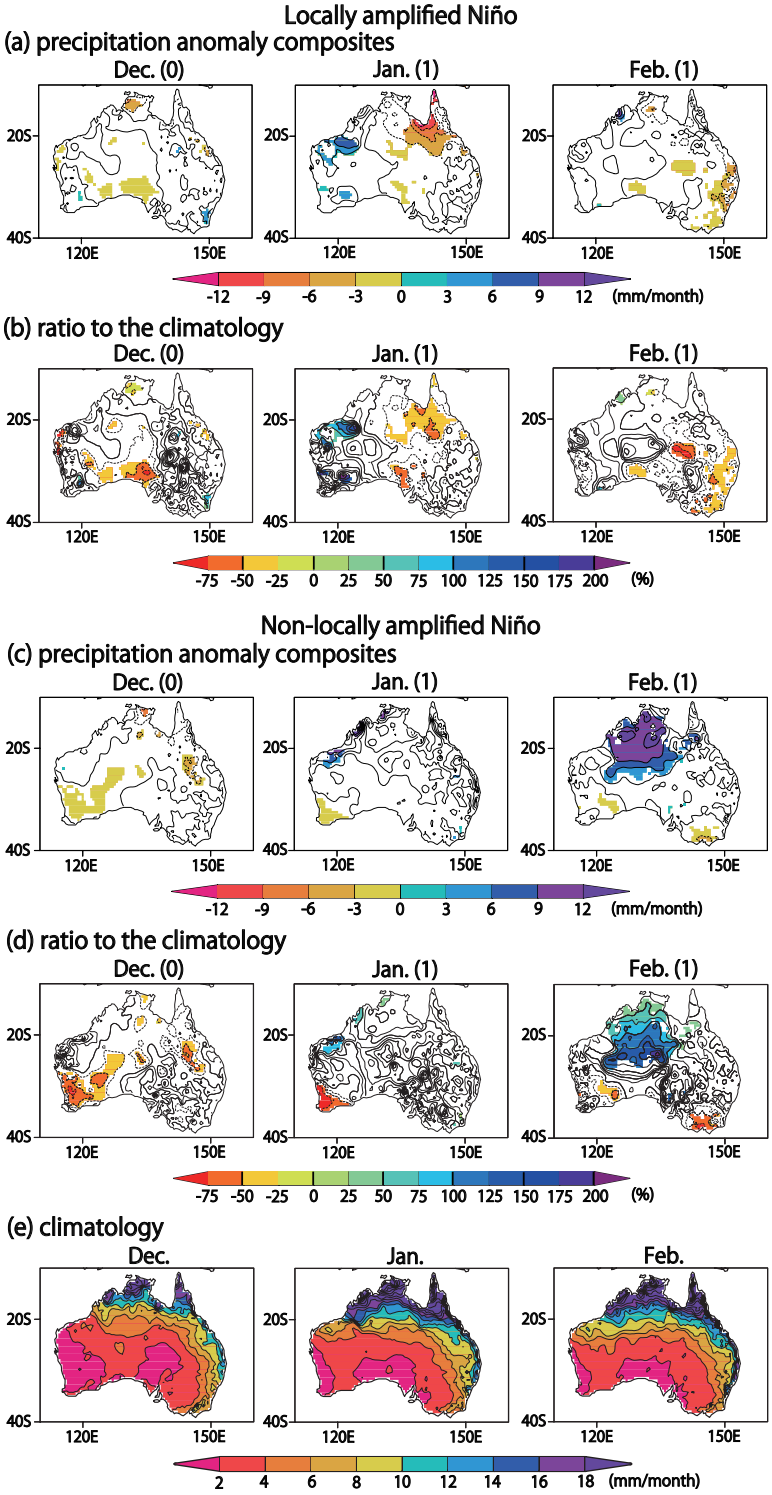

Fig. 2.13 As in Fig. 2.5a, but for (a) the monthly rainfall anomalies (in mm/month) and (b) its ratio to the climatology (in %). The contour interval is 3 mm/month and 25 %, respectively. Anomalies above 80% confidence level by a two-tailed t-test are shaded. Note that non-detrended climatology is used in (b), because the removal of the trend could lead to negative value in precipitation climatology. (c), (d) As in (a) and (b), but for the non-locally amplified Niño year. In (c) and (d), contours multiple of 50 are drawn in a thick line. (e) Non-detrended climatological rainfall (in mm/month).

shown).

To examine possible influences of Ningaloo Niño on the Australian rainfall, we have prepared composites of monthly precipitation anomalies during austral summer and their ratios to the climatology over Australia for both cases (Fig. 2.13). Positive rainfall anomalies along the western coast of Australia are seen for the locally amplified case. However, the signal is weak and the northern part even tends to be drier because of the weaker monsoon. For the non-locally amplified case, the warmer SST brings more rainfall in general with the additional support of the stronger than normal summer monsoon. However, in the southwestern part near Perth, where the agricultural activities are high, a severe drought occurs due to drier easterly wind anomalies (Fig. 2.10b). The rainfall anomalies are quite large compared to the climatology (Figs. 2.13d and e); the rainfall over the southwestern region reduces by more than 75% and that in the central part increases by 200% or more. The influence of the Ningaloo Niño on the rainfall over western Australia will be discussed in more detail in Chapter 4 using an atmospheric general circulation model (AGCM).

2.3.2 Ningaloo Niña

Composites of SST and surface wind anomalies in February (1) are presented in Fig. 2.14a. In the locally amplified case, southerly wind anomalies are seen over negative SST anomalies off the western coast of Australia. The composite of the CWI grows with the NNI (Figs. 2.14b) and peaks in February (1), suggesting the "coastal Bjerknes feedback" mechanism. In fact, amplification is seen around the center of Ningaloo Niña (Fig. 2.15a). On the other hand, no significant wind anomalies are seen in the non-locally amplified case (Figs. 2.14c and d). Instead, negative SSH anomalies propagating from the tropics seem to drive the non-locally amplified Ningaloo Niña by the Clarke-Meyers effect (Fig. 2.15b). The upwelling coastal waves may weaken the Leeuwin Current, thus amplifying negative SST anomalies.

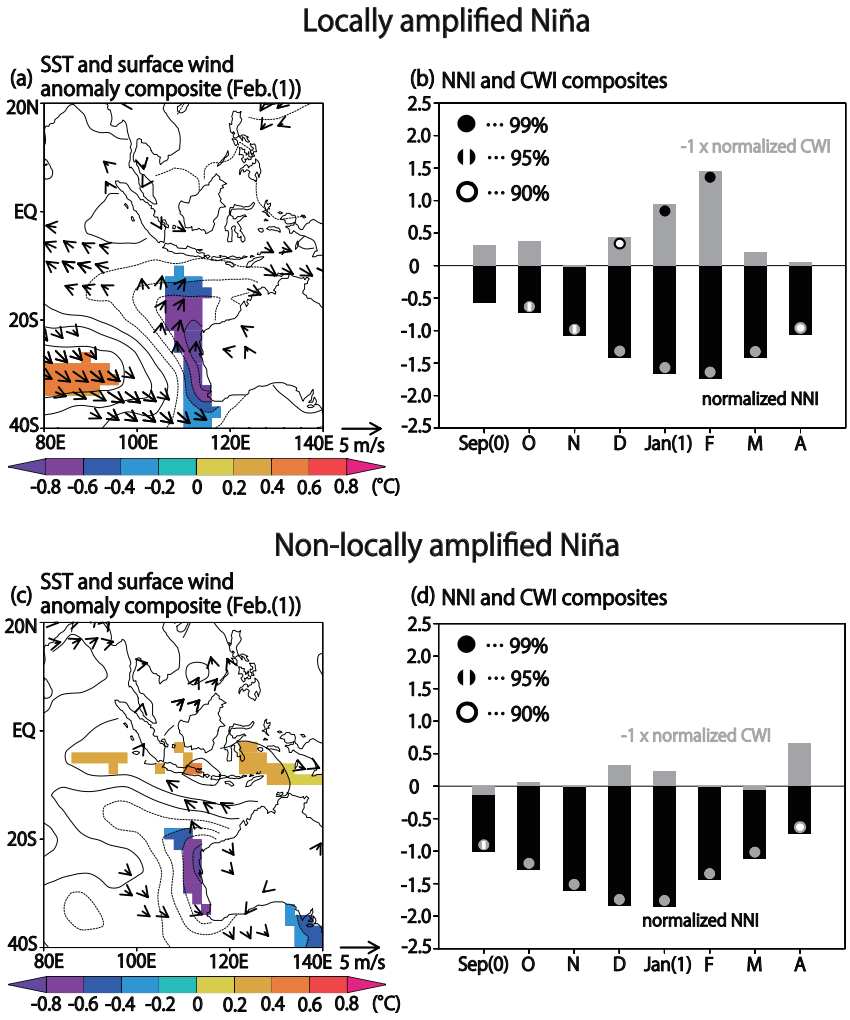

Fig. 2.14 As in Fig. 2.8, but for Ningaloo Niña.

A composite of geopotential height anomalies shows significant positive anomalies confined to the surface, indicating that negative SST anomalies generate an anomalous anticyclone (Fig. 2.16a). This is associated with the alongshore-southerly wind anomalies, which favor coastal upwelling (Fig. 2.17a), and thus amplify the negative SST anomalies. As in the Ningaloo Niño, latent heat flux anomalies generally damp SST anomalies along the coast, while it contributes to the SST anomaly growth further offshore (figure not shown). Also, the velocity fields satisfy the necessary condition for instability near the center of SST anomalies (Yamagata, 1985); the area-averaged atmospheric wind anomalies show a positive

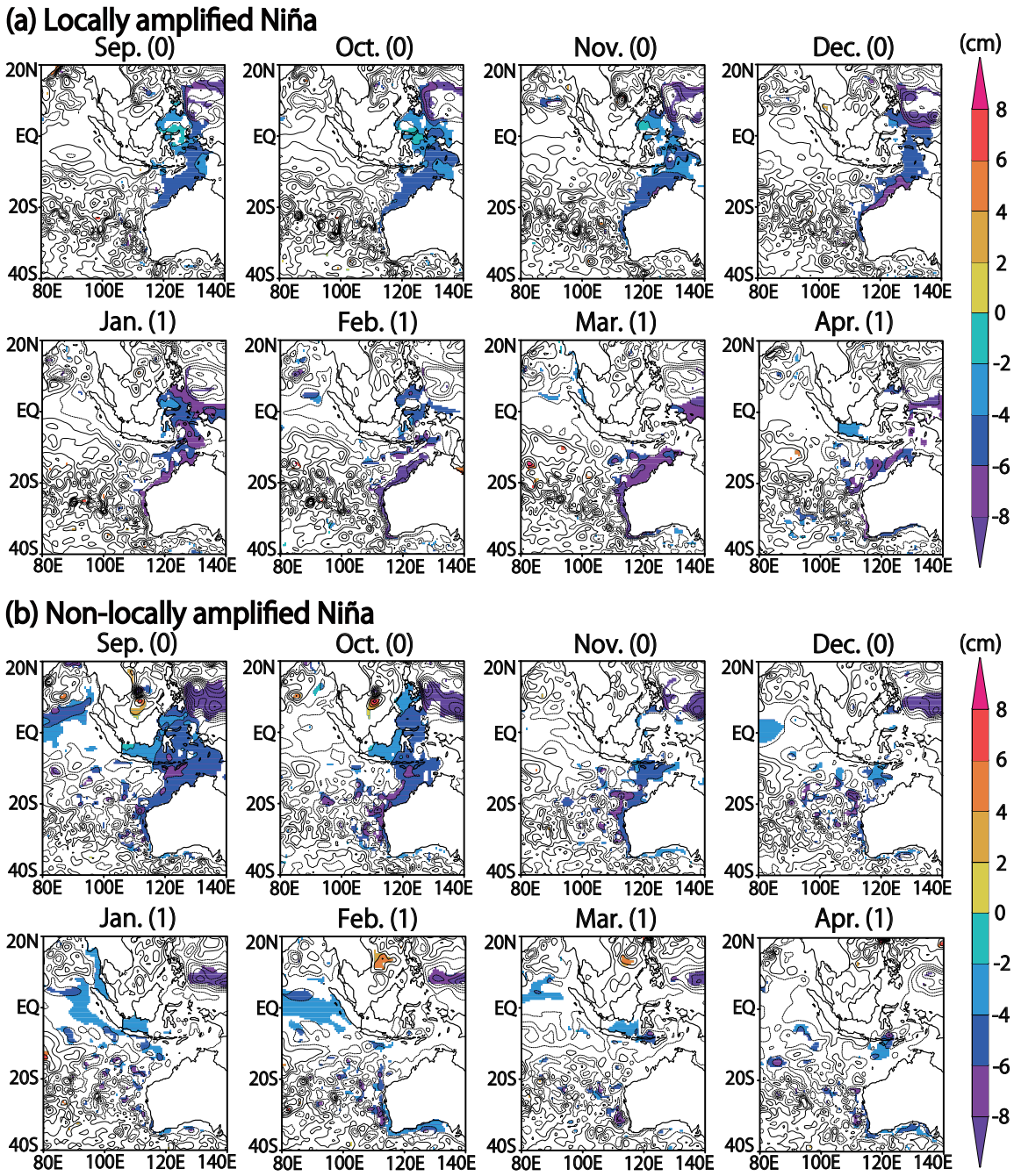

Fig. 2.15 As in Fig. 2.11, but for Ningaloo Niña.

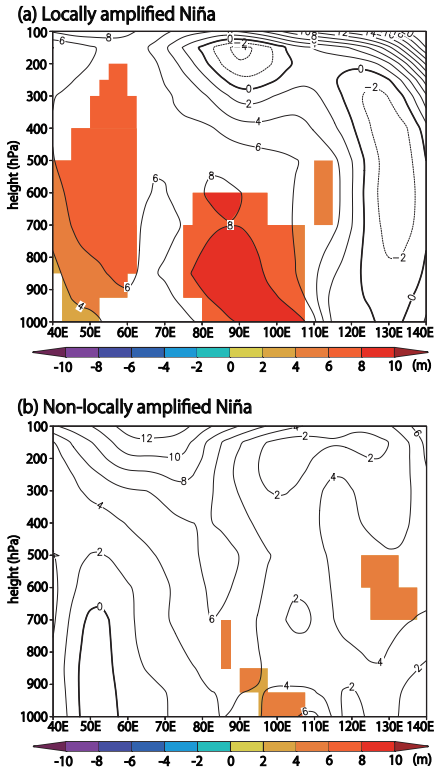

Fig. 2.16 As in Fig. 2.9, but for Ningaloo Niña.

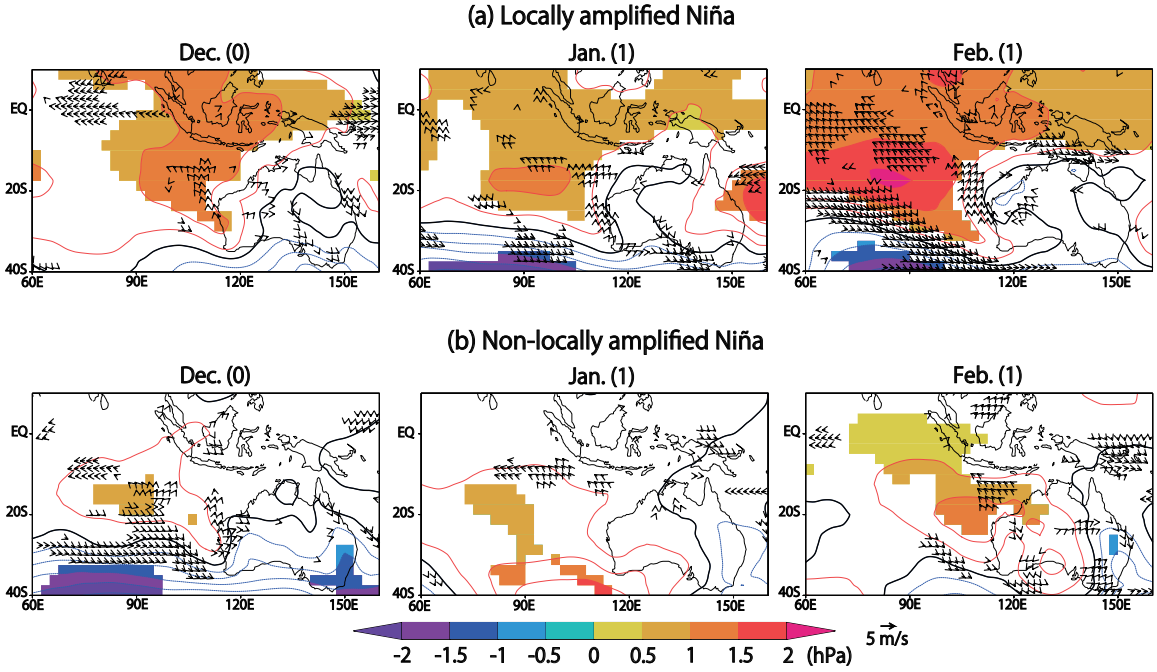

Fig. 2.17 As in Fig. 2.10, but for Ningaloo Niña.

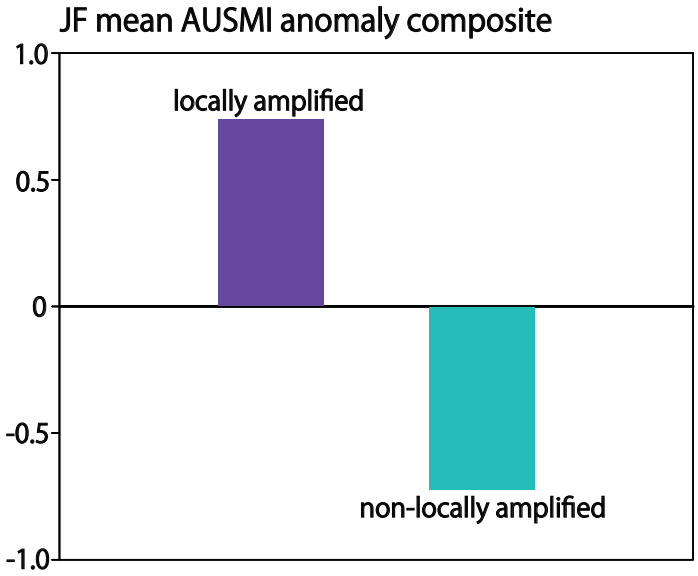

Fig. 2.18 As in Fig. 2.12b, but for Ningaloo Niña.

correlation in an austral summer mean with the anomalous flows in the oceanic mixed-layer in all locally amplified events except for 92/93 Ningaloo Niña (figure not shown). Although composites of geopotential height anomalies suggest the influence of SST anomalies on the overlying atmosphere in both cases, existence of other external forcing cannot be excluded for the generation of the anomalous high to the west of Australia (Fig. 2.16).

The difference between the locally and non-locally amplified cases is associated with the difference in the SLP gradient off Western Australia (Fig. 2.17). As in the previous subsection for Ningaloo Niño events, we examine roles of the Australian summer monsoon. Figure 2.18 reveals that negative SLP anomalies over the continent during the locally amplified case are related to the stronger Australian summer monsoon. On the other hand, the weaker Australian summer monsoon is related to the positive continental SLP anomalies in the non-locally amplified case. We note that the difference in the JF-mean SLP anomalies over the Australian continent is important, even though the confidence level is somewhat lower than that for the case of the Ningaloo Niño (figure not shown).

Figure 2.19 shows the posiible impact of Ningaloo Niña on the Australian summer

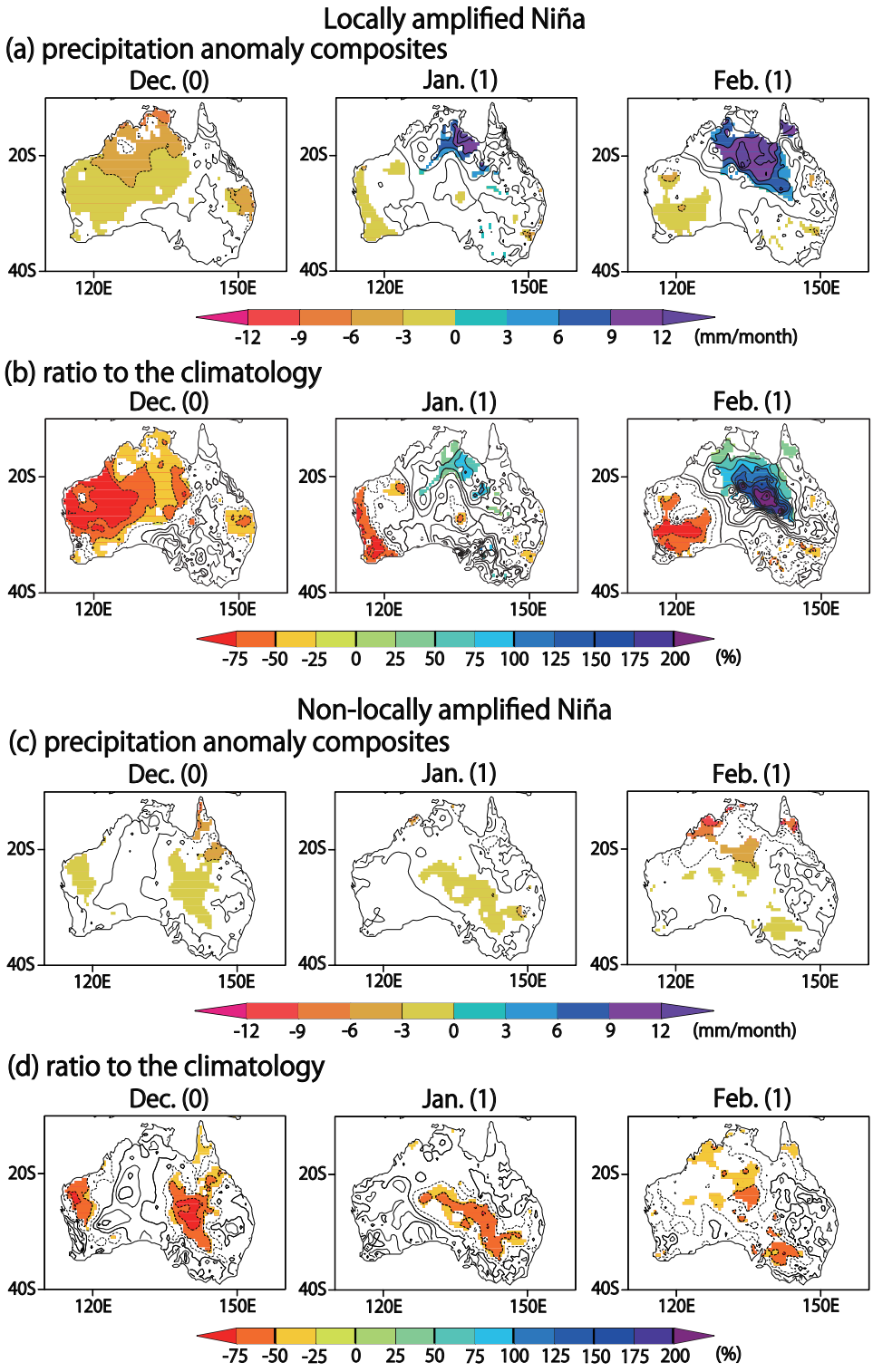

Fig. 2.19 As in Fig. 2.13(a)-(d), but for Ningaloo Niña.

rainfall. The locally amplified Ningaloo Niña brings a drought possibly through less evaporation associated with the cooler SST off the western coast. The precipitation over most of Western Australia is reduced by more than half of the climatology during this season. However, the northern part experiences more rainfall than normal because of the stronger Australian monsoon in January (1) and February (1). There is even a region where the rainfall is three times of the climatology. On the other hand, for the non-locally amplified case, the northwestern part tends to become drier because of the cooler SST and the weaker Australian monsoon. It is interesting to note that some part of the southwestern region tends to have more rainfall because the anomalous surface wind blows landward from the Indian Ocean, although the anomalies are not significant. The drier condition over western Australia as a response to Ningaloo Niña will be confirmed by AGCM experiments in Chapter 4.

2.4 Conclusions and discussions

Using observational and reanalysis data, we have examined the mechanism of newly identified phenomenon named Ningaloo Niño (Feng et al., 2013) as a typical coastal Niño like Benguela Niño (Shannon et al., 1986) along the western coast of southern Africa. In addition, as a mirror image of Ningaloo Niño, we have also defined Ningaloo Niña for completeness. In particular, we have put forward a plausible generation mechanism along with its relationship to precipitation over Western Australia. Ningaloo Niño (Niña) is associated with warm (cold) SST anomalies off the western coast of Australia and reaches the mature phase during austral summer. We have also classified Ningaloo Niño/Niña into two cases, namely the locally amplified and non-locally amplified cases, and pointed out the importance of variability in the Australian monsoon in generating these two cases.

For the locally amplified case (Figs. 2.20a, c), an anomalous low (high) is excited aloft when positive (negative) SST anomalies are generated to the west of Australia. The northerly

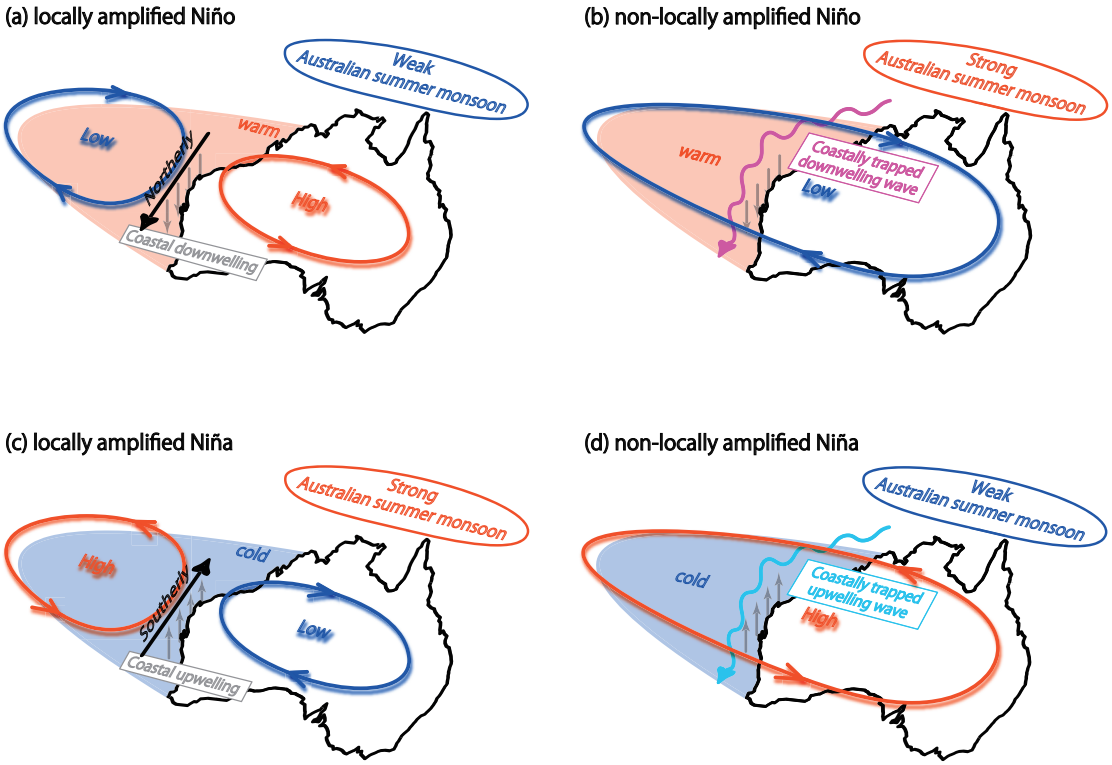

Fig. 2.20 Schematic diagrams of (a) the locally amplified and (b) non-locally amplified Ningaloo Niño. (c), (d) As in (a) and (b), but for Ningaloo Niña.

(southerly) wind anomalies associated with the anomalous low (high) induce anomalous coastal downwelling (upwelling) along the western coast of Australia, and enhance the warm (cold) SST anomalies. Except for 1992/93 Ningaloo Niña and 1999/2000 Ningaloo Niño, the atmospheric winds and oceanic flows in the mixed-layer satisfy the general necessary condition for ocean-atmosphere coupled instability derived first by Yamagata (1985) and applied to ENSO by Goddard and Philander (2000).

For the non-locally amplified case (Figs. 2.20b, d), coastal waves play a key role on SST anomalies through their influence on the Leeuwin Current. These waves originate in either the northern coast of Australia or the western tropical Pacific, where oceanic anomalies are mostly associated with ENSO. Since an ENSO event tends to mature generally toward the end of the year (cf. Rasmusson and Carpenter, 1982), some extent of the seasonal phase-locking

nature of Ningaloo Niño/Niña reflects this through the Clarke-Meyers effect.

The asymmetry between Ningaloo Niño and Niña may be partly related to the asymmetry between El Niño and La Niña; since El Niño events are stronger than La Niña events (Jin et al., 2003), the Clarke-Meyers effect is expected to be stronger during Ningaloo Niña than Ningaloo Niño. This seems to be consistent with the fact that the amplitude of the non-locally amplified Ningaloo Niña is larger than that of the non-locally amplified Ningaloo Niño.

We have found that warm (cold) SST anomalies in both cases induce negative (positive) SLP anomalies in the overlying atmosphere. SLP anomalies in the locally amplified case show a cell-like pattern and produce the sharp pressure gradient along the western coast with positive (negative) SLP anomalies over the continent. On the other hand, those in the non-locally amplified case show a zonally elongated band-like pattern because of the negative (positive) continental SLP anomalies. These differences in SLP anomalies over Australia are related to the variability in the Australian summer monsoon.

It is known that the intensity as well as the onset of the Australian summer monsoon is influenced by ENSO (Holland, 1986; Kajikawa et al., 2009). It is also suggested that the IOD is important in the Australian climate; a positive (negative) IOD event brings a drought (more precipitation) over south Western Australia through the atmospheric teleconnection (Ashok et al., 2003; Saji and Yamagata, 2003a; Yamagata et al., 2004), and affects the continental SLP through its influence on soil moisture. In a much shorter time scale, the Madden-Julian Oscillation (MJO; Madden and Julian, 1971, 1972) also influences the onset of the Australian summer monsoon (Hendon and Liebmann, 1990; Hung and Yanai, 2004). Since the Australian summer monsoon affects Ningaloo Niño/Niña, the three different climate drivers, ENSO, IOD, and MJO may influence Ningaloo Niño/Niña through their unique impacts on the Australian summer monsoon.

The interannual variations of SST anomalies off the western coast of Australia have

been discussed so far only in relation to ENSO (Reason et al., 2000; Feng et al., 2003; Yamagata et al., 2004; Feng et al., 2008). We must note, however, that not all Ningaloo Niño/Niña co-occurred with ENSO. Furthermore, the Ningaloo Niño in 1982/83 and 2010/11 co-occurred with very strong El Niño and La Niña, respectively. This means that Ningaloo Niño/Niña is not just a simple response to ENSO; as clearly demonstrated here, it may develop through its intrinsic unstable ocean-atmosphere interaction off the western coast of Australia. The independent nature of Ningaloo Niño/Niña will be discussed in more detail using a coupled model in Chapter 5.

Appendix: Necessary condition for instability

The method we used to assess whether or not each event satisfies the necessary condition for instability is almost the same as the one derived by Yamagata (1985). We summarize the method here. The equations of motion for ocean, linearized about a state of no motion, are

$$u_t - fv + gh_x = \gamma U \tag{2.1}$$

$$v_t + fu + gh_y = \gamma V \tag{2.2}$$

$$h_t + d(u_x + v_y) = 0, \tag{2.3}$$

where (u, v) are the zonaland meridional oceanic velocity component, h is the surface elevation, g is the acceleration due to gravity, and d is the equivalent depth. The wind stress $(\gamma U, \gamma V)$ is assumed to enter the ocean as a body force. If we take an energy integral of these equations, we obtain an energy equation:

$$\frac{1}{2}\left\langle d\left(u^2 + v^2\right) + gh^2\right\rangle_t = \gamma\left\langle d\left(uU + vV\right)\right\rangle. \tag{2.4}$$

Here, $<>$ denotes the integration with respect to x from $-\infty$ to the coast and y over a wavelength of the disturbance. Equation (2.4) suggests that a positive correlation between

atmospheric winds and oceanic currents is necessary for instability. To reduce influences from noise, we take an average over the region near the center of anomalies in our analysis: The same domain as used to derive the CWI (108-114°E, 28-22°S).

Chapter 3

Thermodynamics of Ningaloo Niño

This chapter will be submitted as:

Kataoka, T., T. Tozuka, and T. Yamagata, 2014: Generation and decay mechanism of Ningaloo Niño/Niña. *Clim. Dyn.*, (in preparation)

3.1 Introduction

In the previous chapter, using observational datasets, we have examined the mechanism of Ningaloo Niño and classified the events into the locally amplified and non-locally amplified cases based on the local alongshore wind anomalies in summer. The former was suggested to develop through an intrinsic air-sea interaction called the coastal Bjerknes feedback: An anomalous low generated by positive SST anomalies is accompanied by northerly-alongshore wind anomalies, which cause coastal downwelling anomalies and further enhance the initial SST anomalies. On the other hand, in the latter case, sea level pressure (SLP) anomalies over the Australian continent are negative as well, resulting in a band-like pattern of SLP anomalies and no anomalous alongshore-wind development. As a consequence, relative importance of the intrusion of the oceanic downwelling coastal waves originating from the western Pacific (Clarke, 1991; Clarke and Liu, 1994; Meyers, 1996), which cause positive SST anomalies through the strengthened poleward-flowing Leeuwin Current, becomes larger. In addition, we suggested that latent heat flux anomalies contribute to the growth of SST anomalies in the offshore region. Although Feng et al. (2013) suggested that the anomalously strong Leeuwin Current and surface heat flux anomalies play an important role in the generation of the massive warming in the summer of 2010/11 as well, no quantitative analyses were conducted to understand the thermodynamics of Ningaloo Niño so far.

In the present chapter, we investigate the generation and decay mechanisms of Ningaloo Niño using an ocean general circulation model (OGCM). Ningaloo Niña, the cold phase of Ningaloo Niño, is also examined. Of particular interest to us is how SST anomalies are generated and damped. Towards this end, we analyze a mixed-layer temperature (MLT) balance. The key questions to be addressed are: (1) Are there any differences in the processes involved in the evolution of the locally and non-locally amplified cases? (2) Are the

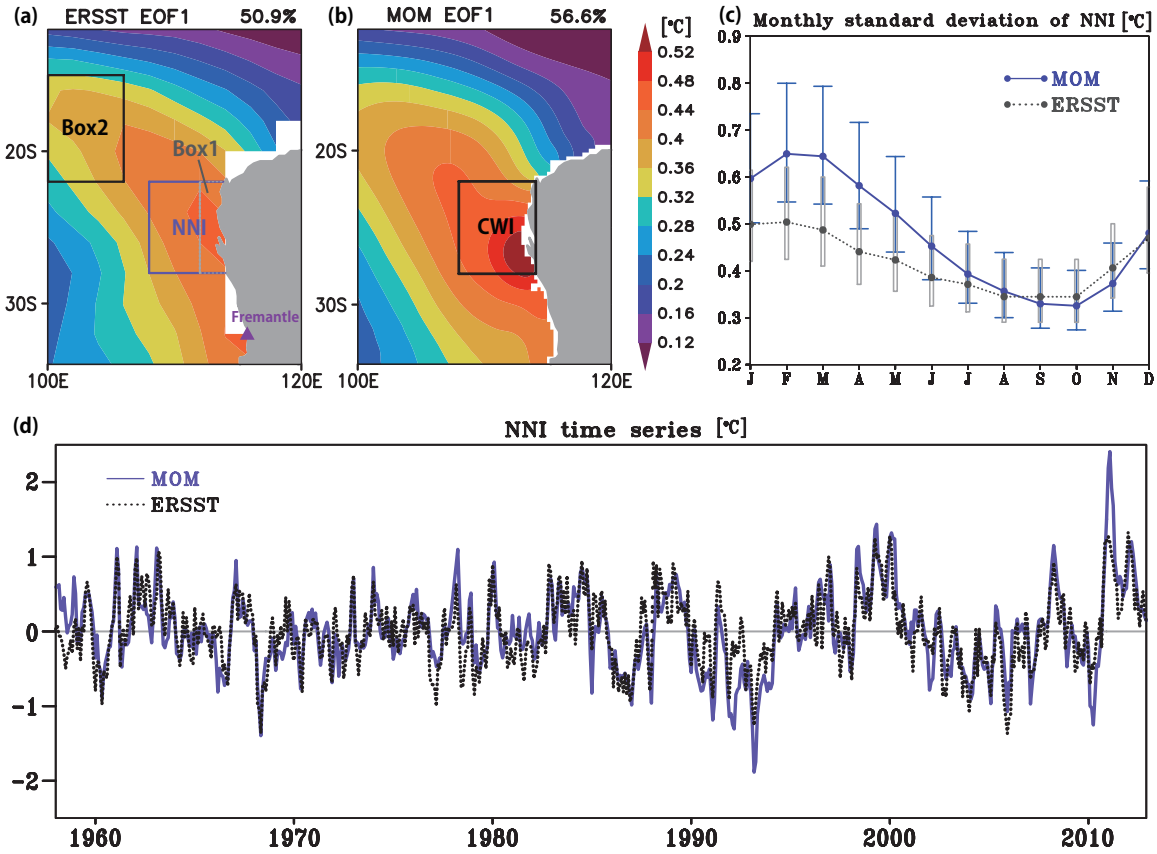

Fig. 3.1 First EOF mode of SST anomalies off Western Australia for (a) ERSST and (b) the model. Variance contribution is indicated on each panel. In panel (a), the domain used to calculated the NNI (108°E-coast, 28-22°S; blue solid) and MLT balance for the near-shore region (Box 1: 112°E-coast, 28-22°S; gray dotted) and the offshore region (Box 2: 100-106°E, 22-15°S; black solid) are indicated, whereas the domain used to define the CWI (108-114°E, 28-22°S; black solid) is superimposed in panel (b). The location of Fremantle is also indicated in panel (a) by a triangle. (c) Monthly standard deviation of the 3-month running averaged NNI (blue solid: the model, gray dotted: ERSST). Error bars represent 95% confidence intervals. (d) Time series of simulated (blue solid) and observed (black dotted) NNI.

thermodynamical aspects different between the near-shore and offshore regions? If so, what process(es) is (are) responsible in each region. The rest of this chapter is organized as follows. A description of observational and reanalysis datasets and model simulations is given in the next section. Section 3.3 describes and develops a diagnostic method for examining MLT balance. Seasonal variation is examined in section 3.4 and section 3.5 presents main results.

Conclusions and discussions are given in the final section.

3.2 Model and data

The OGCM used in this study is based on version 3.0 of the Modular Ocean Model (MOM3.0; Pacanowski and Griffies, 1999) developed at the National Oceanic and Atmospheric Administration/Geophysical Fluid Dynamics Laboratory (NOAA/GFDL). The model covers the global ocean from 65°S-65°N, where the horizontal resolution varies from 1/4° around the study region (90-160°E, 40°S-20°N) to 2° (1°) in the outer region in the zonal (meridional) direction. Within the sponge layer of 3° latitudinal width from the model northern and southern boundaries, temperature and salinity are strongly restored to the monthly climatology (Levitus and Boyer, 1994; Levitus et al., 1994) to reduce artificial wall effects. There are 25 vertical levels and the 5-minute gridded elevation data from ETOPO5 is adopted for the bottom topography and the coastlines. The lateral eddy viscosity and diffusivity are based on the formula by Smagorinsky (1963) and the parameterization of Pacanowski and Philander (1981) is used for the vertical eddy viscosity and diffusivity calculation.

The model is first spun up for 20 years from the initial state of no motion with the annual mean climatology (Levitus and Boyer, 1994; Levitus et al., 1994) by the monthly climatology of the wind stress from the National Centers for Environmental Prediction/National Center for Atmospheric Research (NCEP/NCAR) reanalysis data (Kalnay et al., 1996) and the heat flux calculated by the bulk formulae using simulated SSTs and the atmospheric variables from the reanalysis. Simulated sea surface salinities (SSSs) are relaxed to the monthly mean climatology with the restoring time scale of 30 days. Then, it is further integrated using the daily mean wind stress from the NCEP/NCAR reanalysis and daily surface heat flux calculated by the bulk formulae for 1948-2012 with the spin-up period of the first 10 years

discarded. Thus, outputs for 55 years from 1958 to 2012 are analyzed. Again, simulated SSSs are nudged to the monthly mean climatology.

For comparison, we use the Extended Reconstructed Sea Surface Temperature (ERSST) version 3b dataset (Smith et al., 2008) with 2° x 2° resolution from 1958 to 2012. Ocean currents from the Simple Ocean Data Assimilation (SODA; Carton and Giese, 2008) is adopted for 1958-2010. The sea level observations at Fremantle (115°44'E, 32°03'S; Fig. 1a) are obtained from the National Tidal Unit (NTU). Monthly climatology of mixed layer depth (MLD) from Commonwealth Scientific and Industrial Research Organisation (CSIRO) Atlas of Regional Seas (CARS; Ridgway et al., 2002) is used as well.

Linear trends are removed from the observation data and outputs from the OGCM using a least-square fit. When discussing the MLD and MLT balance, however, we retain trends to avoid artificial inversion layers.

3.3 Mixed-layer temperature balance: Physical background

The MLT balance can be calculated by

$$\frac{\partial T_{\text{mix}}}{\partial t} = \frac{Q}{\rho c_p h} - \frac{1}{h}\int_{-h}^{0} \boldsymbol{v}\cdot\nabla T dz - \frac{1}{h}\int_{-h}^{0} \nabla\cdot(\kappa\nabla T)dz + \frac{q_{-h}}{\rho c_p h} \tag{3.1}$$

(e.g. Vialard and Delecluse, 1998). Here, T_{mix} is temperature averaged over the mixed layer, ρ is the sea water density, c_p is the specific heat of the sea water, h is the MLD, which is defined as a depth at which the potential density increases by 0.01 kg/m^3 from the top model layer, $\boldsymbol{v}$ is horizontal velocity vector, T is the sea water temperature, κ is the horizontal diffusion coefficient, q_{-h} is the bottom heat flux into the mixed layer including vertical diffusion and

entrainment. Also, the net surface heat flux is given by

$$Q = Q_{\text{sw}} + Q_{\text{lw}} + Q_{\text{lh}} + Q_{\text{sh}} \tag{3.2}$$

$$= q(0) - q(-h) + Q_{\text{lw}} + Q_{\text{lh}} + Q_{\text{sh}}, \tag{3.3}$$

where $q(z)$ is the downward shortwave radiation at depth z and is parameterized by

$$q(z) = q(0)\left[R\exp\frac{z}{\gamma_1} + (1-R)\exp\frac{z}{\gamma_2}\right] \tag{3.4}$$

(Paulson and Simpson, 1977), where R (=0.58) is a separation constant, and γ_1 (0.35 m) and γ_2 (=23.0 m) are attenuation length scales. These values are for the case of water type I of Jerlov (1976). Also, Q_{sw} is the shortwave radiation absorbed in the mixed layer, and Q_{lw}, Q_{lh}, and Q_{sh} are the net surface longwave radiation, latent heat flux, and sensible heat flux into the ocean, respectively. In the rest of the chapter, we denote the surface heat flux into the ocean as positive heat flux. The first term on the RHS of Eq. (3.1) represents the contribution from the surface heat flux, but it should not be treated as a single dynamical quantity. Rather, it is a response to surface heat flux forcing and MLD variations. In general, we can decompose the contribution from the surface heat flux as

$$\left(\frac{Q}{\rho c_p h}\right)' \simeq \frac{Q'}{\rho c_p \bar{h}} - \frac{\bar{Q}}{\rho c_p \bar{h}}\frac{h'}{\bar{h}} + \text{Res}, \tag{3.5}$$

where an overbar denotes monthly climatology and a prime represents interannual anomaly. The first term on the RHS represents anomalous contribution due to surface heat flux anomaly and is referred to as "heat flux anomaly effect" for convenience. The second term on the RHS shows the sensitivity variation to the climatological surface heat flux due to the variation in heat capacity of the mixed layer associated with MLD anomaly and called "heat capacity variation effect". For example, when the mixed layer is deep, the climatological cooling by the latent heat flux weakens because of the larger mixed layer heat capacity, resulting in warm MLT anomalies if everything else remains the same. Since our focus is summer, when

the the mixed layer is shallow, we note that shortwave radiation anomaly, Q'_{sw}, may include non-negligible MLD variation effect; MLD anomalies lead to variations in the penetrative shortwave radiation at the base of the mixed layer, even if the incoming shortwave radiation at the sea surface remains the same. Since $R \sim 1 - R$ and $\gamma_2 \gg \gamma_1$, the first term on the RHS of Eq. (3.4) is influential only when h is very close to 0, giving

$$Q_{\text{sw}} = q(0)\left[1 - \left(R\exp\frac{-h}{\gamma_1} + (1-R)\exp\frac{-h}{\gamma_2}\right)\right] \tag{3.6}$$

$$\simeq q(0)\left[1 - (1-R)\exp\frac{-h}{\gamma_2}\right]. \tag{3.7}$$

Since

$$Q'_{\text{sw}} \simeq q(0)'\left[1 - (1-R)\exp\frac{-\bar{h}}{\gamma_2}\right] + \left[\overline{q(0)}(1-R)\exp\frac{-\bar{h}}{\gamma_2}\right]\frac{h'}{\gamma_2} + \text{Res}, \tag{3.8}$$

the contribution from the shortwave radiation may be decomposed into

$$\left(\frac{Q_{\text{sw}}}{\rho c_p h}\right)' \simeq \frac{q(0)'\left[1-(1-R)\exp\frac{-\bar{h}}{\gamma_2}\right]}{\rho c_p \bar{h}} + \frac{\left[\overline{q(0)}(1-R)\exp\frac{-\bar{h}}{\gamma_2}\right]\frac{h'}{\gamma_2}}{\rho c_p \bar{h}} - \frac{\overline{Q}_{\text{sw}}}{\rho c_p \bar{h}}\frac{h'}{\bar{h}} + \text{ Res.} \tag{3.9}$$

The first term on the RHS is the heat flux anomaly effect, the second term represents the effect of variation in absorption amount due to MLD anomaly ("absorption anomaly effect"), and the third term is the heat capacity variation effect for the shortwave radiation.

In a similar manner, the second term on the RHS of Eq. (3.1), the horizontal advection may be decomposed as

$$\left(-\frac{1}{h}\int_{-h}^{0} v\cdot\nabla T dz\right)' \simeq -\frac{1}{\bar{h}+h'}\int_{-\bar{h}+h'}^{0}(\bar{v}+v')\cdot(\overline{\nabla T}+\nabla T')dz + \frac{1}{\bar{h}}\int_{-\bar{h}}^{0}\bar{v}\cdot\overline{\nabla T}dz \tag{3.10}$$

$$= -\left(\frac{1}{\bar{h}+h'}\int_{-\bar{h}+h'}^{0}\bar{v}\cdot\overline{\nabla T}dz - \frac{1}{\bar{h}}\int_{-\bar{h}}^{0}\bar{v}\cdot\overline{\nabla T}dz\right)$$
$$-\frac{1}{\bar{h}}\int_{-\bar{h}}^{0}v'\cdot\overline{\nabla T}dz - \frac{1}{\bar{h}}\int_{-\bar{h}}^{0}\bar{v}\cdot\nabla T'dz + \text{Res}. \tag{3.11}$$

The sum of the first two terms represents the vertical shear of climatological horizontal advection effect ("shear effect"), where we retain second order terms only in the first term so that the physical meaning of these terms may be clearer (however, this effect turns out to be unimportant). The third term is associated with anomalous currents, which will be shown to be important during the growing phase in the near-shore region, whereas the forth term, which turns out to be effective in the decay phase, is horizontal temperature gradient anomaly effect.

The third term on the RHS of Eq. (3.1) representing the horizontal diffusion is expected to be small. Thus, we estimate the fourth term, which we refer to as a vertical term or vertical processes, as the difference between the LHS and the first two terms on the RHS.

We note that the above decomposition procedures are not applicable when nonlinearity is important and the residual terms become large.

Since SST anomalies in the coastal and offshore regions may be generated by different mechanism considering that the Leeuwin Current and coastal processes may play a role near the coast, the MLT balance is calculated in two box regions (Fig. 3.1a). Box 1 (112°E-coast, 28-22°S) is located within the Ningaloo Niño Index (NNI; Chapter 2) region (108°E-coast, 28-22°S), whereas Box 2 (100-106°E, 22-15°S) is placed away from the coast. Both boxes are located within the area where SST anomalies associated with Ningaloo Niño/Niña appear.

3.4 Seasonal cycle

Prior to examining the MLT balance during Ningaloo Niño/Niña years, we analyze the seasonal cycle of the study region. Both observed and simulated SSTs in Boxes 1 and 2 reach the maximum in late summer to early autumn and the minimum around spring (Fig. 3.2a). Also, the MLD in these regions shoals in summer, and deepens in winter (Fig. 3.2b). Although the model overestimates the MLD in winter, the MLD is realistically simulated in

summer, when Ningaloo Niño typically develops. The warming (cooling) tendency in the

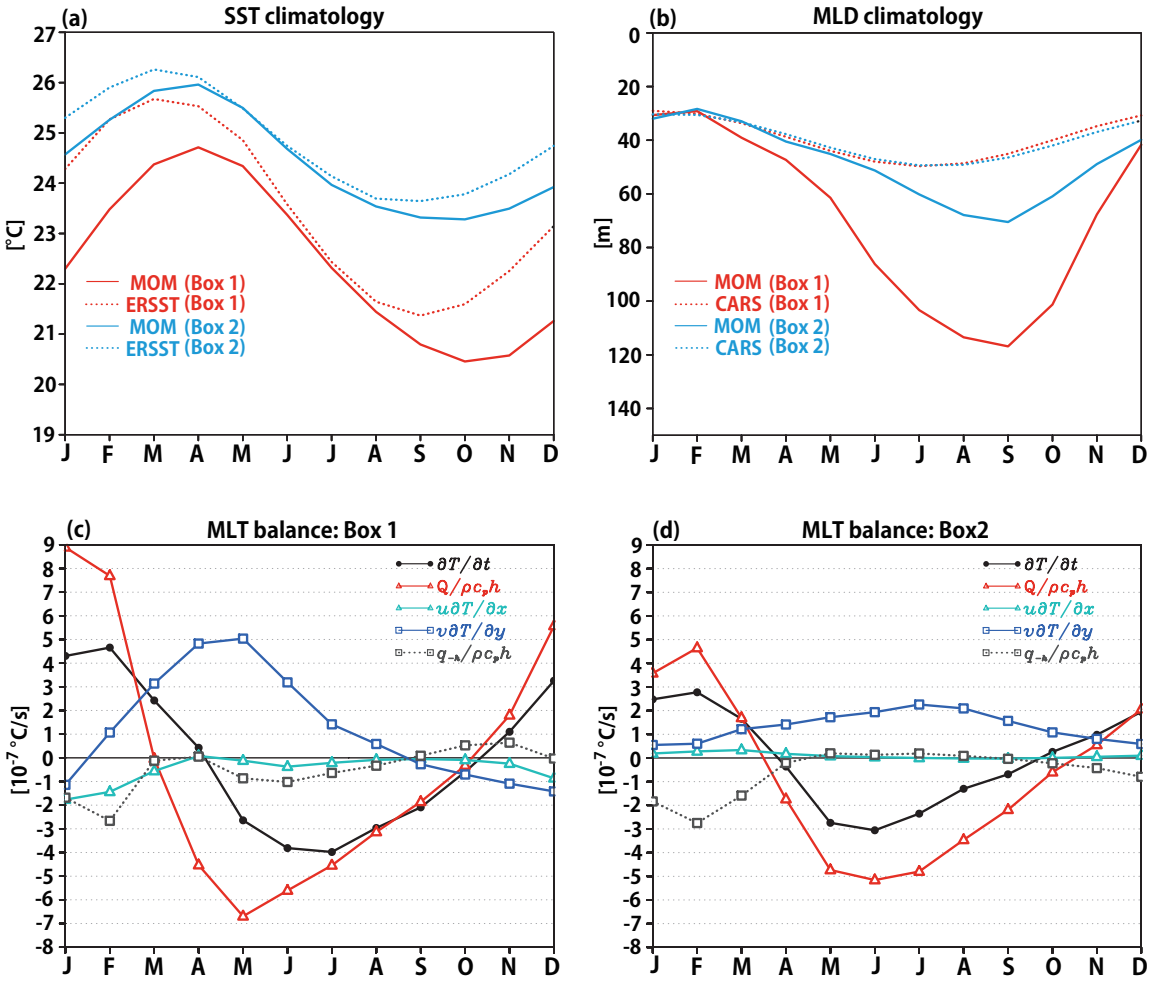

Fig. 3.2 (a) Annual cycle of SST from the model (solid line) and the observation (dotted line) for the Box 1 (red) and Box 2 (blue) regions. (b) As in (a), but for MLD. (c) Climatological MLT balance over the Box 1 region. The MLT tendency, the contribution from the surface heat flux, zonal advection, meridional advection, and vertical processes are shown in black, red, light blue, blue, and dotted gray lines, respectively.

mixed layer over both regions in summer (winter) is consistent with the seasonal cycle of SSTs (Figs. 3.2c, d). While these tendencies are explained mostly by contribution from the surface heat flux, which is dominated by the shortwave radiation (not shown), the meridional advection modulates the seasonal variation in the near-shore region during late summer to autumn because of the seasonal strengthening of the Leeuwin Current. This seasonal

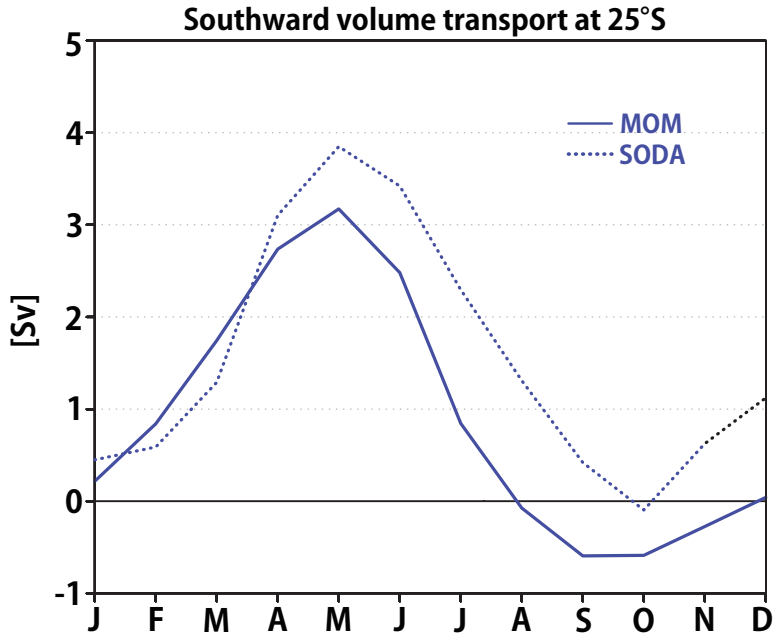

Fig. 3.3 Southward volume transport (in Sv) across 108°E-coast at 25°S from the model (solid) and SODA (dotted). Note that positive values indicate the southward transport.

strengthening is consistent with the data assimilation product (Fig. 3.3). The realistically reproduced Leeuwin Current seasonality is also verified by the high correlation coefficient of 0.92 between the simulated and observed sea level at Fremantle, which is considered to be a good proxy of the Leeuwin Current strength (Feng et al., 2003). Vertical processes contribute to the cooling during summer, when the MLD is shallowest and the vertical processes can operate efficiently.

3.5 Interannual variation: Ningaloo Niño/Niña

We begin by performing an empirical orthogonal function (EOF) analysis to extract the dominant mode of interannual variability off the west coast of Australia (100-120°E, 34-12°S; Figs. 3.1a, b). The model well reproduces the observed spatial pattern and amplitude of Ningaloo Niño. Also, the current model well simulates the observed NNI

during 1958-2012 (Fig. 3.1d) with a correlation coefficient of 0.81, partly because of its success in simulating the Leeuwin Current variability; high correlation of 0.81 is found between observed and simulated sea level at Fremantle. The standard deviation of 3-month running averaged NNI is computed to check its seasonality. Both observed and simulated NNI show high (low) variability in summer (winter), although simulated amplitude is somewhat stronger in the peak season (Fig. 3.1c). In this chapter, the Ningaloo Niño-developing year is denoted as year 0 and the following year as year 1. Because of this phase-locking nature, we define Ningaloo Niño (Niña) years as the year in which the simulated NNI averaged from January-March exceeds 1 standard deviation. This criterion leads to 13 (11) Ningaloo Niño (Niña) years (Fig. 3.4), where the years in black letters are the same as those defined in Chapter 2. The current model captures most events in Chapter 2 and only misses the 1982/83 and 1996/97 Ningaloo Niño and the 1976/77 Ningaloo Niña events for the overlapped period. Finally, we calculate the coastal wind index (CWI), which is defined by the area-average of northerly wind anomalies over the region 108-114°E and 28-22°S (Fig. 3.1b), to classify the simulated events into two cases following Chapter 2 (Fig. 3.4). Ningaloo Niño (Niña) events with the CWI exceeding 0.9 (falling below -0.9) standard deviations are classified into “locally-amplified case”, whereas others are classified into “non-locally amplified case”. Hereafter, we investigate the generation and decay mechanisms of Ningaloo Niño/Niña for both locally and non-locally amplified cases.

3.5.1 Ningaloo Niño

Figure 3.5a shows the composite of MLT balance over the Box 1 region for the locally amplified case. Significant warming is seen around summer and is primarily driven by anomalous meridional advection, which is mostly explained by strengthening of the Leeuwin Current (Fig. 3.6a). This supports our hypothesis of the local feedback based on the observation, and is also consistent with the viewpoint based on energetics (see Appendix

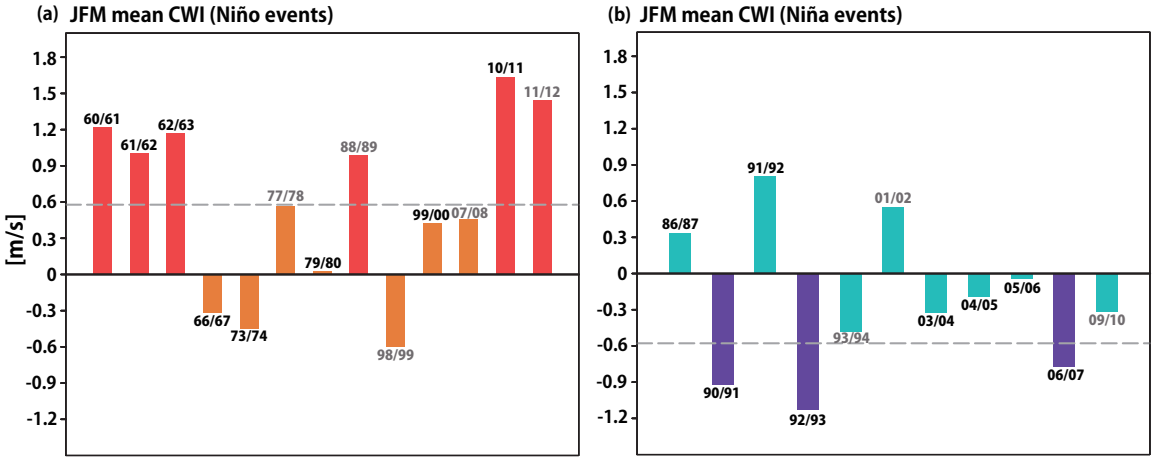

Fig. 3.4 (a) January-March (JFM) mean CWI in each Ningaloo Niño year. The dashed line represents 0.9 standard deviation of the CWI. The "locally amplified cases" are drawn in red, whereas the "non-locally amplified cases" are in orange. Years in black letters are the same as those identified in Chapter 2. (b) As in (a), but for each Ningaloo Niña year. The dashed line indicates -0.9 standard deviation of the CWI. The "locally amplified cases" are expressed in purple, whereas the "non-locally amplified cases" are in light blue.

in Chapter 2). Anomalous contribution from the shortwave radiation further enhances the warming tendency, offering another positive feedback process for the Ningaloo Niño development. This is dominated by the third term on the RHS of Eq. (3.9), the heat capacity variation effect due to MLD anomalies (Fig. 3.7a). On the other hand, vertical processes tend to cool the mixed layer. Since the residual term is generally large, Eq. (3.5) is not applicable to the vertical processes. Instead, to understand the mechanism in the variability of the vertical processes, we calculate the temperature difference (ΔT) between the MLT and the water at 10 m below the base of the mixed layer (T_{-10}; $\Delta T \equiv T_{\mathrm{mix}} - T_{-10}$). We find significant positive ΔT anomalies in January (1) and February (1) (not shown), which lead to stronger cooling by the vertical processes. The larger ΔT is a result of warmer mixed layer at the peak phase. Also, the mixed layer is more sensitive to cooling by the vertical processes owing to negative MLD anomalies (Fig. 3.7a).

The decay of warm MLT anomalies in early autumn can be explained by the sum of

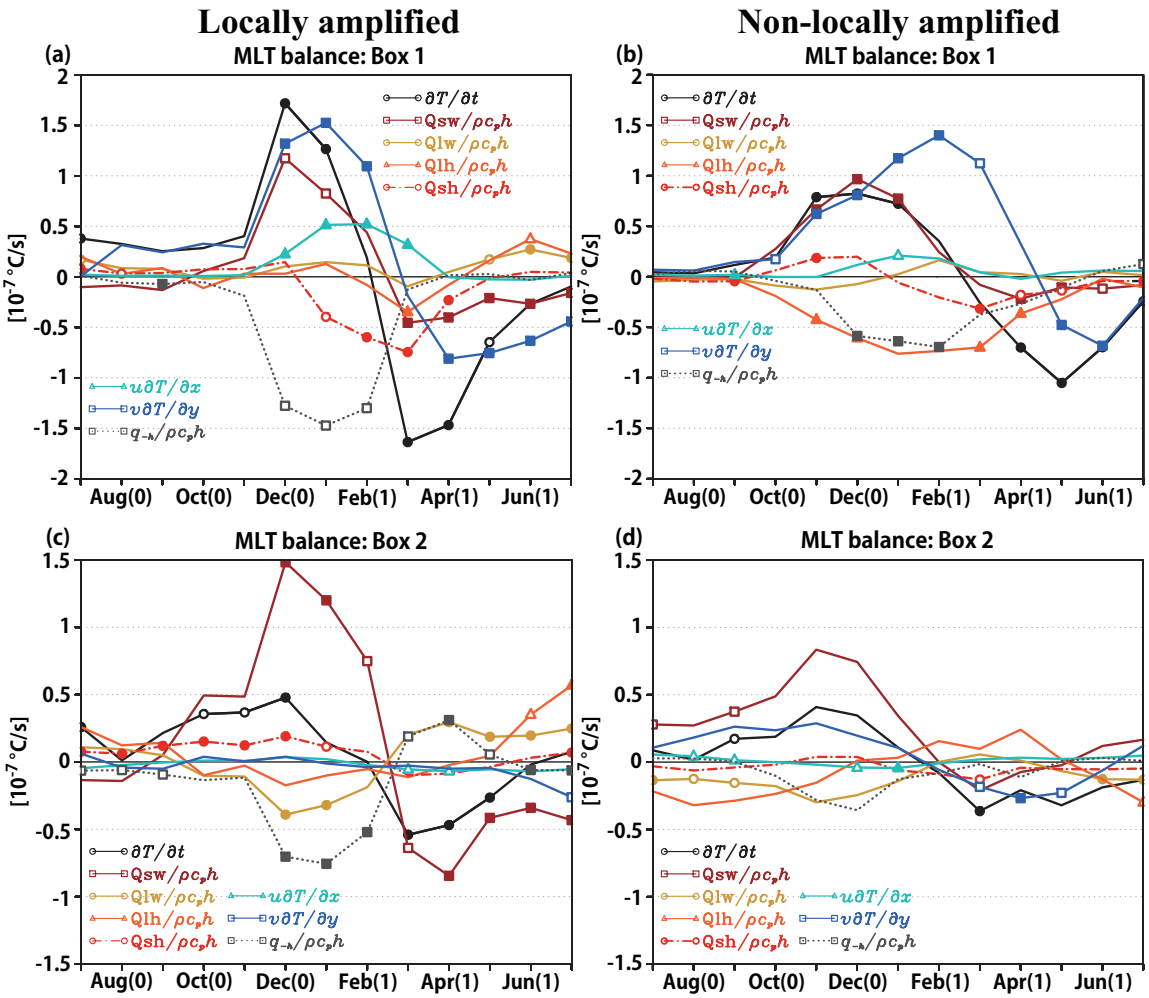

Fig. 3.5 (a) Composites of the MLT balance (in 10^{-7}°C/s) over the Box 1 region in the locally amplified Ningaloo Niño year. The MLT tendency anomaly (black solid line), the anomalous contribution from the shortwave radiation (dark-red solid line), the longwave radiation (yellow solid line), the latent heat flux (orange solid line), and the sensible heat flux (red dot-dash line), the zonal advection anomaly (light-blue solid line), the meridional advection anomaly (blue solid line), and the anomaly in the vertical processes (dark-gray dotted line) are shown. Anomalies exceeding 90% (80%) confidence level by a two-tailed t-test are indicated by filled (open) markers. A 3-month running mean is applied to smooth the time series. Note that the different vertical scales are used between the Box 1 and Box 2. (c) As in (a), but for the Box 2 region. (b, d) As in (a) and (c), respectively, but for the non-locally amplified Ningaloo Niño year. Note that 10^{-7} °C/s $\sim$ 0.26 °C/30day.

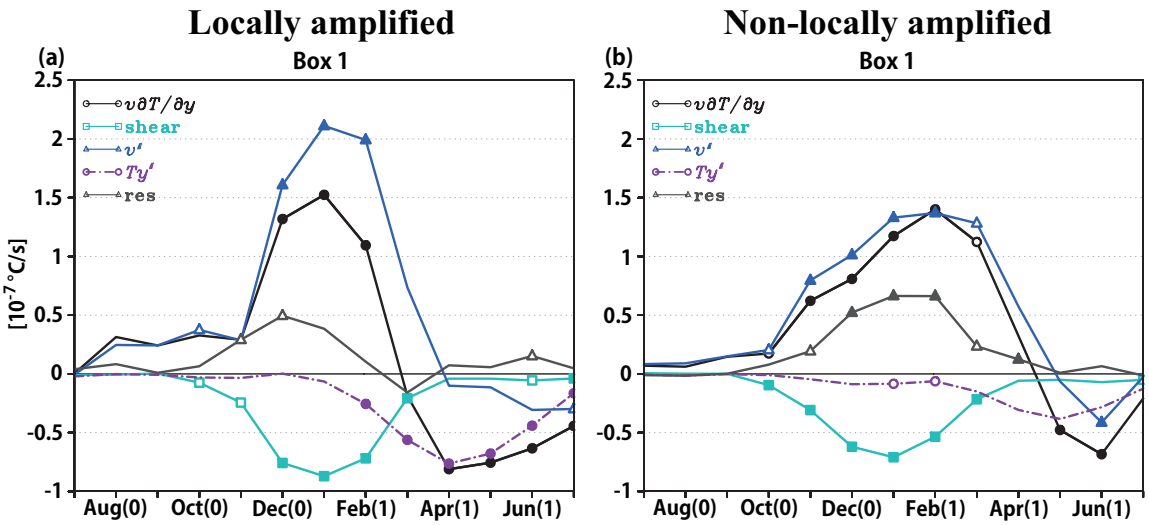

Fig. 3.6 Time series of composite anomalies of the meridional advection terms in Eq. (3.11) over the Box 1 region for (a) the locally amplified and (b) non-locally amplified Ningaloo Niño (in 10^{-7}°C/s). The meridional advection anomaly (black solid line), the climatological advection shear effect (light-blue solid line), the anomalous ocean current effect (blue solid line), the meridional temperature gradient anomaly effect (purple dot-dash line), and residual (dark-gray solid line) are shown. Filled (Open) markers show anomalies exceeding 90% (80%) confidence level by a two-tailed t-test. A 3-month running mean is applied to smooth the time series.

the anomaly in the contribution from the shortwave radiation, and latent and sensible heat fluxes. Then, relative importance of the meridional advection anomaly becomes larger. Figure 3.6a reveals that this meridional advection anomaly is associated with the weakening of the meridional temperature gradient, likely due to the preceding anomalous current. The anomalous contribution from the shortwave radiation in this phase is explained by the suppressed climatological warming associated with the deeper MLD (Fig. 3.7a). On the other hand, cooling anomaly in the latent heat is associated with the flux anomaly effect (Fig. 3.8a). We note that while anomalous latent heat flux is seen during the mature phase, its contribution is compensated by the capacity variation effect due to shoaled MLD. The latent heat flux anomaly during the peak season is caused by the reduced wind speed, and this reduction in wind speed may partly explain the shoaling of the MLD. However, as SST

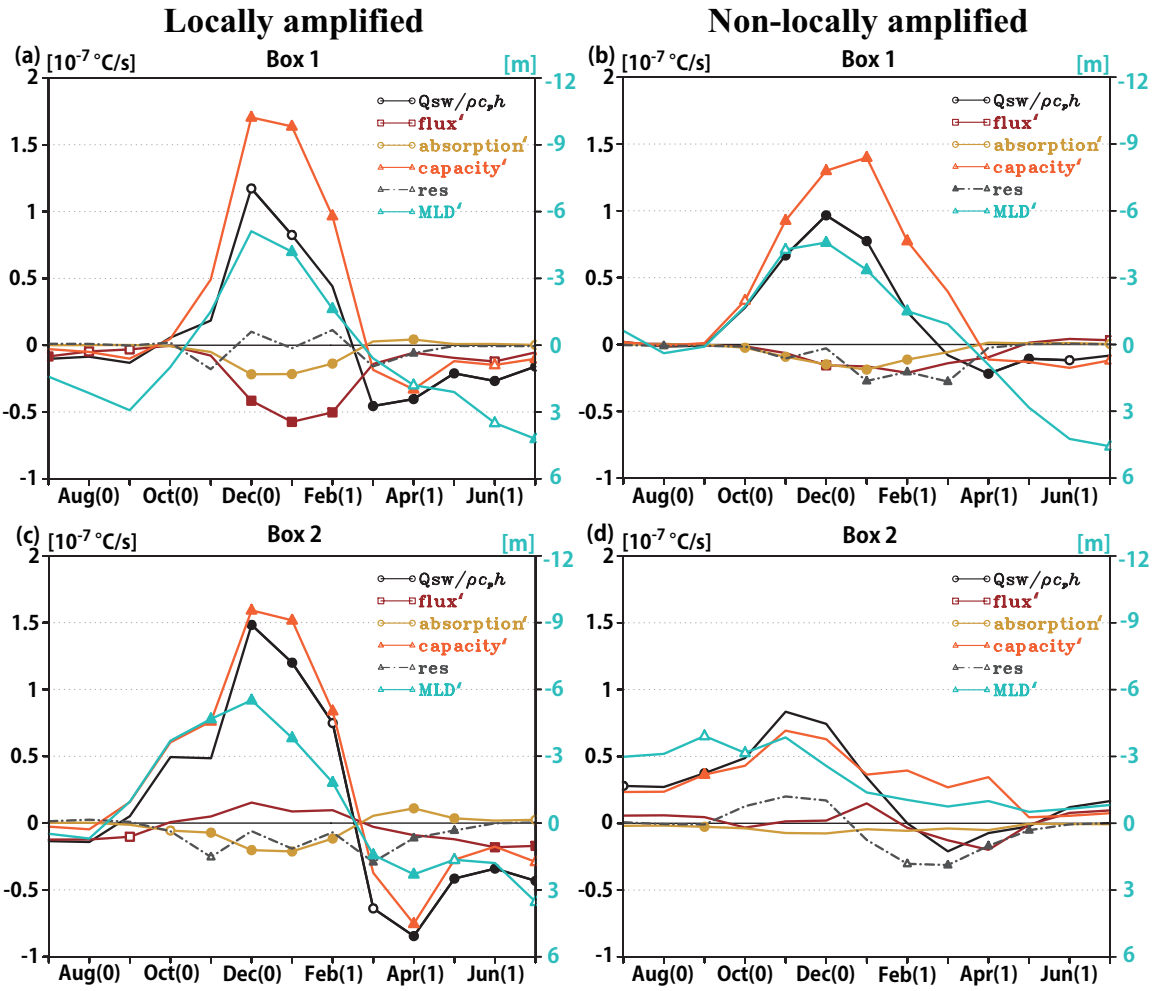

Fig. 3.7 Time series of composite anomalies of the shortwave radiation terms in Eq. (3.9) for the locally amplified Ningaloo Niño over (a) the Box 1 and (c) Box 2 regions (in 10^{-7}°C/s; left y-axis label). The total contribution anomaly (black solid line), the flux anomaly effect (dark-red solid line), the variation in absorption amount effect (yellow solid line), the heat capacity anomaly effect (orange solid line), and residual (dark-gray dot-dash line) are shown. MLD anomalies (light-blue solid line) are superimposed (in m; right y-axis label). Filled (Open) markers show anomalies exceeding 90% (80%) confidence level in a two-tailed t-test. A 3-month running mean is applied to smooth the time series. (b, d) As in (a) and (c), but for the non-locally amplified Ningaloo Niño.

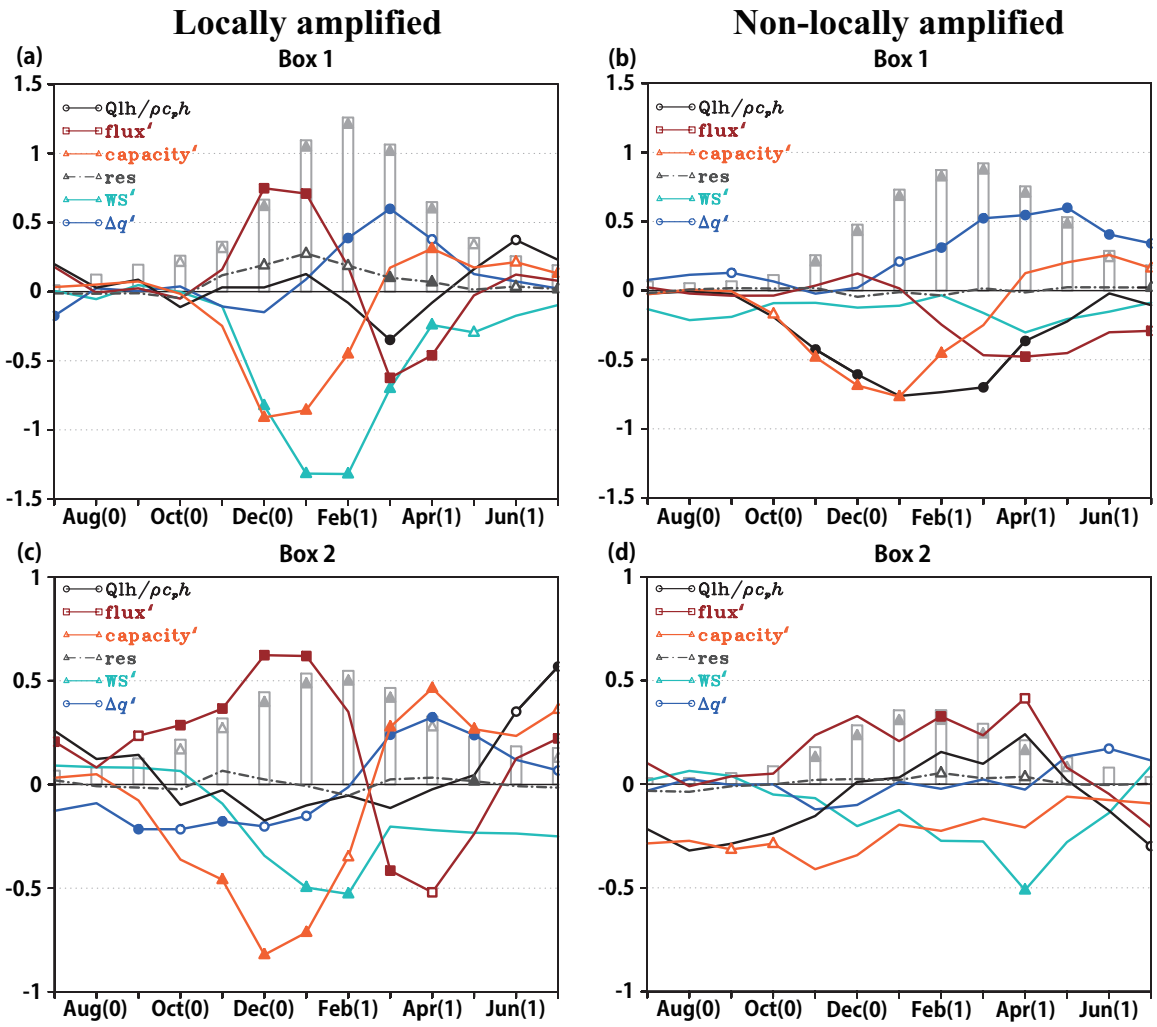

Fig. 3.8 Time series of composite anomalies of the latent heat terms in Eq. (3.5) over the Box 1 region for (a) the locally amplified and (b) the non-locally amplified Ningaloo Niño (in 10^{-7}°C/s). The total contribution anomaly (black solid line), the flux anomaly effect (dark-red solid line), the heat capacity anomaly effect (orange solid line), and residual (dark-gray dot-dash line) are shown. Wind speed (in m/s; WS; light-blue solid line), the difference between the saturated specific humidity at SST and the specific humidity at 2 m (in g/kg; Δq; blue solid line), and SST (in °C; light gray bar) anomalies are superimposed. Filled (Open) markers show anomalies exceeding 90% (80%) confidence level in a two-tailed t-test. A 3-month running mean is applied to smooth the time series. Note that the different vertical scale is used between the two regions. (c, d) As in (a) and (b), respectively but for the Box 2 region.

anomalies grow and the reduction in the wind speed is suppressed, SST response effect in surface evaporation becomes larger, which is reflected in the increase of Δq anomaly. Here, Δq denotes the difference between the saturated specific humidity at sea surface (q_s) and the specific humidity at 2 m (q_a; $\Delta q \equiv q_s - q_a$). We note that since Δq is also dependent on the atmospheric conditions, it does not simply follow SST anomalies. Thus, latent heat flux finally contributes to the damping of SST anomalies. The same technique reveals that the cooling anomaly by sensible heat flux is associated with anomalous flux (figure not shown), which is expected from higher SSTs. Over the offshore region (i.e. Box 2), the MLT tendency is mostly controlled by the contribution from the shortwave radiation during the whole life cycle (Fig. 3.5c), where MLD anomalies again play an important role (Fig. 3.7c). The vertical processes damp SST anomalies. This is due to more efficient cooling of the thinner mixed layer by the vertical processes. Also, significant positive ΔT anomaly in Feb. (1) contribute to the decay.

It is interesting to note that no significant contribution from the latent heat flux is seen, even though we suggested that latent heat flux anomalies contribute to the SST anomaly growth from their spatial pattern in Chapter 2. The balance between flux anomaly effect and the capacity effect explains this apparent contradiction as for the near-shore region. Positive latent heat flux anomalies are actually found during spring to summer and as the wind speed decreases, the anomalous flux effect increases (Fig. 3.8c). However, this is compensated by the capacity effect associated with the shallower MLD and the positive latent heat flux anomalies do not directly warm the mixed layer. In the decay season, the SST response effect becomes important in latent heat flux anomalies and they change the sign, but the capacity variation effect again compensates this term. Thus, the variation in the latent heat flux itself does not contribute to the evolution of the MLT anomalies. However, this does not mean that the latent heat flux is unimportant; through buoyancy flux, its anomalies can cause MLD variation, which plays a key role in generating SST anomalies as discussed above. In

fact, latent heat flux anomalies dominate surface heat flux anomalies (not shown) and some coherency is seen between the heat flux anomaly term of the latent heat flux (Fig. 3.8c) and MLD anomalies (Fig. 3.7c), while negative wind speed anomalies themselves may also contribute to anomalously shallow mixed layer.

Now let us consider the non-locally amplified case. Anomalies in the meridional advection and the contribution from the shortwave radiation cause warming of the mixed layer. It is found that the anomalously strong current (Fig. 3.6b) and the heat capacity variation effect for the shortwave radiation (Fig. 3.7b) are again responsible for those anomalies. Although the MLD is anomalously shallow, neither significant wind speed (Fig. 3.8b) nor net surface heat flux anomalies (not shown) are found during the developing season. The anomalous poleward current may contribute to the shallower MLD by advecting the warm and fresh water from the tropics, though its details are left for the future study. The stronger than normal vertical processes tend to cool the mixed layer during the summer, which may be due to the negative MLD anomalies. In contrast to the locally amplified case, latent heat flux contributes to damping of MLT anomalies. This difference is mostly explained by the difference in the flux anomaly effect (Figs. 3.8a, b). As expected from Fig. 3.4a, we cannot see wind speed reduction and latent heat flux anomalies for the non-locally amplified case (Fig. 3.8b). Thus, the enhanced climatological cooling is not offset as in the locally amplified case.

From late summer to autumn, the SST response effect in latent heat release becomes larger and the negative contribution from the latent heat flux takes the place of the heat capacity variation effect. Negative meridional advection anomalies contribute to the cooling at the final decay stage. This seems to be due to the combination of the weaker meridional temperature gradient and the current, though the former is not statistically significant.

For the offshore region, almost no statistically significant anomalies are found and we cannot discuss in detail (Fig. 3.5d). However, we note the importance of the enhanced

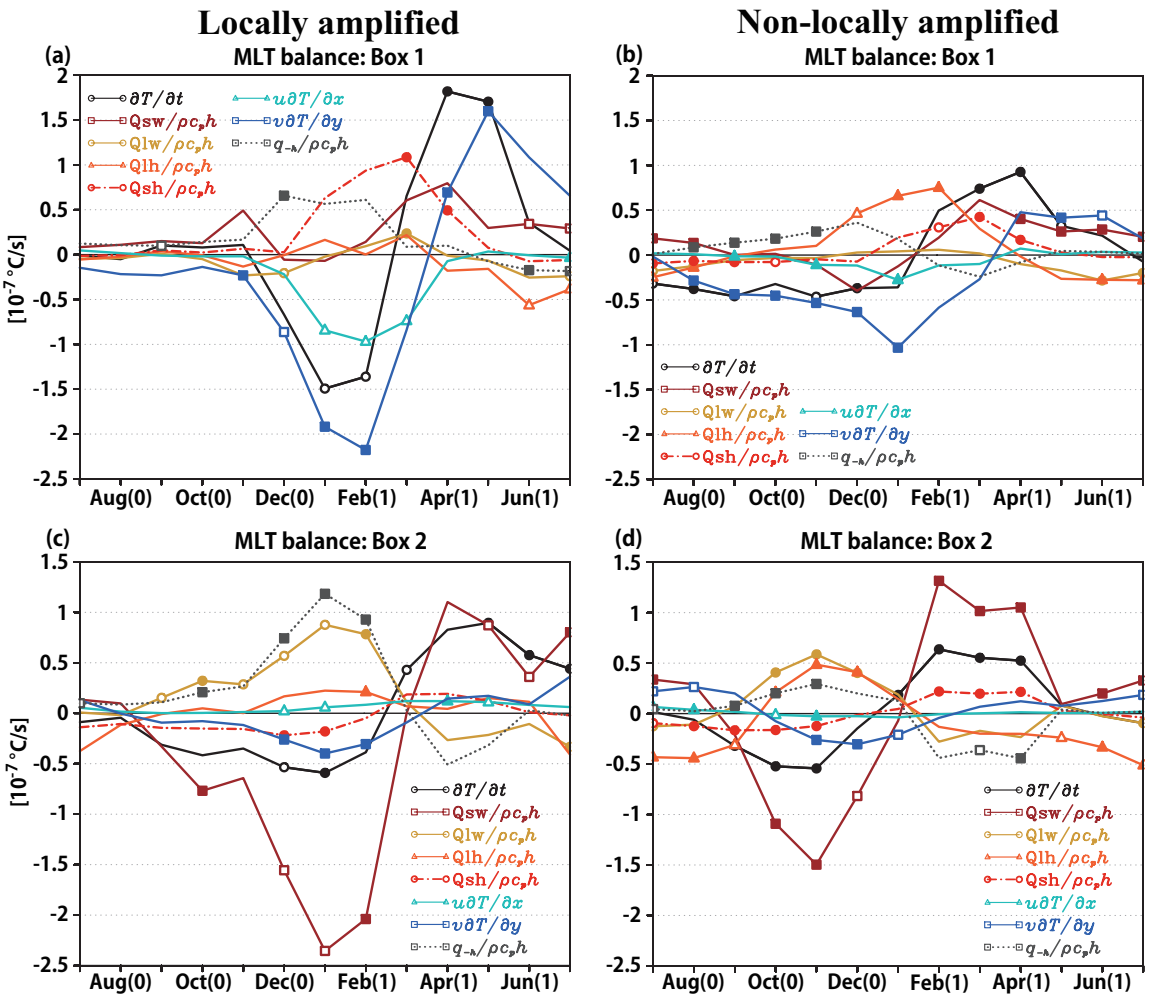

Fig. 3.9 As in Fig. 3.5, but for Ningaloo Niña. Note that only 3 Ningaloo Niña events are classified as the locally amplified case.

warming by the climatological shortwave radiation as for the locally amplified case (Fig. 3.7d).

3.5.2 Ningaloo Niña

Since only 3 Ningaloo Niña events are classified into the locally amplified case during the period of 1958-2012 (Fig 3.4b), we first discuss the non-locally amplified case and then briefly comment on the locally amplified case.

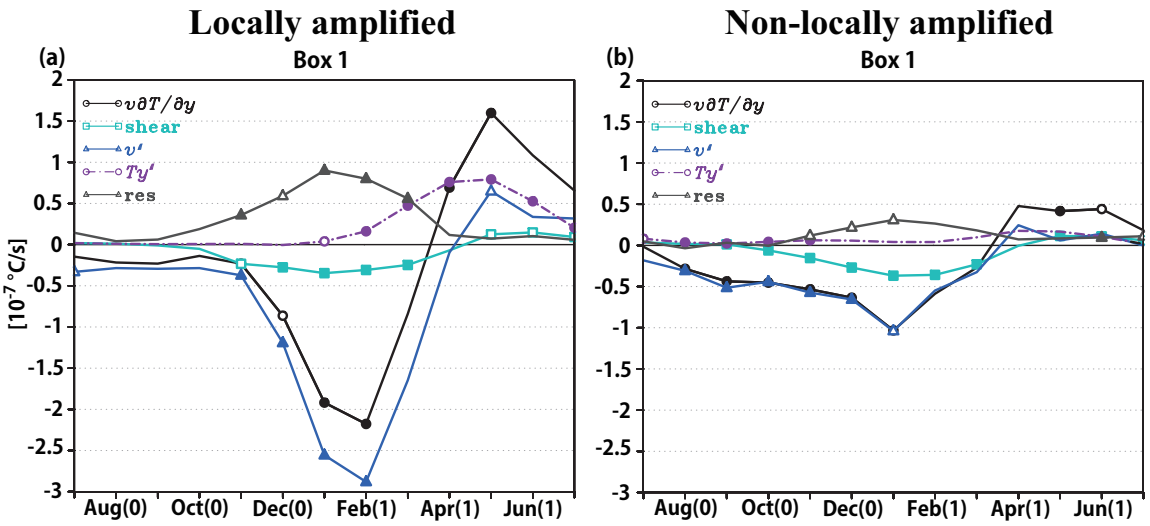

Fig. 3.10 As in Fig. 3.6, but for Ningaloo Niña.

From spring to summer, the MLT cooling is mainly caused by an anomalous meridional advection (Fig. 3.9b), which is associated with weakening of the Leeuwin Current (Fig. 3.10b). As in the non-locally amplified Ningaloo Niño case, the anomalous contribution from the latent heat flux damps the MLT anomalies around summer. This is explained by positive latent heat flux anomalies associated with the cooler SST and smaller Δq (Fig. 3.11b). As SST anomalies decay, the anomalous flux effect also becomes smaller. At the same time, MLD becomes thinner (Fig. 3.12b), which is related to positive net surface heat flux anomaly (not shown), resulting in enhanced cooling by the climatological latent heat. This heat capacity variation effect overwhelms the heat flux anomaly effect by April (1) and the anomalous contribution from the latent heat flux moderate the decay of the MLT anomalies at the very final stage. At the early stage of the decay phase, the anomalous contribution from sensible heat flux plays a role in warming. We find that this anomalous contribution is related to positive sensible heat flux anomalies due to negative MLT anomalies, though they are not significant until April (1) (not shown). The anomalous contribution from the shortwave radiation also contributes to the decay and is associated with the enhanced warming by the shallower MLD (Fig. 3.12b). At last, meridional advection anomalies seem to warm the

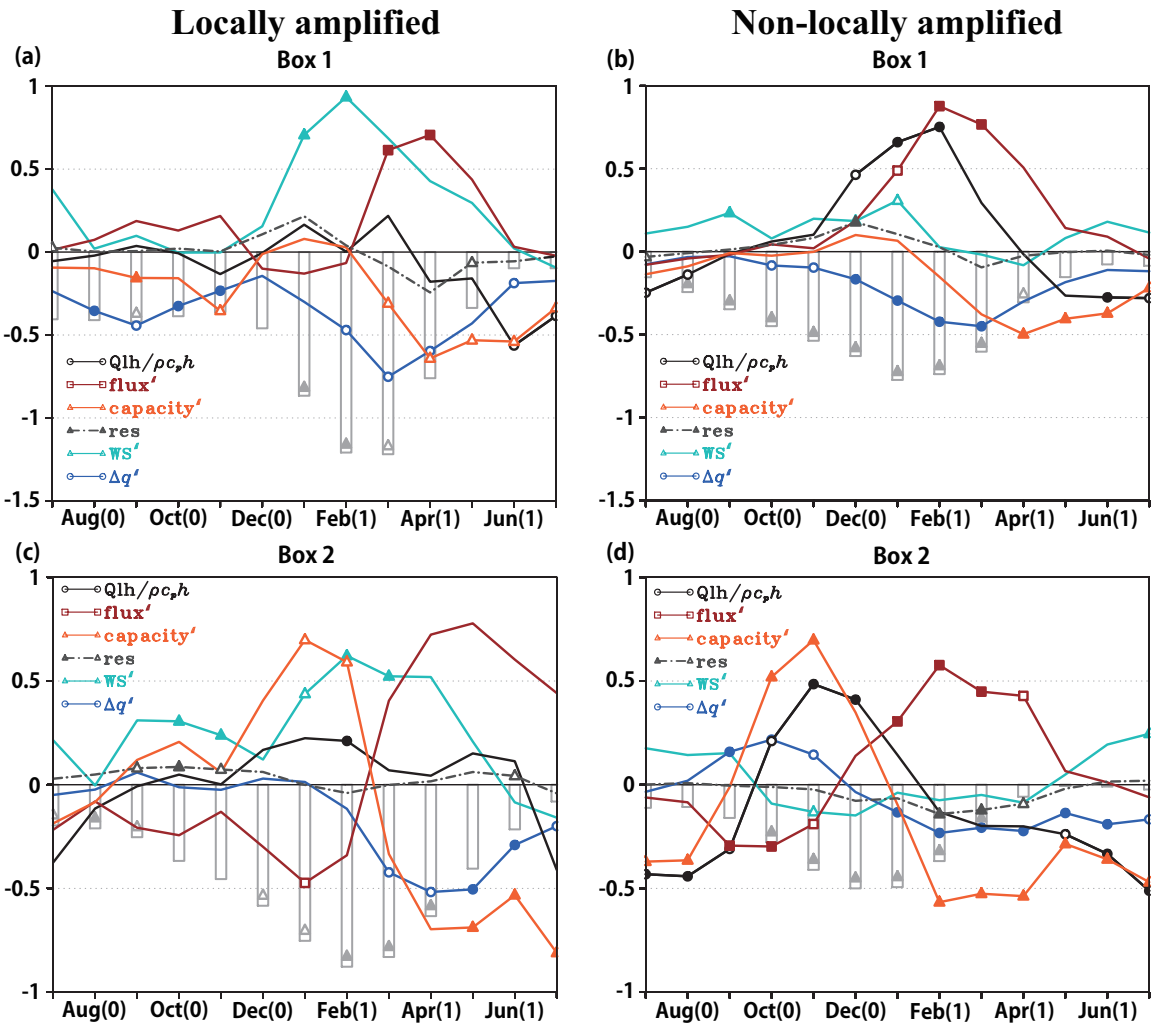

Fig. 3.11 As in Fig. 3.8, but for Ningaloo Niña.

MLT, although SST anomalies are no longer significant then.

Figure 3.9d shows the MLT balance anomaly for the offshore region. For both the growth and decay period, the MLT tendency anomaly in the Box 2 region is primarily controlled by the anomalous contribution from the shortwave radiation, which is explained by the heat capacity variation effect, highlighting the importance of MLD anomalies again (Fig. 3.12d). The MLD anomalies are related to surface heat flux anomalies (not shown). Around the peak phase, anomalous contribution from the longwave radiation tends to oppose the MLT cooling due to the combination of its suppressed climatological cooling and positive

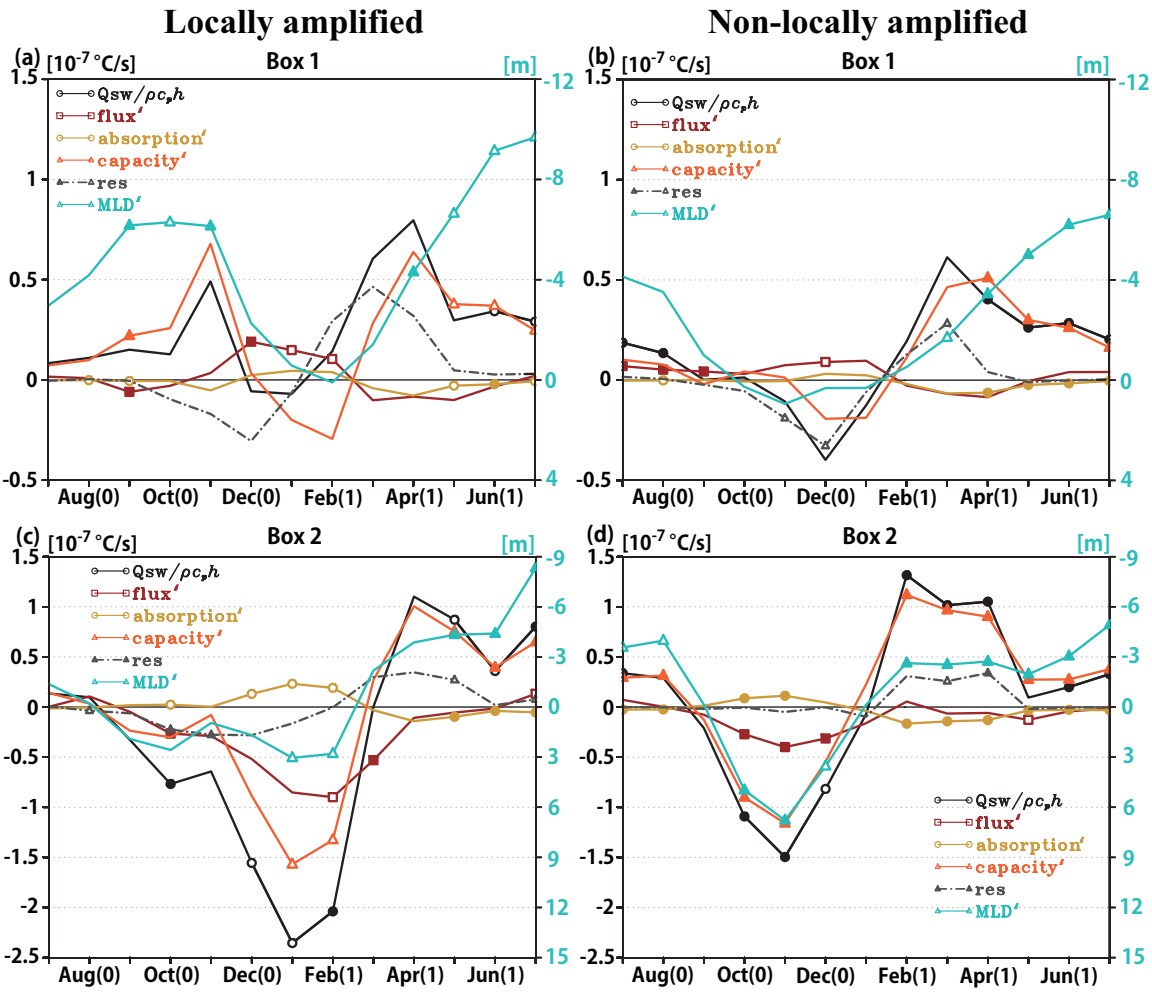

Fig. 3.12 As in Fig. 3.7, but for Ningaloo Niña. Different vertical scales are used between the two regions.

longwave radiation anomaly. Anomalous contribution from the latent heat flux also damps the MLT cooling. This is different from the inference based on the spatial pattern made in Chapter 2. This apparent discrepancy again can be understood by the decomposition of Eq. (3.5) (Fig. 3.11d). Consistent with Chapter 2, latent heat flux anomalies itself are negative, but the reduced climatological cooling associated with the deeper MLD overwhelms, resulting in damping of SST anomalies.

Although only 3 Ningaloo Niña events are classified into the locally amplified case, they are similar to non-locally amplified case; anomalous meridional advection due to weaker

Leeuwin Current is important for the near-shore region, whereas the reduced warming by the shortwave radiation owing to the deeper MLD dominates the anomalous cooling in the offshore region.

3.6 Conclusions and discussions

Using outputs from an OGCM, we have quantitatively examined the generation and decay mechanisms of SST anomalies associated with locally and non-locally amplified Ningaloo Niño/Niña. Since the near-shore and offshore regions may be governed by different processes, MLT balance is calculated separately for each region.

For the near-shore region, positive meridional advection anomalies associated with stronger Leeuwin Current and enhanced warming by climatological shortwave radiation owing to anomalously thin mixed layer contribute to the generation of both cases of Ningaloo Niño. The former result supports the existence of the coastal Bjerknes feedback, whereas the latter reveals another positive feedback process. On the other hand, negative sensible heat flux anomalies play an important role in the decay. Since the positive meridional advection anomalies during the developing phase reduce meridional temperature gradient, meridional advection anomalies eventually change their sign and also contribute to the decay.

However, there are some differences between the two cases. For the locally amplified case, anomalous northerly-alongshore winds oppose climatological southerly winds, and the resulting weaker wind speed leads to smaller latent heat loss. This is mostly cancelled out by enhanced cooling by climatological latent heat loss associated with the shallower mixed layer. This is why the latent heat flux as a whole does not contribute much to the development. For the non-locally amplified case, on the other hand, no significant wind speed anomalies are seen and thus no significant latent heat flux anomalies are found during the developing season. However, enhanced cooling by climatological latent heat loss is present. While this

enhancement weakens after the mature phase, negative latent heat flux anomalies become larger owing to the SST response effect. As a result, the latent heat flux as a whole cools the mixed layer throughout the course of the event.

The MLT tendency anomalies in the offshore region during the development (decay) phase for both cases are dominated by enhanced (reduced) warming by the climatological shortwave radiation owing to negative (positive) MLD anomalies.

It is worth mentioning possible generation mechanisms of MLD anomalies. In the near-shore region, since northerly-alongshore wind anomalies during the locally amplified Ningaloo Niño are against the climatological southerlies (Figs. 2.1b and 2.8a), wind speed is reduced and thus turbulent mixing is suppressed. On the other hand, surface wind anomalies over the offshore region for both cases oppose the background southeasterly (Figs. 2.8a and c), resulting in the suppression of wind-induced turbulence. The reduction in wind speed is also favorable for a shallower mixed layer because it tends to suppress the latent heat loss. Moister air coming from the tropics may contribute to less evaporation as well. Further analysis is needed to quantify their relative importance in the generation of MLD anomalies.

The generation and decay mechanisms for both cases of Ningaloo Niña are close to a mirror image of those for Ningaloo Niño in general. In particular, negative meridional advection anomalies associated with weaker Leeuwin Current for the near-shore region and suppressed warming by climatological shortwave radiation for the offshore region play an important role, respectively, in the development of both cases of Ningaloo Niña. However, we note that only 3 locally amplified cases occurred and we need more events to discuss their general characteristics.

This study revealed the importance of MLD anomalies, which change sensitivity of the mixed layer to the surface heat fluxes. We note that the change in sensitivity is not directly proportional to MLD anomalies, but proportional to their ratio to the climatology, as inferred from Eqs. (3.5) and (3.9). Figure 3.13 shows the standard deviation of MLD anomalies over

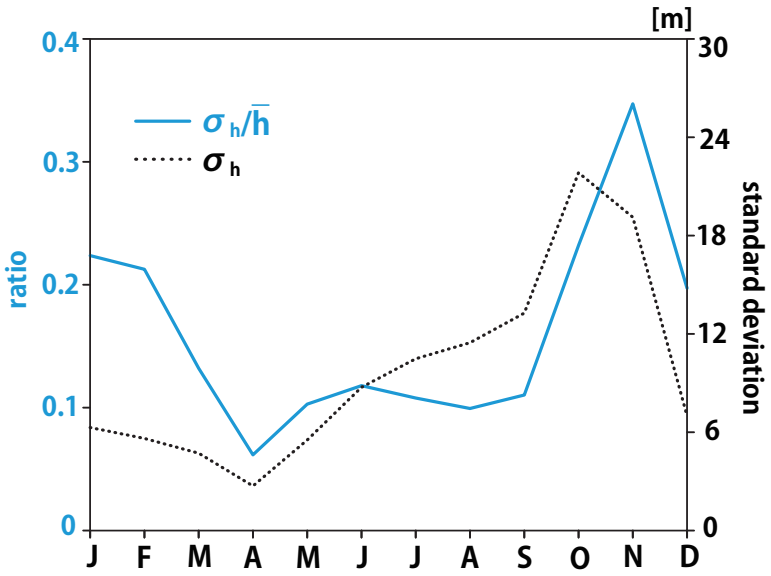

Fig. 3.13 Monthly standard deviation of the MLD over the NNI region (in m; black dotted line) and its ratio to the climatology (blue solid line).

the NNI region along with their ratio to the climatology. Although the standard deviation is relatively small during summer and fall, the ratio is large from spring to summer, when Ningaloo Niño/Niña develops. This suggests that the seasonal phase-locking nature is partly due to the seasonal variation of the MLD.

We further note that the sign as well as the amplitude of the climatological surface heat fluxes could also contribute to the phase lock. Northerly-alongshore wind anomalies, for example, may generate positive SST anomalies via strengthened meridional advection. At the same time, these northerly wind anomalies lead to a shallower mixed layer given the climatological southerly. If the climatological net surface heat flux tends to warm the mixed layer, the smaller heat capacity enhances the warming tendency anomalies. However, if the climatological net surface heat flux cools the mixed layer, it reduces, or even offsets the warming by the advection. As seen in Fig. 3.2, summer is the only season when the net surface heat flux warms the mixed layer.

Such an effect of interannual MLD variation is also crucial for development of other

climate modes such as the Atlantic Meridional Mode (Doi et al., 2010) and the Subtropical Dipole Modes (Morioka et al., 2010, 2011; Kataoka et al., 2012). The above discussion on the seasonal phase-lock may be applicable to these climate modes (e.g. Suzuki et al., 2004) and be extended even to their changes on longer timescales (e.g. Yamagami and Tozuka, 2014).

Chapter 4

Locally and remotely forced atmospheric circulation anomalies of Ningaloo Niño/Niña

This chapter has been published as:

Kataoka, T., T. Tozuka, and T. Yamagata, 2014: Locally and remotely forced atmospheric circulation anomalies of Ningaloo Niño/Niña. *Clim. Dyn.*, **43**, 2197-2205.

4.1 Introduction

In Chapter 2, we have investigated the mechanism of Ningaloo Niño/Niña using observation data and classified the phenomenon into locally and non-locally amplified cases. Intrusion of downwelling (upwelling) coastal waves propagating from the western tropical Pacific (Clarke, 1991; Clarke and Liu, 1994; Meyers, 1996) is important for the latter case. These waves cause warming (cooling) off the west coast of Australia and thus Ningaloo Niño (Niña). On the other hand, positive (negative) SST anomalies in the former are further amplified by northerly (southerly) wind anomalies along the coast. The positive (negative) SST anomalies associated with both modes of Ningaloo Niño (Niña) are suggested to generate negative (positive) sea level pressure (SLP) anomalies. These SLP anomalies form a cell-like pattern and induce alongshore northerly (southerly) wind anomalies in the locally amplified case, whereas a band-like pattern without significant alongshore wind anomalies is seen in the non-locally amplified case. The above difference in SLP anomaly patterns is due to SLP anomalies over the Australian continent associated with the interannual variations in the Australian summer monsoon (Kajikawa et al., 2009). If SLP anomalies over the ocean and the continent have the same (opposite) signs, a band-like (cell-like) pattern is formed.

On the other hand, Feng et al. (2013) suggested that a Matsuno-Gill type response (Matsuno, 1966; Gill, 1980) to La Niña induced negative SLP anomalies displaced westward from the peak SST anomalies off the Australian coast during the 2010/11 event (A pair of cyclonic (anticyclonic) anomalies that straddles the equator is generated to the west of a positive (negative) diabatic heating anomaly located on the equator. We refer to this atmospheric response as the Matsuno-Gill type response in this chapter.). They further suggested that associated northerly alongshore wind anomalies contributed to the unprecedented warming.

To enhance our understanding of Ningaloo Niño/Niña, it is necessary to examine the relative role of local and remote forcing of atmospheric circulation anomalies that play a crucial role in the development of this particular phenomenon. For this reason, we quantify the relative role of local and remote forcing using a series of numerical experiments with an atmospheric general circulation model (AGCM). Since Ningaloo Niño/Niña and ENSO are not independent of each other, we cannot use a partial regression analysis to isolate the local and remote forcing in the observational data, and use of an AGCM is reasonable for our purpose. This chapter is organized as follows. A brief description of AGCM experiments and observation data is given in the next section. In Section 4.3, we discuss atmospheric circulation anomalies from the AGCM experiments. Influences of Ningaloo Niño/Niña on precipitation anomalies over Australia are investigated in Section 4.4. Conclusions are given in the final section.

4.2 Description of AGCM experiments and observation data

The AGCM used in the present study is the atmospheric component of the University of Tokyo Coupled general circulation model (Tozuka et al., 2006, 2011; Doi et al., 2010), and is called Frontier Atmospheric General Circulation Model (FrAM; Guan et al., 2000). The horizontal resolution is T42 (triangular truncation at wavenumber 42) and there are 28 vertical levels. Physical parameterizations such as a cumulus convection scheme developed by Emanuel (1991), a land surface scheme based on Viterbo and Beljaars (1995), and a gravity wave drag scheme of Palmer et al. (1986) are used. Influences of climate variability related to the Indian Ocean Dipole and ENSO on regional climate is relatively well captured by the FrAM (Yuan et al., 2012; Tozuka et al., 2014). More details on this model can be

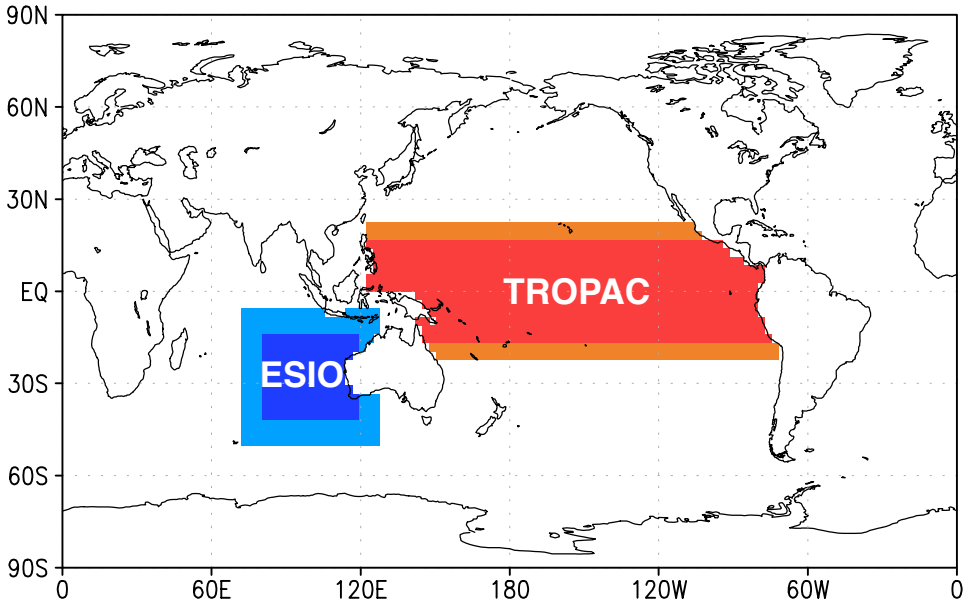

Fig. 4.1 Domain where SST is allowed to vary interannually in the ESIO experiment (blue shading). The imposed SST anomalies in the eastern South Indian Ocean are linearly decreased to zero in areas with light blue shading. Also shown is the domain where SST is allowed to vary interannually in the TROPAC experiment (red shading). The imposed SST anomalies in the Pacific are linearly decreased to zero in areas with orange shading.

found in papers by Guan et al. (2000) and Tozuka et al. (2014).

Four experiments with five ensemble members are conducted in this chapter. In the control (CTRL) run, the AGCM is forced with monthly fields of SST and sea ice cover observed for 1951-2011, as in the Atmospheric Model Intercomparison Project (AMIP) simulations (Hurrell et al., 2008). To examine the impact of local SST anomalies, we have conducted an ESIO experiment, where SST is allowed to vary interannually only in the eastern South Indian Ocean (shown by blue shading in Fig. 4.1) and the monthly climatology of SST is imposed elsewhere. The imposed SST anomalies in the eastern South Indian Ocean are linearly decreased to zero in areas with light blue shading in Fig. 4.1. In addition, a NOESIO experiment is conducted to examine influences from SST anomalies outside of the eastern South Indian Ocean. In contrast to the ESIO experiment, the imposed SST varies interannually only outside of the eastern South Indian Ocean and the monthly climatology is

prescribed in the eastern South Indian Ocean. To isolate impacts from tropical Pacific in the NOESIO experiment, we have also conducted a TROPAC experiment, where SST is allowed to vary interannually only in the tropical Pacific (red and orange shading in Fig. 4.1). To construct five ensemble members for each experiment, the AGCM integration is repeated with different initial conditions. If we were to discuss each Ningaloo Niño/Niña event separately, five members might be too small. However, since our focus in this study is on general features of Ningaloo Niño/Niña and composites of anomalies in AGCM experiments are based on number of events times five ensemble members, this number is adequate to filter out atmospheric internal variability.

For SST data, the Extended Reconstructed Sea Surface Temperature (ERSST) version 3b dataset (Smith et al., 2008) with 2° x 2° resolution are also used, to compare our results with those of Chapter 2. We use the National Centers for Environmental Prediction (NCEP)/National Center for Atmospheric Research (NCAR) reanalysis data (Kalnay et al., 1996) for SLP and zonal and meridional wind velocities for the period between 1951 and 2011. For precipitation data, we use the version 6 of Global Precipitation Climatology Centre (GPCC) monthly precipitation dataset (Schneider et al., 2011) from 1951 to 2010 with 1°x1° horizontal resolution. Linear trends are removed from all observation data and model outputs using least-square fit.

4.3 Atmospheric circulation anomalies

Figure 4.2 shows the time series of the Ningaloo Niño Index (NNI) in December-February (DJF) from both the ERSST used in Chapter 2 and the AMIP SST used to force the AGCM. Here, the NNI is defined as area-averaged SST anomalies off Western Australia (108°E-coast, 28°S-22°S; see boxes in Fig. 4.3) and we focus on DJF because the phenomenon peaks during this season (Chapter 2). The correlation coefficient

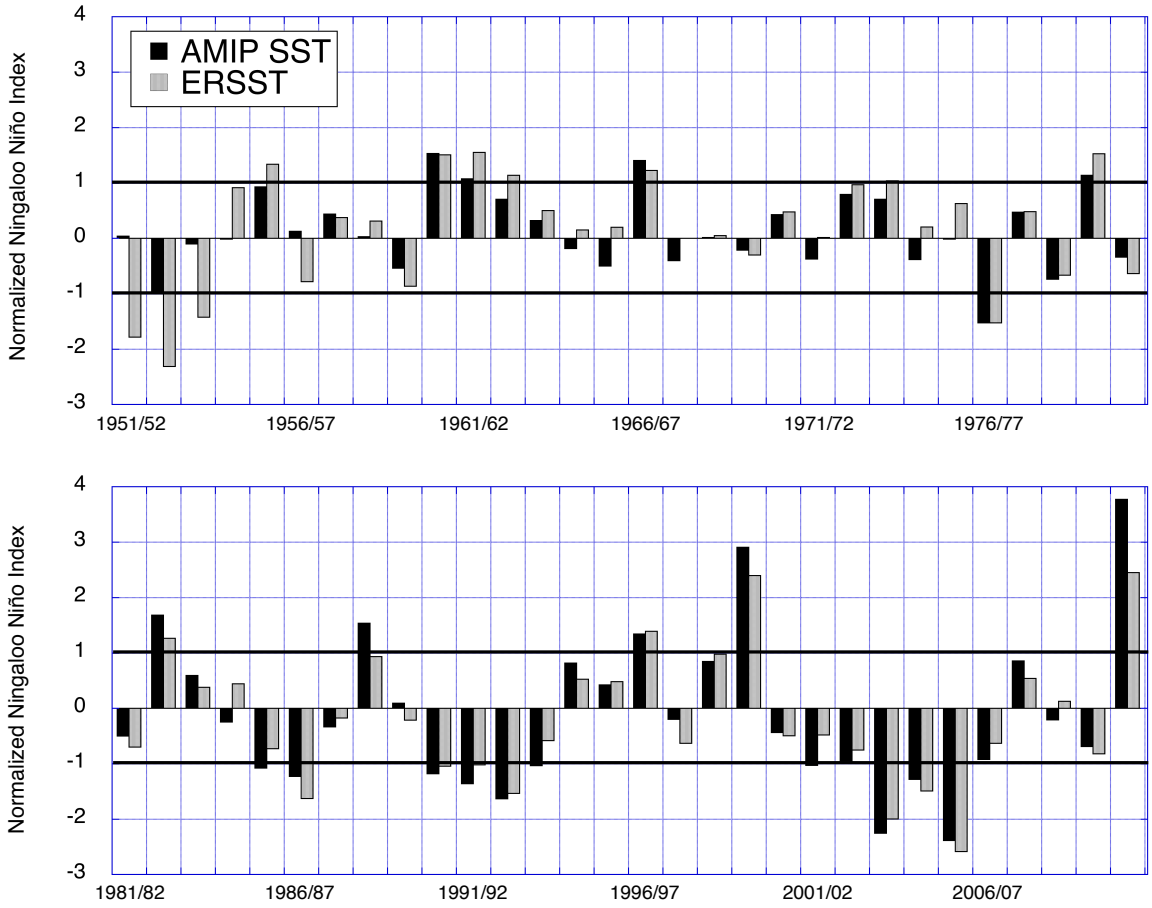

Fig. 4.2 Time series of the normalized Ningaloo Niño Index (NNI) in December-February from the AMIP SST (black bars) and the ERSST (gray bars).

between these two time series is 0.89. Anomalous years in which the NNI in DJF is above +1 standard deviation for both datasets are defined as Ningaloo Niño years and below -1 standard deviation are defined as Ningaloo Niña years. As a result, we have eight events for both Ningaloo Niño and Niña and those are listed in Table 4.1. Although 1982/83 is classified as a Ningaloo Niño year, it is the only event that co-occurred with a strong El Niño event in the Pacific Ocean and very different from other events (Chapter 2). Although understanding of the peculiar event in 1982/83 is an interesting topic, it is beyond the scope of this thesis and we exclude 1982/83 from the composite analysis in the rest of this chapter.

Composites of SST anomalies in DJF based on the AMIP SST are presented in Fig. 4.3

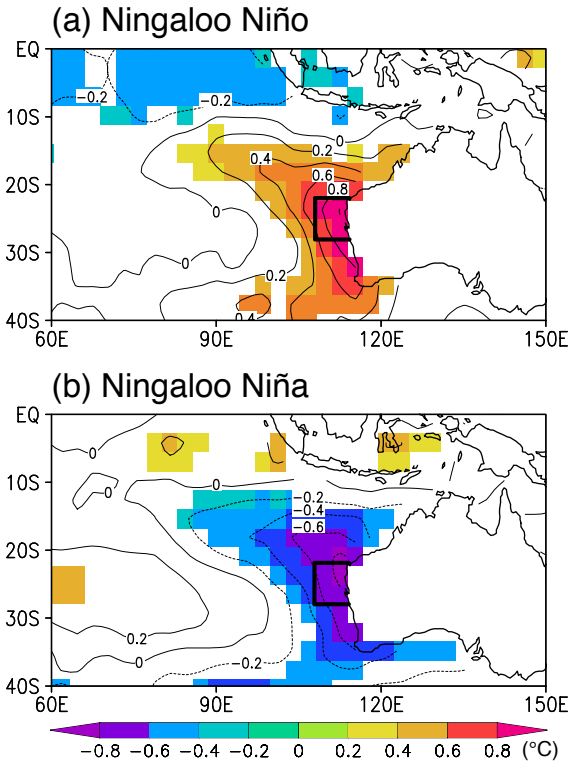

Fig. 4.3 Composites of SST anomalies in DJF for (a) Ningaloo Niño and (b) Ningaloo Niña. Contour interval is 0.2°C and anomalies significant at 95% confidence level by a two-tailed t-test assuming six and seven degrees of freedom (number of events minus one) for Ningaloo Niño and Niña, respectively, are shaded. The domain (108°E-coast, 28°S-22°S) used to define the NNI is shown by boxes.

Table 4.1 Years of Ningaloo Niño and Niña. The event in 1982/83 is excluded from composites for the reason stated in the text.

	Years
Ningaloo Niño	1960/61, 1961/62, 1966/67, 1979/80, (1982/83), 1996/97, 1999/2000, 2010/11
Ningaloo Niña	1976/77, 1986/87, 1990/91, 1991/92, 1992/93, 2003/04, 2004/05, 2005/06

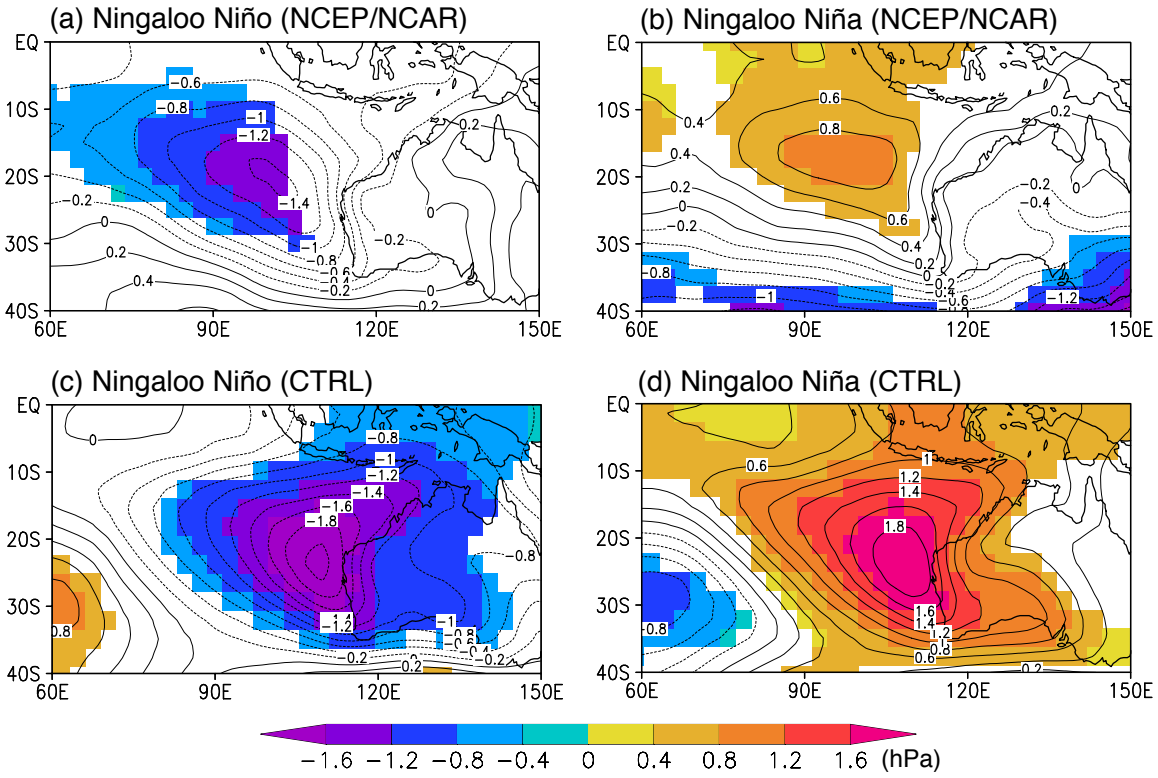

Fig. 4.4 Composites of SLP anomalies in DJF for (a), (b) NCEP/NCAR reanalysis data, and (c), (d) the CTRL run of the FrAM. Left panels are composites of Ningaloo Niño and right panels are those of Ningaloo Niña. Contour interval is 0.2 hPa and anomalies significant at 90% confidence level by a two-tailed t-test are shaded. Note that composite diagrams of anomalies from the AGCM in Ningaloo Niño (Niña) years are constructed using 35 (40) anomaly fields (i.e. seven (eight) events times five ensemble members), but since five anomaly fields for an event is not totally independent, we have assumed six (seven) degrees of freedom to be on the conservative side.

for Ningaloo Niño/Niña. Both Ningaloo Niño and Niña are associated with SST anomalies that are attached to the west coast of Australia and extending to the northwest in the southeastern Indian Ocean. Their peak anomalies are 1.0°C and -0.85°C, respectively. The stronger peak SST anomalies during Ningaloo Niño are related to skewness of Ningaloo Niño/Niña; skewness of the NNI in DJF is 0.67.

To check whether the current AGCM can reproduce atmospheric circulation anomalies associated with Ningaloo Niño/Niña, we have constructed composite diagrams of SLP

anomalies (Fig. 4.4). Ningaloo Niño is associated with negative SLP anomalies off the west coast of Australia with the peak value of about -1.4 hPa (Fig. 4.4a). The CTRL run well reproduces the spatial pattern, although the peak amplitude of SLP anomalies is larger by 0.6 hPa (Fig. 4.4c). On the other hand, Ningaloo Niña is associated with positive SLP anomalies with the maximum of about 0.8 hPa (Fig. 4.4b). The model is also successful in reproducing the positive SLP anomalies, although the amplitude is twice as strong compared with the reanalysis data and the center is located slightly to the southeast of the observed position (Fig. 4.4d). Therefore, the model has good skills in simulating SLP anomalies associated with Ningaloo Niño/Niña, although the model is not successful in reproducing strong asymmetry in the amplitude of SLP anomalies. Nevertheless, due to the relatively good agreement between the model and the reanalysis data, we expect that this model can provide useful insight into the atmospheric circulation anomalies associated with Ningaloo Niño/Niña.

To quantify the relative contribution from local and remote forcing on SLP anomalies, we have compared composite diagrams of SLP anomalies in the ESIO and NOESIO experiments (Fig. 4.5). For Ningaloo Niño, peak SLP anomalies of about -0.7 hPa is obtained for the ESIO experiment and about -1.5 hPa is obtained for the NOESIO experiment. On the other hand, for Ningaloo Niña, the maximum SLP anomalies are about 0.5 and 1.8 hPa in the ESIO and NOESIO experiments, respectively. This suggests that SST anomalies both inside and outside of the eastern South Indian Ocean are important in generating negative (positive) SLP anomalies associated with Ningaloo Niño (Niña), but the latter has a larger contribution. It is interesting to note that negative SLP anomalies associated with Ningaloo Niño are stronger in amplitude compared with positive SLP anomalies associated with Ningaloo Niña in the ESIO experiment. This may be explained by the fact that the NNI is positively skewed with stronger (weaker) Ningaloo Niño (Niña).

Since ENSO is the most dominant mode of interannual climate variability, it is

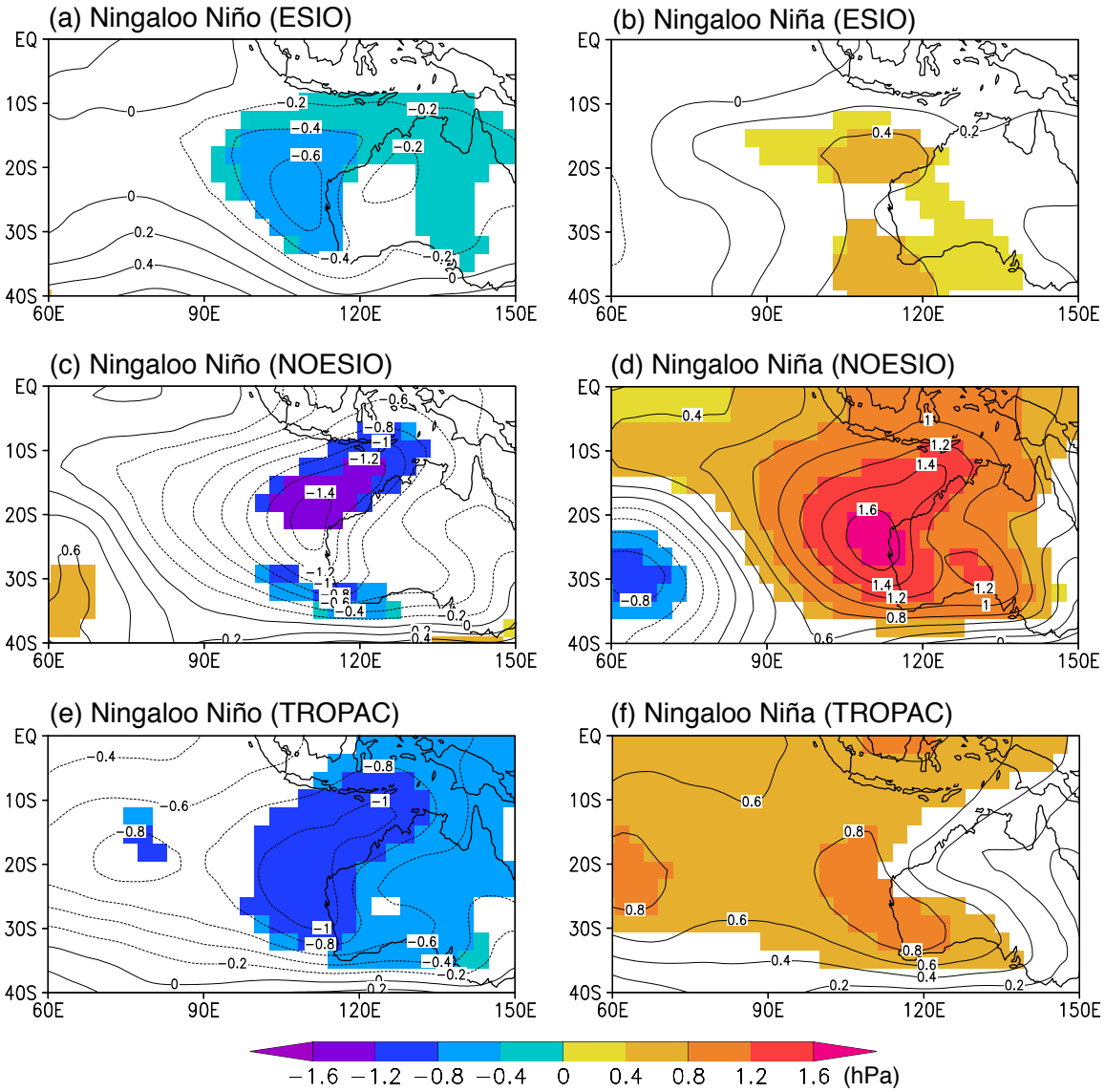

Fig. 4.5 As in Fig. 4.4, but for (a), (b) ESIO, (c), (d) NOESIO, and (e), (f) TROPAC experiments.

reasonable to expect that SLP anomalies seen in the NOESIO experiment are associated with ENSO in the tropical Pacific. For this reason, we have constructed composites of SLP anomalies simulated in the TROPAC experiment (Figs. 4.5e, f). The spatial pattern of SLP anomalies are similar to that in the NOESIO experiment and the minimum (maximum) SLP anomaly off the west coast of Australia in the TROPAC experiment is 78% (56%) of that in the NOESIO experiment. The SLP anomaly pattern resembles that of the Matsuno-Gill type

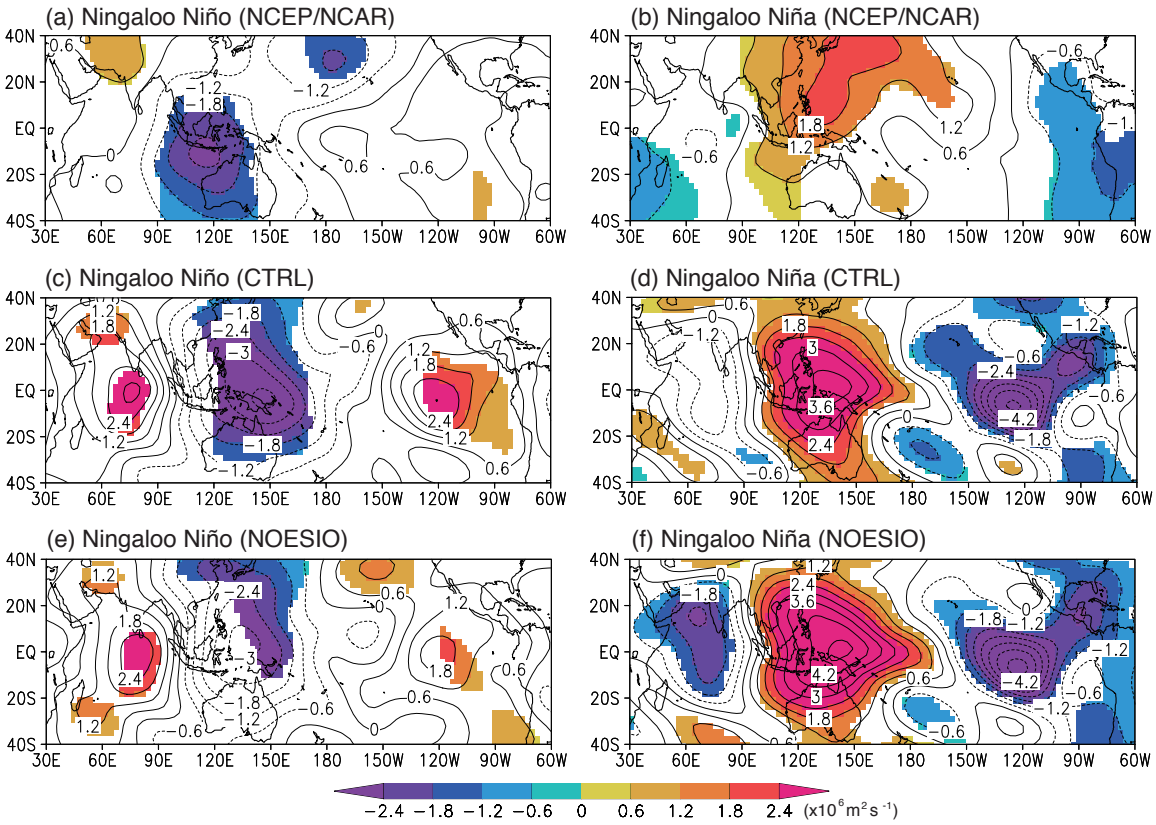

Fig. 4.6 Composites of velocity potential anomalies at 200 hPa in DJF for Ningaloo Niño (left column) and Niña (right column): (a), (b) NCEP/NCAR reanalysis data, (c), (d) CTRL run, and (e), (f) NOESIO experiment. Contour interval is 0.6x10^6 m^2 s^{-1} and anomalies significant at 90% confidence level by a two-tailed t-test are shaded.

response (Feng et al., 2013).

We note that stronger contribution of the remote forcing may partly be due to an exaggerated atmospheric response in the western tropical Pacific. Composites of velocity potential anomalies at 200 hPa in DJF of Ningaloo Niño (Niña) years show that the minimum (maximum) velocity potential is only about -2.4x10^6 (1.8x10^6) m^2 s^{-1} in the NCEP/NCAR reanalysis data, but the minimum (maximum) is -3.6x10^6 (3.6x10^6) m^2 s^{-1} and -3x10^6 (4.8x10^6) m^2 s^{-1} in the CTRL and NOESIO experiments, respectively (Fig. 4.6). We note that the minimum (maximum) velocity potential anomaly is about -1.4x10^6 (1.5x10^6) m^2 s^{-1} in the European Centre for Medium-Range Weather Forecasts (ECMWF) 40-year

Re-analysis (ERA-40) data (Uppala et al., 2005) (figure not shown), which is similar to that of the NCEP/NCAR reanalysis data.

4.4 Impacts on precipitation

Although we constructed composites of precipitation anomalies using observation data in Chapter 2 and suggested possible impacts of Ningaloo Niño/Niña on precipitation over Australia, it was not possible to isolate the impacts related to SST anomalies associated with Ningaloo Niño/Niña off the west coast of Australia. Thus, it will be interesting to examine precipitation anomalies simulated in our model experiments. In agreement with Chapter 2, positive (negative) precipitation anomalies are found in the northwestern part of Australia in Ningaloo Niño (Niña) years in the observation (Figs. 4.7a, b). Precipitation anomalies simulated in the CTRL run also shows wet (dry) anomalies in the northwestern part of Australia in Ningaloo Niño (Niña) years (Figs. 4.7c, d) as in the observation. Precipitation anomalies in the CTRL run are more widespread and covers majority of the Australian continent (Figs. 4.7c, d). This may be explained by strong precipitation anomalies induced by SST anomalies outside of the eastern South Indian Ocean (Figs. 4.7g, h), particularly those associated with ENSO in the Pacific. La Niña (El Niño), which tends to co-occur with Ningaloo Niño (Niña), induces widespread positive (negative) precipitation anomalies over the Australian continent and as discussed in the previous section, this influence may be overestimated in our AGCM. When only SST anomalies over the eastern South Indian Ocean are imposed, positive (negative) precipitation anomalies are seen in the northwestern part of Australia (Figs. 4.7e, f). Therefore, Ningaloo Niño/Niña itself can also cause precipitation anomalies in northwestern Australia. However, precipitation anomalies are weaker in the ESIO experiment than in the NOESIO experiment. Also, we note that precipitation anomalies are more significant in Ningaloo Niño years compared with Ningaloo Niña years, which may

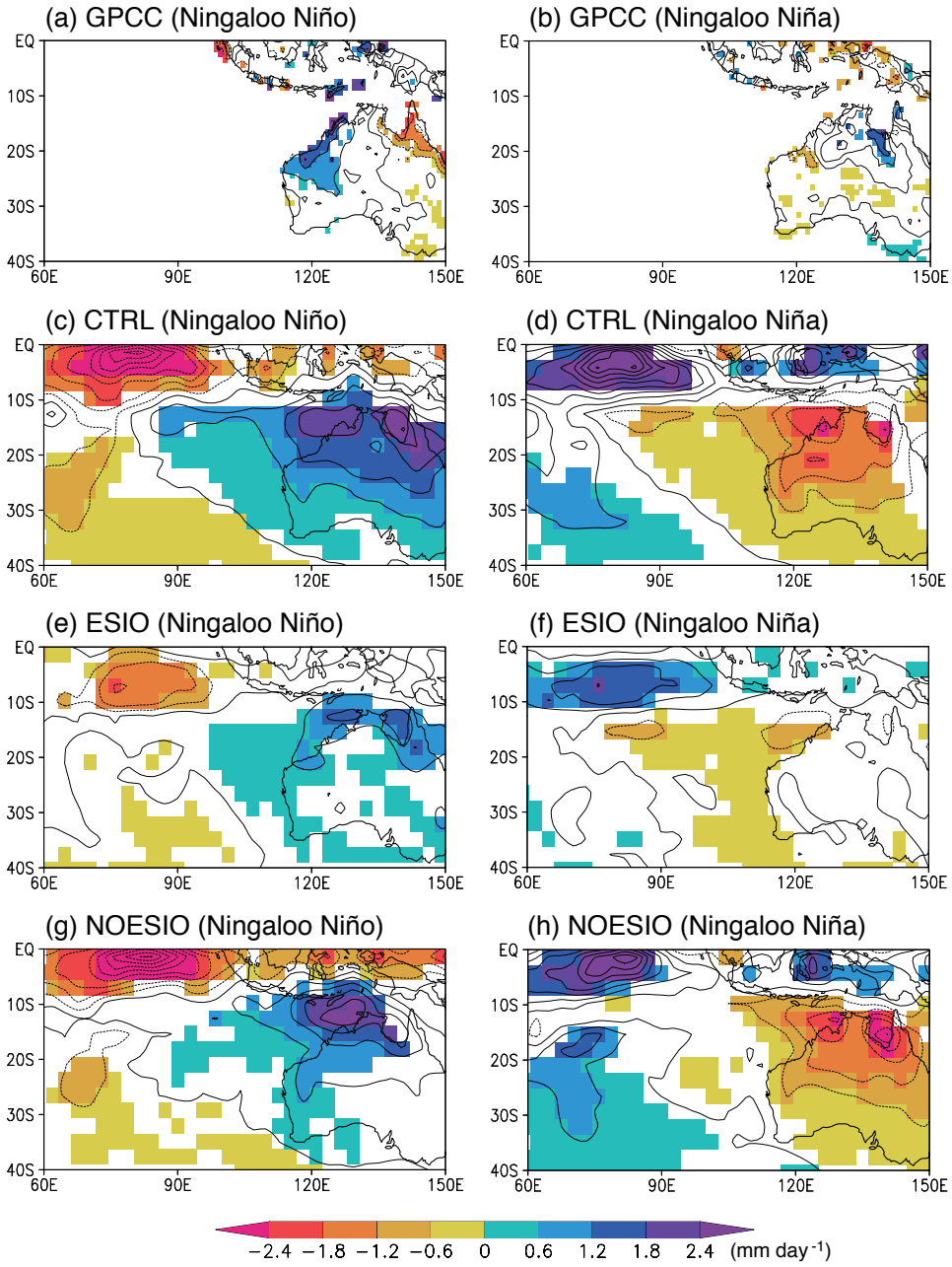

Fig. 4.7 Composites of precipitation anomalies in DJF for (a), (b) GPCC data, and (c), (d) CTRL, (e), (f) ESIO, and (g), (h) NOESIO experiments. Left (Right) panels are for Ningaloo Niño (Niña). Contour interval is 0.6 mm day^{-1} and anomalies significant at 80% confidence levels by a two-tailed t-test are shaded.

be partly explained by positive skewness of Ningaloo Niño/Niña.

4.5 Conclusions

In this chapter, we have examined the atmospheric component of Ningaloo Niño/Niña for the first time with a series of AGCM experiments. When an AGCM is forced by SST anomalies only in the eastern South Indian Ocean (i.e. ESIO experiment), the model reproduced negative (positive) SLP anomalies associated with Ningaloo Niño (Niña) off the west coast of Australia. These SLP anomalies are an essential component of local amplification of Ningaloo Niño/Niña. In addition, when an AGCM is forced by SST anomalies outside of the eastern South Indian Ocean (i.e. NOESIO experiment), statistically significant SLP anomalies are generated for both Ningaloo Niño and Niña. The SLP anomaly pattern resembles that of the Matsuno-Gill type response. In our AGCM experiments, it is found that the latter remote effect is stronger than the former local effect.

We have also found that Ningaloo Niño (Niña) induces wet (dry) anomalies in the northwestern part of Australia. Although we could not isolate influences of Ningaloo Niño/Niña based on statistical analyses of observational precipitation data in Chapter 2, the present model experiment without SST anomalies outside of the eastern South Indian Ocean (i.e. ESIO experiment) clearly shows the sole influence from Ningaloo Niño/Niña. Since this region is vulnerable to rainfall variability (e.g. Turner and Asseng, 2005), understanding such extreme events is of great importance.

This study suggests that there may be two pathways that ENSO may influence Ningaloo Niño/Niña. As is already suggested by Feng et al. (2013) and Chapter 2, coastal waves originating from the western tropical Pacific associated with ENSO, so called the Clarke-Meyers effect (Clarke, 1991; Clarke and Liu, 1994; Meyers, 1996), play an important role. In addition to this oceanic connection, this chapter pointed out that the Matsuno-Gill

type response in the atmosphere can induce SLP anomalies that are favorable for the development of Ningaloo Niño/Niña. Although existence of this atmospheric connection is suggested by Feng et al. (2013) for a single event, this chapter is the first to show this connection in a composite view.

Chapter 5

Ningaloo Niño as a phenomenon independent of El Niño/Southern Oscillation

This chapter will be submitted as:

Kataoka, T., S. Masson, T. Izumo, T. Tozuka, and T. Yamagata, 2014: Ningaloo Niño as a phenomenon independent of El Niño/Southern Oscillation. *Clim. Dyn.*, (in preparation)

5.1 Introduction

As reviewed in Chapter 1, interannual oceanic variability off the western coast of Australia has long been considered mainly a response to tropical Pacific variability, especially El Niño/Southern Oscillation (ENSO) until quite recently (Pariwano et al., 1986; Wijffels and Meyers, 2003; Feng et al., 2008). However, we suggested in Chapter 2 that some Ningaloo Niño develops through an intrinsic unstable air-sea interaction off the west coast of Australia, called the coastal Bjerknes feedback: an anomalous low generated by positive SST anomalies forces northerly-alongshore wind anomalies, which cause coastal downwelling anomalies and further enhance the initial warm SST anomalies further. Our numerical model experiments in Chapters 3 and 4 support the above proposed mechanism based on the observation. We also showed that the enhanced warming by the climatological shortwave radiation due to shallower mixed layer contributes to the growth of SST anomalies (Chapter 3). Then, a simple question arises. Does Ningaloo Niño exist even without ENSO? Considering that Ningaloo Niño in 1982/83 and 2010/11 co-occurred respectively with very strong El Niño and La Niña (Chapter 2), the answer seems yes. However, as long as ENSO exists as it does in the real world, the ENSO influence including its delayed effects (e.g. Xie et al., 2009), which is nonlinear, cannot be completely removed. Therefore, the co-occurrence with both El Niño and La Niña is not the perfect answer to the particular question.

In this chapter, using a state-of-the-art coupled general circulation model (CGCM), we demonstrate that Ningaloo Niño exists even when the tropical Pacific interannual variability is suppressed. The rest of the chapter is organized as follows. Section 5.2 describes model simulations and observational and reanalysis datasets. In Section 5.3, main results are presented. Conclusions and discussions are given in the final section.

5.2 Model and data description

The CGCM used in this chapter is SINTEX-F2 (Masson et al., 2012). The atmospheric component is ECHAM 5.3 (Roeckner et al., 2003, 2004) with horizontal resolution of T106 and 31 hybrid sigma-pressure levels in the vertical. A cumulus convection scheme developed by Tiedtke (1989) and Nordeng (1994) is used. The oceanic component is NEMO (Madec, 2008) with the ORCA05 horizontal grid ($\sim$0.5°) and 31 vertical levels. LIM2 ice model (Timmermann et al., 2005) is also included in the coupled system. Two experiments are conducted here. In the control (CTRL) run, the ocean and atmosphere are freely coupled everywhere. On the other hand, in the noENSO run, the ocean and atmosphere are allowed to interact except over the tropical Pacific and the maritime continent, where SSTs are strongly restored to the smoothed daily climatology of the CTRL run. Both experiments are integrated for 110 years and a spin-up period of the first 10 years are discarded. The configuration of the noENSO run is identical to the FTPC run of Prodhomme et al. (2014), except for its longer duration. For comparison, we use (1) the Extended Reconstructed Sea Surface Temperature (ERSST) version 3b dataset (Smith et al., 2008) from 1950 to 2013, (2) the National Centers for Environmental Prediction/National Center for Atmospheric Research (NCEP/NCAR) reanalysis data (Kalnay et al., 1996) for sea level pressure (SLP) and wind at 10 m for 1950-2012, (3) the Global Precipitation Climatology Project (GPCP) data (Adler et al., 2003) for precipitation from 1979 to 2013, and (4) the sea surface height (SSH) derived from the Simple Ocean Data Assimilation (SODA) version 2.2.4 from (Carton and Giese, 2008) 1950 till 2008. Linear trends are removed from all the time series using a least-square fit. Then, to remove decadal variability (Kuhnert et al., 1999; Zinke et al., 2014), a Lanczos high-pass filter (Duchon, 1979) is applied except for the shorter GPCP dataset, with the first and last 5 years of each time series discarded to avoid edge effects. The response curve of

this filter retains 50% of the amplitude at 8-year period and 90% at 5-year period.

5.3 Results

5.3.1 CTRL run

To extract the dominant mode of variability off the western coast of Australia (105-120°E, 35-15°S), we have performed an empirical orthogonal function (EOF) analysis of SST anomalies (Figs. 5.1a,b). The CTRL run reproduces Ningaloo Niño well with a similar spatial pattern and amplitude compared to the observation. Following Chapter 2, the Ningaloo Niño index (NNI) is defined by area-averaged SST anomalies over the region 108°E - coast and 22-28°S. To check the model performance in Ningaloo Niño seasonality, the standard deviation of 3-month running averaged NNI is computed as a function of the calendar month (Fig. 5.1d). The model captures Ningaloo Niño seasonality well with a peak from January to March (JFM), though the variability is too weak in austral winter. Hereafter, Ningaloo Niño-developing year is denoted as year 0 and the following year as year 1.

To see both the temporal and spatial evolution of simulated Ningaloo Niño, a lead-lag regression analysis of SST anomalies onto the normalized JFM-mean NNI is performed on the model outputs along with observations (Figs. 5.2a,b). The model captures the SST evolution well; SST anomalies appear to the northwestward of Australia in austral spring and peak around summer, near the North West Cape.

Regarding the generation mechanism, SINTEX-F2 again reproduces observed features well. Coastal waves (Fig. 5.3d) are partly originating from the western Pacific (Clarke, 1991; Clarke and Liu, 1994; Meyers, 1996), though observed coastal waves from the tropical Pacific are modest compared to the CTRL run, and partly forced locally by alongshore wind as suggested by poleward strengthening of SSH anomalies. Negative SLP and

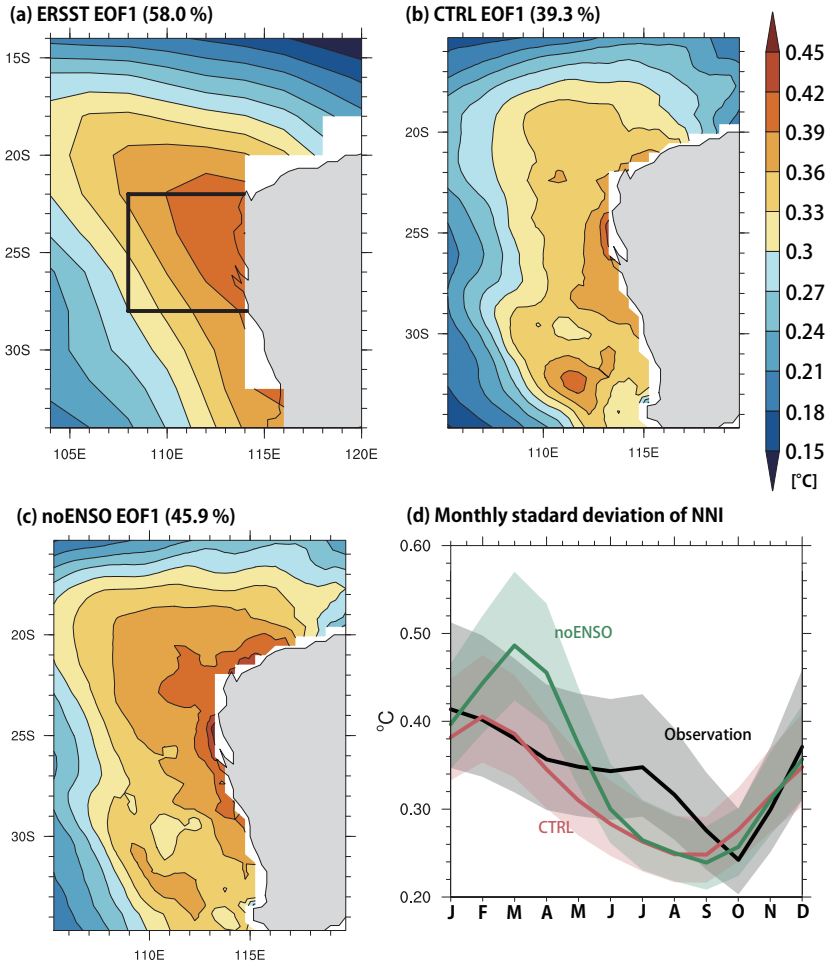

Fig. 5.1 First EOF mode of SST anomalies off Western Australia for (a) ERSST, (b) CTRL run, and (c) noENSO run. Slight difference in the domain for ERSST is due to its coarse resolution. Variance contribution is indicated on each panel. In panel (a), the domain used to calculate the NNI (108°E-coast, 28-22°S) is superimposed (black line). (d) Monthly standard deviation of the 3-month running averaged NNI (black: ERSST, red: CTRL run, and green: noENSO run). Shading represents 95% confidence interval.

alongshore-northerly wind anomalies off the western coast of Australia are also found (Figs. 5.3b,e). The model simulates the atmospheric circulation anomalies relatively well, although significant anomalies in the CTRL run have a broader pattern mainly due to their overestimation in December (0), with maxima slightly shifted eastward. These atmospheric anomalies may have both western tropical Pacific and local forcing origins (Chapter 4).

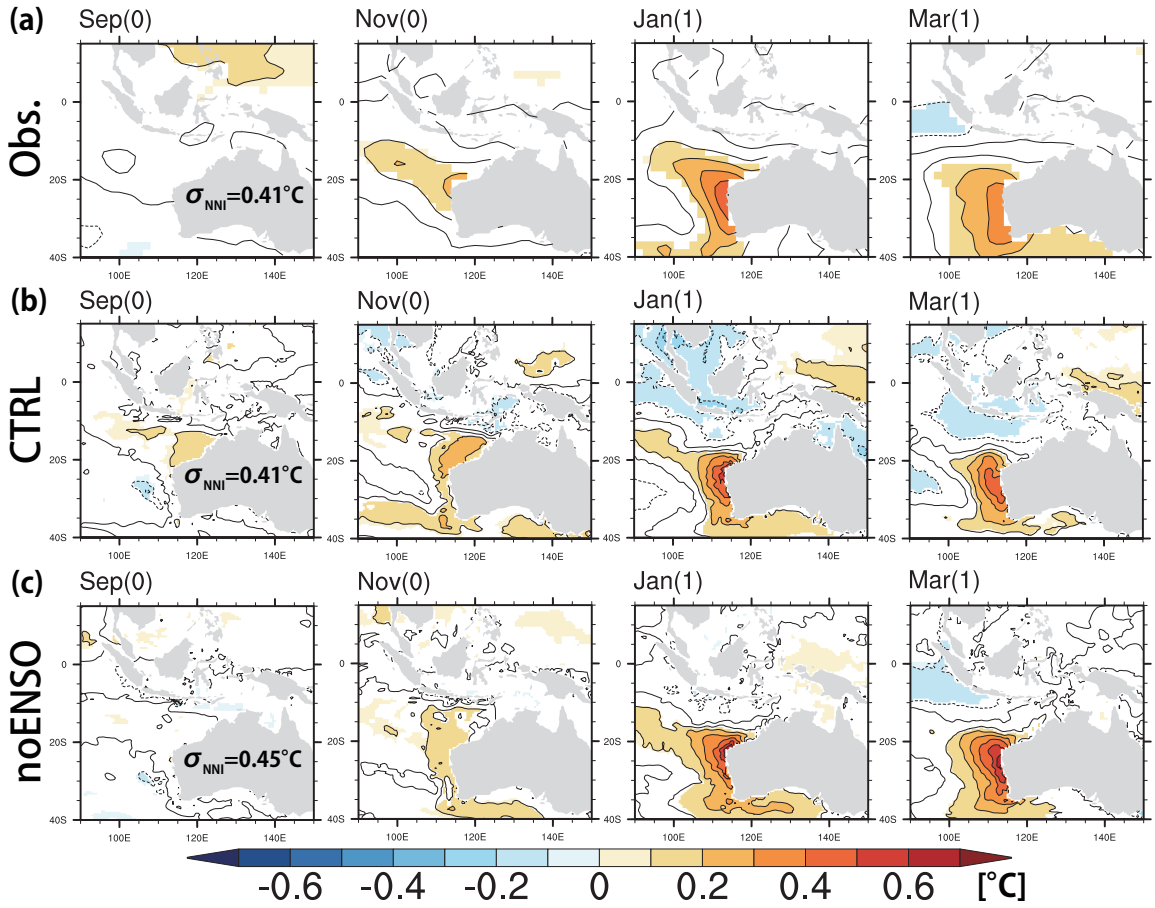

Fig. 5.2 Regressed anomalies of SST (in °C) onto the normalized JFM-mean NNI for (a) observation, (b) CTRL run, and (c) noENSO run. Results are shown every two months from September (0) to March (1). Contour intervals are 0.1°C. Regression coefficients exceeding 95% confidence level by a two-tailed t-test are shaded. The standard deviations used for the normalization are indicated on the panels for Sep(0).

5.3.2 noENSO run

Since the CTRL run well reproduces Ningaloo Niño, we expect that it can provide a useful insight into its aspect independent from ENSO. As for the CTRL run, an EOF analysis is conducted on SST anomalies of the noENSO experiment over the same region (Fig. 5.1c). It is found that Ningaloo Niño still exists and remains the dominant mode even without ENSO. Monthly standard deviation of the NNI for the noENSO run reveals

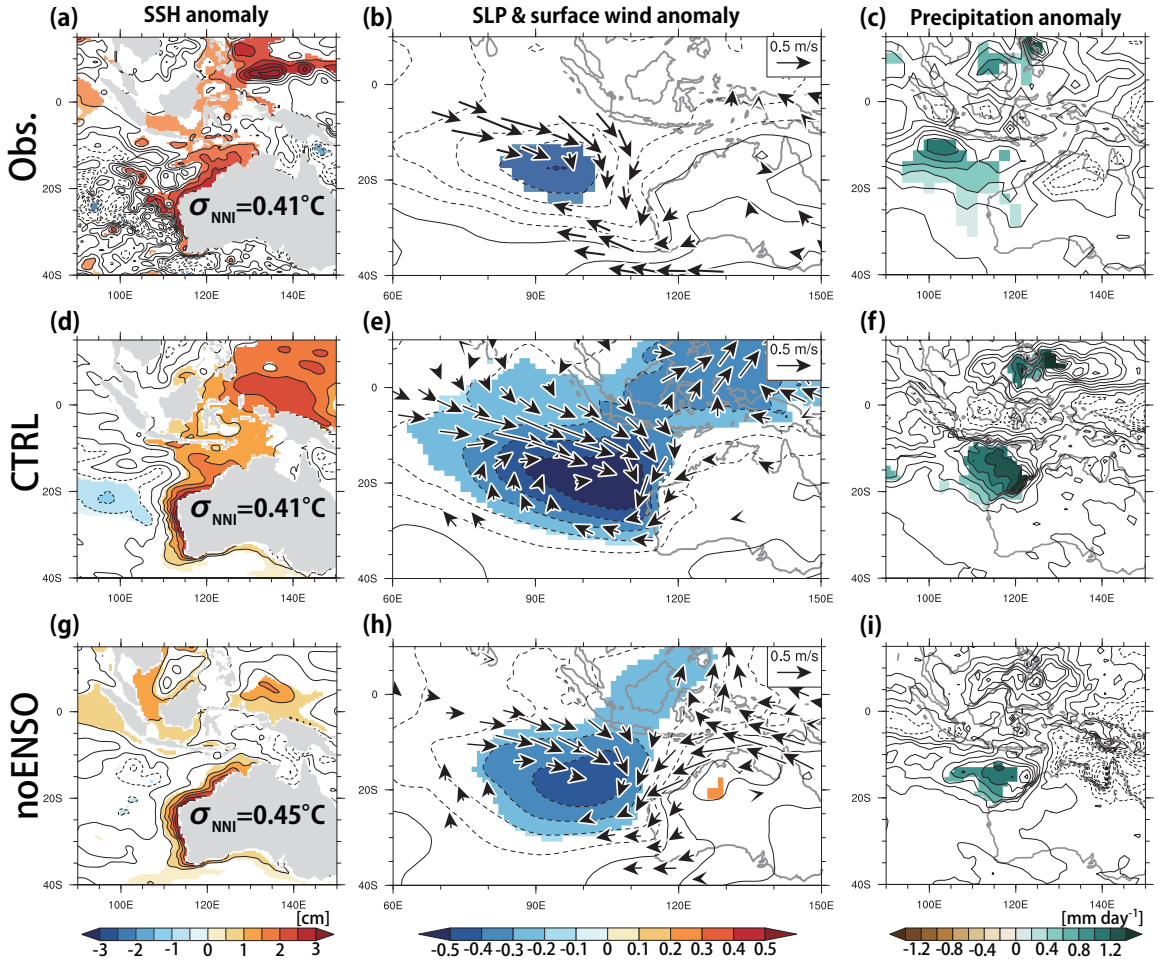

Fig. 5.3 DJF-averaged map for regression coefficients of observed (a) SSH (in cm), (b) standardized SLP and surface wind (in m/s), and (c) precipitation (mm/day) anomalies against JFM-mean NNI. SLP anomalies are normalized by standard deviations at each grid. (d-f) As in (a-c), but for the CTRL run. (g-i) As in (a-c), but for the noENSO run. Coefficients significant at 95% confidence level are shaded except for observed SSH and precipitation anomalies for which 90% confidence level is adopted. Vectors are drawn when zonal or meridional component is significant at 95%. The standard deviations used for the normalization are shown on the panels for SSH anomaly.

that its seasonal phase-locking nature is also unchanged (Fig. 5.1d). Although we see some difference in amplitude between CTRL and noENSO experiments, they are not significant at 95% confidence level; a brief consideration will be given later. The most important point here is that the amplitude of Ningaloo Niño is unlikely smaller without ENSO.

A lead-lag regression analysis of SST anomalies onto the normalized JFM-mean NNI reveals that Ningaloo Niño in the noENSO experiment is not just a transient signal, but it evolves with time as in the real world and the CTRL run. The same regression analysis but for other anomaly fields is also performed to look into the generation mechanism of Ningaloo Niño independent from ENSO. As expected, almost no significant coastal waves from the western Pacific are found in this experiment (Fig. 5.3g). Despite this absence of waves originating from the Pacific, positive SSH anomalies are seen along the coast, suggesting an oceanic dynamical response to local alongshore wind anomalies off Western Australia (Fig. 5.3h).

As in observations and the CTRL run, negative SLP anomalies are found in the noENSO run off the western coast of Australia around the peak phase (Fig. 5.3h). It is important to note that neither significant SST anomalies associated with some other climate modes nor atmospheric teleconnection that may contribute to the generation of atmospheric circulation anomalies related to Ningaloo Niño are found. Therefore, the negative SLP anomalies in the southeastern Indian Ocean may be generated by local positive SST anomalies through more active convection to the northwest of Australia. This is a consistent feature seen among the observation and the model experiments (Figs. 5.3c,f,i) and in agreement with the SST-forced atmospheric model experiments in Chapter 4. The anomalous low is accompanied by alongshore-northerly wind anomalies, which cause coastal downwelling anomalies as pointed above (Fig. 5.3h). These coastal downwelling anomalies may enhance the initial SST anomalies via stronger poleward flowing current (Clarke and Li, 2004). Thus, the coastal Bjerknes feedback seems to operate. In addition, the cyclonic wind anomalies that are against

the climatological anticyclonic wind result in shallower mixed layer, as pointed out in Chapter 3 (figure not shown). This leads to enhanced warming of the mixed layer by climatological shortwave radiation.

5.4 Conclusions and discussions

We have performed two CGCM experiments and demonstrated for the first time that Ningaloo Niño/Niña develops even without ENSO, through an intrinsic air-sea interaction off the west coast of Australia, called the coastal Bjerknes feedback. Local SST anomalies force more active convection to the northwest of Australia, which is accompanied by low SLP anomalies off Western Australia and alongshore-northerly wind anomalies. These alongshore wind anomalies feedback onto initial SST anomalies by causing coastal downwelling anomalies, possibly through stronger poleward flowing current. We note that changes in sensitivity to climatological shortwave radiation further enhance SST anomalies. In Chapter 2, we have suggested that Ningaloo Niño may be categorized into locally and non-locally amplified cases. For our CGCM experiments conducted in this chapter, both cases can occur in the CTRL run, but only the locally amplified case exists in the noENSO run.

We note that the amplitudes of Ningaloo Niño/Niña in March and April may become larger in the "no-ENSO world" according to the noENSO experiment. This may be because SLPs over Australia in early austral autumn are generally lower in the noENSO run (not shown) and the Australian summer monsoon last longer so that convective activity around Australia may be stronger, although the confidence level of the difference in SLP in March and April is somewhat low.

Although ENSO is considered as one of the important triggers of Ningaloo Niño/Niña, the model results suggest that there are other triggering processes that are not related to ENSO. Thus, it will be interesting to examine how Ningaloo Niño/Niña is triggered in the

noENSO experiment and when an event occurs independent of ENSO in the real world. One candidate is atmospheric internal variability; variations in strength/position of the South Indian Ocean anticyclone or the Madden-Julian Oscillation (Madden and Julian, 1971, 1972) that generate SST anomalies to the northwest of Australia (Vialard et al., 2013) may trigger an event.

Finally, it is important to note that the existence of Ningaloo Niño/Niña in the "no-ENSO world" does not mean that Ningaloo Niño/Niña is not related to ENSO. The ENSO-related coastal waves originating from the western tropical Pacific may trigger the locally amplified case and play a key role in the development of the non-locally amplified case. Also, as shown in Chapter 4, a Matsuno-Gill type response to convection anomalies linked with ENSO contributes to the development of Ningaloo Niño/Niña by generating SLP anomalies off the west coast of Australia.

Chapter 6

General conclusions

In this thesis, the growth and decay mechanisms of a recently identified regional climate phenomenon off Western Australia named "Ningaloo Niño" and its impact on precipitation over western Australia are investigated. Ningaloo Niña, the opposite phase of Ningaloo Niño, is introduced and examined as well. This chapter summarizes the main results obtained in each chapter and discusses their implications.

6.1 Summary

In Chapter 2, using both observational and reanalysis data, general characteristics of Ningaloo Niño (Niña) are obtained for the first time and we suggested the existence of the coastal Bjerknes feedback. Ningaloo Niño (Niña), which is associated with positive (negative) sea surface temperature (SST) anomalies and atmospheric anomalies off the western coast of Australia, peaks during austral summer and has significant impacts on the precipitation over Australia. Based on the difference in the local alongshore wind anomalies, it is classified into two cases. The first case called a "locally amplified case" develops through an intrinsic unstable air-sea interaction off the western coast of Australia; an anomalous cyclone (anticyclone) generated by positive (negative) SST anomalies forces northerly (southerly) alongshore wind anomalies, which induce coastal downwelling (upwelling) anomalies, and enhance the positive (negative) SST anomalies further. This newly identified positive feedback loop is named as the coastal Bjerknes feedback. The second case is a "non-locally amplified case", where coastally trapped waves originating from either the western tropical Pacific or the northern coast of Australia play an important role. The former origin is mostly related to El Niño/Southern Oscillation (ENSO).

Positive (negative) SST anomalies in both cases are associated with an anomalous low (high) off the western coast of Australia. The sea level pressure (SLP) anomalies in the locally amplified case are regionally confined with a cell-like pattern and produce a sharp

corss-shore pressure gradient along the western coast of Australia, whereas those in the non-locally amplified case tend to show a zonally elongated pattern. The difference is found to be related to the continental SLP modulated by the Australian summer monsoon. The introduction of the locally and non-locally amplified cases allowed us to find the existence of the local air-sea interaction.

In Chapter 3, using outputs from an ocean general circulation model (OGCM), the generation and decay mechanisms of Ningaloo Niño (Niña) suggested in Chapter 2 are investigated quantitatively by calculating mixed layer temperature (MLT) balance. For both cases of Ningaloo Niño, positive meridional advection anomalies associated with the stronger Leeuwin Current and enhanced warming by climatological shortwave radiation due to anomalously thin mixed layer contribute to the generation of SST anomalies in the near-shore region. Although the former is suggested to contribute to the development of a single event by a past study (Feng et al., 2013), the importance of the latter effect is pointed out for the first time. Negative sensible heat flux anomalies, on the other hand, play an important role in the decay. Since the strengthened meridional current during the developing season reduce meridional temperature gradient, meridional advection anomalies eventually change their sign and contribute to the decay as well. While the latent heat flux as a whole does not contribute much to the development of the locally amplified case, it cools the mixed layer in the non-locally amplified case. This is because, in the former case, the effect of reduced latent heat loss associated with decreased wind speed is mostly cancelled out by the effect of enhanced cooling by climatological latent heat loss due to shallower mixed layer, whereas no significant reduction in wind speed and thus latent heat loss are seen even though enhanced cooling by climatological latent heat loss is present in the latter case.

The MLT tendency anomalies in the offshore region during the development (decay) phase for both cases are dominated by enhanced (reduced) warming by the climatological shortwave radiation induced by mixed layer depth (MLD) anomalies.

The generation and decay mechanisms of both cases of Ningaloo Niña are close to a mirror image of those for Ningaloo Niño in general. In particular, negative meridional advection anomalies associated with weaker Leeuwin Current for the near-shore region, and suppressed warming by climatological shortwave radiation owing to anomalously thick mixed layer for the offshore region, play an important role, respectively.

Negative (Positive) SLP anomalies off the west coast of Australia are suggested as a key element of Ningaloo Niño (Niña) in Chapter 2. For this reason, generation mechanisms of atmospheric circulation anomalies accompanied by Ningaloo Niño/Niña are examined in Chapter 4 by conducting a series of numerical experiments with an atmospheric general circulation model (AGCM). Even when SST is allowed to vary interannually only in the eastern South Indian Ocean, negative (positive) SLP anomalies are formed off the west coast of Australia in Ningaloo Niño (Niña) years, supporting the existence of local ocean-atmosphere interaction suggested in Chapter 2. When the model is forced by SST anomalies outside of the eastern South Indian Ocean, negative (positive) SLP anomalies are also generated in Ningaloo Niño (Niña) years owing to a Matsuno-Gill type response to atmospheric convection anomalies in the tropical Pacific. Regarding climatic impacts, it is shown that Ningaloo Niño (Niña) induces wet (dry) anomalies over the northwestern part of Australia even when SST anomalies outside of the eastern South Indian Ocean are excluded from the SST forcing.

While the results obtained in the previous chapters suggest the existence of the intrinsic air-sea interaction off the western coast of Australia, the existence of ENSO-related forcing is also suggested. Thus, it was not clear whether Ningaloo Niño/Niña may develop without oceanic and atmospheric teleconnections from ENSO and solely by the local air-sea interaction. However, as long as ENSO exists, its influence cannot be completely excluded from the observational data, and thus, the co-occurrence of Ningaloo Niño with both El Niño and La Niña in the historical records cannot be a conclusive answer to the independence of

Ningaloo Niño from ENSO. In Chapter 5, therefore, aspects of Ningaloo Niño independent from ENSO are examined using a coupled ocean-atmosphere model. In a control experiment, Ningaloo Niño is realistically simulated including its magnitude and seasonality. In another experiment, where SSTs in the tropical Pacific and the maritime continent are strongly nudged toward their daily climatology in the control run to suppress ENSO, Ningaloo Niño still develops with the similar magnitude through an intrinsic air-sea interaction off Western Australia. This study is the first to show that Ningaloo Niño can develop even without ENSO.

6.2 Concluding remarks

The air-sea coupled feedback put forward in this thesis includes precipitation anomalies to the northwest of Australia, but SST and SLP anomalies associated with Ningaloo Niño/Niña extend to the mid-latitudes. Thus, fluctuations of seasonally strengthened subtropical high (e.g. Liu et al., 2004; Miyasaka and Nakamura, 2010) induced by anomalous land-sea thermal contrast may also contribute to the generation. However, the present GCMs and thus reanalysis data are not realistic enough to simulate complex interactions involving low-level clouds. The relationship between modulations of the subtropical high and Ningaloo Niño/Niña should be examined in the future.

The observational data analysis (Chapter 2) and AGCM experiments (Chapter 4) suggest that Ningaloo Niño/Niña influences precipitation over Western Australia. Thus, a successful prediction of this climate mode may be of great importance for regional industrial and societal activities. However, such a downscaled seasonal climate prediction is still quite challenging. One reason is that a high-resolution ocean component is required for the ocean-atmosphere coupled model to adequately resolve coastal waves and/or coastal upwelling/downwelling. As shown in the present thesis, the regional as well as coastal processes play a vital role in the development of Ningaloo Niño/Niña. As far as we know, no seasonal prediction

model is composed of such a high-resolution ocean model. Hendon and Wang (2010) attempted to predict the Leeuwin Current using a dynamical seasonal forecast model, but 2° resolution in the zonal direction was not sufficient to resolve the above costal processes and they had to use an empirical downscaling method to achieve some prediction skills. Also, the interannual variation in the monsoon system is very difficult to predict at the seasonal time-scale (e.g. Kulkarni et al., 2012). Since the interannual variations in the Australian monsoon regulate the alongshore wind anomalies during the development of Ningaloo Niño/Niña, this gives another reason for the difficulty. Furthermore, as shown in Chapter 3, the ocean mixed layer processes play a vital role in development of Ningaloo Niño/Niña and thus, accurate prediction of the MLD is crucial. However, the state-of-the-art of mixed layer parameterization is not sufficient (Watanabe and Hibiya, 2013) and further improvements are required.

Concerning the generation mechanism of MLD anomalies, since northerly-alongshore wind anomalies over the near-shore region are against the climatological southerlies during the locally amplified Ningaloo Niño, wind speed is reduced and thus turbulent mixing is suppressed. On the other hand, surface wind anomalies over the offshore region for both cases oppose the background southeasterly, suppressing wind-induced mixing. The reduction in wind speed is also favorable for the suppression of the latent heat loss and therefore, a shallower mixed layer. Moister air coming from the tropics may contribute to less evaporation as well. The generation mechanism of MLD anomalies needs to be examined quantitatively in the future study.

Associated with a longer climate trend, Xie et al. (2010) suggested that the tropical precipitation response to climate change has a spatial pattern in relation to relative SST to tropical mean. Although the domain of definition for the Leeuwin Current strength is somewhat south of the convection region, Sun et al. (2012) suggested that the Leeuwin Current and Indonesian Throughflow weaken under global warming, which may contribute

to the cooler southeastern tropical Indian Ocean relative to the tropical mean warming. In fact, multi-model ensemble mean projects a reduction of precipitation off Western Australia (Figure 12.10 of Collins et al. (2013)). Thus, under global warming, the coastal Bjerknes feedback off Western Australia might weaken, or even disappear in an extreme case.

Since there is a well-known similarity between equatorial and coastal processes as first discussed by Yoshida (1959), it may be interesting to compare Ningaloo Niño with El Niño in the tropical Pacific. Warm SST anomalies associated with Ningaloo Niño induce northerly-alongshore wind anomalies, which cause anomalous poleward current along the coastal waveguide and enhance the initial SST anomalies. This situation is more or less similar to that of El Niño evolution in that positive SST anomalies induce westerly surface wind anomalies, which result in eastward zonal current anomalies along the equatorial waveguide (Picaut and Delcroix, 1995; Picaut et al., 1996) and amplify the initial SST anomalies. However, there is a difference as well. Regarding the coupled instability of ENSO, Hirst (1986) suggested that oceanic Rossby waves are destabilized when horizontal advection by zonal current anomalies is dominant in SST anomaly generation (zonal advective feedback), whereas Kelvin waves are destabilized when SST growth is dominated by vertical processes associated with the local thermocline displacement (thermocline feedback). In this regard, El Niño and Ningaloo Niño evolution may look different because the situation in Ningaloo Niño is closer to the zonal advective feedback. However, it should be noted that previous studies which addressed the equatorial coupled instability through eigenvalue problem used very simple thermodynamic equations for the ocean. This simplification includes the neglect of MLD variations, which play an important role in Ningaloo Niño evolution by changing the sensitivity to the climatological shortwave radiation. Such a heat capacity variation effect due to MLD variation could operate in El Niño as well, given the prevailing easterly trade winds against westerly wind anomalies.

Finally, we note that similar warming/cooling events occur along the eastern boundary

of other subtropical ocean basins. Among others, Benguela Niño/Niña off the west coast of Angola and Namibia in southern Africa is also associated with large SST variability attached to the eastern boundary (Shannon et al., 1986). Several mechanisms have been proposed (Florenchie et al., 2003; Lübbecke et al., 2010; Richter et al., 2010), but its mechanism including its relation with Atlantic Niño (Merle, 1980) is still under debate. Although the background SST in the Benguela region is much colder and the strength of local air-sea interaction may be weaker, the present study may shed new light on the research of Benguela Niño/Niña and other similar phenomena such as recently identified California Niño/Niña (Yuan and Yamagata, 2014).

References

Adler, R. F., G. J. Huffman, A. Chang, R. Ferraro, P. Xie, J. Janowiak, B. Rudolf, U. Schneider, S. Curtis, D. Bolvin, A. Gruber, J. Susskind, and P. Arkin, 2003: The Version 2 Global Precipitation Climatology Project (GPCP) Monthly Precipitation Analysis (1979-Present). *J. Hydrometeor.*, **4**, 1147–1167.

Andrew, J. C., 1977: Eddy structure and the West Australian Current. *Deep-Sea Res.*, **24**, 1133–1148.

Ashok, K., Z. Guan, and T. Yamagata, 2003: Influence of the Indian Ocean Dipole on the Australian winter rainfall. *Geophys. Res. Lett.*, **30**, doi:10.1029/2003GL017926.

Behera, S. K., R. Krishnan, and T. Yamagata, 1999: Unusual ocean-atmosphere conditions in the tropical Indian Ocean during 1994. *Geophys. Res. Lett.*, **26**, 3001–3004.

Behera, S. K., J.-J. Luo, S. Masson, P. Delecluse, S. Gualdi, A. Navarra, and T. Yamagata, 2005: Paramount impact of the Indian Ocean Dipole on the East African short rains: A CGCM study. *J. Climate*, **18**, 4514–4530.

Behera, S. K., J.-J. Luo, S. Masson, S. A. Rao, H. Sakuma, and T. Yamagata, 2006: A CGCM study on the interaction between IOD and ENSO. *J. Climate*, **19**, 1688–1705.

Behera, S. K., J. V. Ratnam, Y. Masumoto, and T. Yamagata, 2013: Origin of extreme summers in Europe: the Indo-Pacific connection. *Clim. Dyn.*, **41**, 663–676.

Behringer, D. and Y. Xue, 2004: Evaluation of the global ocean data assimilation system at NCEP: The Pacific Ocean. *Eighth Symp. On Integrated Observing and Assimilation*

System for Atmosphere, Ocean, and Land Surface, Seattle, WA, Amer. Meteor. Soc., 2.3, [Available online at https://ams.confex.com/ams/pdfpapers/70720.pdf].

Bjerknes, J., 1969: Atmospheric teleconnections from the equatorial Pacific. *Mon. Wea. Rev.*, **97**, 163–172.

Cadet, D. L., 1985: The Southern Oscillation over the Indian Ocean. *J. Climate*, **5**, 189–212.

Caputi, N., W. J. Fletcher, A. Pearce, and C. F. Chubb, 1996: Effect of the Leeuwin Current on the recruitment of fish and invertebrates along the Western Australian coast. *Mar. Freshwater Res.*, **47**, 147–155.

Carton, J. A. and S. G. Giese, 2008: A reanalysis of ocean climate using Simple Ocean Data Assimilation (SODA). *Mon. Wea. Rev.*, **136**, 2999–3017.

Clarke, A. J., 1991: On the reflection and transmission of low-frequency energy at the irregular western Pacific Ocean boundary. *J. Geophys. Res.*, **96**, 3289–3305.

Clarke, A. J. and J. Li, 2004: El Niño/La Niña shelf edge flow and Australian western rock lobsters. *Geophys. Res. Lett.*, **31**, doi:10.1029/2003GL018900.

Clarke, A. J. and X. Liu, 1994: Interannual sea level in the northern and eastern Indian Ocean. *J. Phys. Oceanogr.*, **24**, 1224–1235.

Collins, M., R. Knutti, J. Arblaster, J.-L. Dufresne, T. Fichefet, P. Friedlingstein, X. Gao, W. J. Gutowski, T. Johns, G. Krinner, M. Shongwe, C. Tebaldi, A. J. Weaver, and M. Wehner, 2013: Long-term climate change: Projections, commitments and irreversibility. *Climate Change 2013: The Physical Science Basis. Contribution of Woring Group I to the Fifth Assessment Report of the Intergovernmental Panel on Climate Change*, T. F. Stocker, D. Qin, G.-K. Plattner, M. Tignor, S. K. Allen, J. Boschung, A. Nauels, Y. Xia, V. Bex, and P. M. Midgley, Eds., Cambridge University Press, Cambridge, United Kingdom and New York, NY, USA, 1029–1138.

Cresswell, G. R. and T. J. Golding, 1980: Observations of a south-flowing current in the southeastern Indian Ocean. *Deep-Sea Res.*, **27A**, 449–466.

Depczynski, M., J. P. Gilmour, T. Ridgway, H. Barnes, A. J. Heyward, T. H. Holmes, J. A. Y. Moore, B. T. Radford, D. P. Thomson, P. Tinkler, and S. K. Wilson, 2013: Bleaching, coral mortality and subsequent survivorship on a West Australian fringing reef. *Coral Reefs*, **32**, 233–238.

Doi, T., T. Tozuka, and T. Yamagata, 2010: The Atlantic Meridional Mode and its coupled variability with the Guinea Dome. *J. Climate*, **23**, 455–475.

Drosdowsky, W., 1996: Variability of the Australian summer monsoon at Darwin: 1957-1992. *J. Climate*, **9**, 85–96.

Duchon, C. E., 1979: Lanczos filtering in one and two dimensions. *J. Appl. Meteor.*, **18**, 1016–1022.

Ekman, V. W., 1905: On the influence of the Earth's rotation on ocean currents. *Ark. Mat. Astron. Fys.*, **2**, 1–53.

Emanuel, K., 1991: A scheme for representing cumulus convection in large-scale models. *J. Atmos. Sci.*, **48**, 2313–2335.

Feng, M., A. Biastoch, C. Böning, N. Caputi, and G. Meyers, 2008: Seasonal and interannual variations of upper ocean heat balance off the west coast of Australia. *J. Geophys. Res.*, **113**, doi:10.1029/2008JC004908.

Feng, M., M. J. McPhaden, S.-P. Xie, and J. Hafner, 2013: La Niña forces unprecedented Leeuwin Current warming in 2011. *Sci. Rep.*, **3**, 10.1038/srep01 277.

Feng, M., G. Meyers, A. Pearce, and S. Wijffels, 2003: Annual and interannual variations of the Leeuwin Current at 32°S. *J. Geophys. Res.*, **108**, doi:doi:10.1029/2002JC001763.

Florenchie, P., J. R. E. Lutjeharms, and C. J. C. Reason, 2003: The source of Benguela Niños in the South Atlantic Ocean. *Geophys. Res. Lett.*, **30**, doi:10.1029/2003GL017172.

Furue, R., J. P. McCreary, J. Benthuysen, H. E. Phillips, and N. L. Bindoff, 2013: Dynamics of the Leeuwin Current: Part 1. Coastal flows in an inviscid, variable-density, layer model. *Dyn. Atmos. Oceans*, **63**, 24–59.

Gill, A. E., 1980: Some simple solutions for heat-induced tropical circulation. *Q. J. R. Meteorol. Soc.*, **106**, 447–462.

Gill, A. E., 1983: An Estimation of sea-level and surface-current anomalies during the 1972 El Niño and consequent thermal effects. *J. Phys. Oceanogr.*, **13**, 586–606.

Gill, A. E., 1985: Elements of coupled ocean-atmosphere models for the tropics. *Coupled Ocean-Atmosphere Models*, J. C. J. Nihoul, Ed., Elsevier Science, Amsterdam, Elsevier Oceanography Series, Vol. 40, 303–327.

Goddard, L. and S. G. Philander, 2000: The energetics of El Niño and La Niña. *J. Climate*, **13**, 1496–1516.

Graham, N. E. and T. P. Barnett, 1987: Sea surface temperature, surface wind divergence, and convection over topical oceans. *Science*, **238**, 657–659.

Guan, Z., S. Iizuka, M. Chiba, S. Yamane, K. Ashok, M. Honda, and T. Yamagata, 2000: Frontier Atmospheric General Circulation Model version 1.0 (FrAM1.0): Model climatology. *Technical Report FTR-1*, 27pp.

Hendon, H. H. and B. Liebmann, 1990: A composite study of onset of the Australian summer monsoon. *J. Atmos. Sci.*, **47**, 2227–2240.

Hendon, H. H. and G. Wang, 2010: Seasonal prediction of the Leeuwin Current using POAMA dynamical seasonal forecast model. *Clim. Dyn.*, **34**, 1129–1137.

Hirst, A. C., 1986: Unstable and damped equatorial modes in simple coupled ocean-atmosphere models. *J. Atmos. Sci.*, **43**, 606–630.

Holland, G. J., 1986: Interannual variability of the Australian summer monsoon at Darwin: 1952-82. *Mon. Wea. Rev.*, **144**, 594–604.

Horii, T., Y. Masumoto, I. Umeki, H. Hase, and K. Mizumo, 2009: Mixed layer temperature balance in the eastern Indian Ocean during the 2006 Indian Ocean dipole. *J. Geophys. Res.*, **114**, doi:10.1029/2008JC005180.

Hung, C. W. and M. Yanai, 2004: Factors contributing to the onset of the Australian summer

monsoon. *Q. J. R. Meteorol. Soc.*, **130**, 739–758.

Hurrell, J. W., J. J. Hack, D. Shea, J. M. Caron, and J. Rosinski, 2008: Sea surface temperature and sea ice boundary dataset for the Community Atmosphere Model. *J. Climate*, **21**, 5145–5153.

Izumo, T., J. Vialard, M. Lengaigne, C. de Boyer Montegut, S. K. Behera, J.-J. Luo, S. Cravatte, S. Masson, and T. Yamagata, 2010: Influence of the state of the Indian Ocean Dipole on the following year's El Niño. *Nat. Geosci.*, **3**, 168–172.

Jerlov, N. G., 1976: *Marine Optics*. Elsevier, Amsterdam, Netherlands, 231pp pp.

Jin, F.-F., S. An, A. Timmermann, and J. Zhao, 2003: Strong El Niño events and nonlinear dynamical heating. *Geophys. Res. Lett.*, **30**, doi:doi:10.1029/2002GL016356.

Kajikawa, Y., B. Wang, and J. Yang, 2009: A multi-time scale Australian monsoon index. *Int. J. Climatol.*, **30**, 1114–1120.

Kalnay, E., M. Kanamitsu, R. Kistler, W. Collins, D. Deaven, L. Gandin, M. Iredell, S. Saha, G. White, J. Woollen, Y. Zhu, M. Chelliah, W. Ebisuzaki, W. H. J., Janowiak, K. C. Mo, C. Ropelewski, J. Wang, A. Leetmaa, R. Reynolds, R. Jenne, and D. Joseph, 1996: The NCEP/NCAR 40-year reanalysis project. *Bull. Am. Meteorol. Soc.*, **77**, 437–471.

Kara, A. B., P. A. Rochford, and H. E. Hurlburt, 2000: An optimal definition for ocean mixed layer depth. *J. Geophys. Res.*, **105**, 16 803–16 821.

Kataoka, T., T. Tozuka, Y. Masumoto, and T. Yamagata, 2012: The Indian Ocean subtropical dipole mode simulated in the CMIP3 models. *Clim. Dyn.*, **39**, 1385–1399.

Klein, S., B. J. Soden, and N.-C. Lau, 1999: Remote sea surface temperature variations during ENSO: Evidence for a tropical atmospheric bridge. *J. Climate*, **12**, 917–932.

Kosaka, Y., S.-P. Xie, N.-C. Lau, and G. A. Vecchi, 2013: Origin of seasonal predictability for summer climate over the Northwestern Pacific. *Proc. Natl. Acad. Sci. (USA)*, **110**, 7574–7579.

Kuhnert, H., J. Pätzold, B. Hatcher, K.-H. Wyrwoll, A. Eisenhauer, L. B. Collins, Z. R. Zhu,

and G. Wefer, 1999: A 200-year coral stable oxygen isotope record from a high-latitude reef off Western Australia. *Coral Reefs*, **18**, 1–12.

Kulkarni, N. A. M. A., S. C. Kar, U. C. Mohanty, M. K. Tippett, A. W. Robertson, J.-J. Luo, and T. Yamagata, 2012: Probabilistic prediction of Indian summer monsoon rainfall using global climate models. *Theor. Appl. Climatol.*, **107**, 441–450.

Kullgren, K. and K. Y. Kim, 2006: Physical mechanisms of the Australian summer monsoon: 1. Seasonal cycle. *J. Geophys. Res.*, **111**, doi:10.1029/2005JD006807.

Kundu, P. K. and J. P. McCreary, 1986: On the dyanmics of the Troughflow from the Pacific into the Indian Ocean. *J. Phys. Oceanogr.*, **16**, 2191–2198.

Legates, D. R. and C. J. Willmott, 1990: Mean seasonal variability in gauge-corrected, global precipitation. *J. Climate*, **10**, 111–127.

Levitus, S. and T. P. Boyer, 1994: World Ocean Atlas, Vol. 4: Temperature. *NOAA Atlas NESDIS 4*, 117pp.

Levitus, S., R. Burgett, and T. P. Boyer, 1994: World Ocean Atlas, Vol. 3: Salinity. *NOAA Atlas NESDIS 3*, 99pp.

Liu, Y., G. Wu, and R. Ren, 2004: Relationship between the subtropical anticyclone and diabatic heating. *J. Climate*, **17**, 682–698.

Lübbecke, J. F., C. W. Böning, N. S. Keenlyside, and S.-P. Xie, 2010: On the connection between Benguela and equatorial Atlantic Niños and the role of the South Atlantic anticyclone. *J. Geophys. Res.*, **115**, doi:10.1029/2009JC005964.

Lukas, R., T. Yamagata, and J. P. McCreary, 1996: Pacific low-latitude western boundary currents and the Indonesian throughflow. *J. Geophys. Res.*, **101**, 12 209–12 216.

Madden, R. A. and P. R. Julian, 1971: Detections of a 40-50 day oscillation in the tropics. *J. Atmos. Sci.*, **28**, 702–708.

Madden, R. A. and P. R. Julian, 1972: Description of global scale circulation cells in the tropics with a 40-50 day period. *J. Atmos. Sci.*, **29**, 1109–1123.

Madec, G., 2008: NEMO ocean engine. *Note du Pole de modelisation*, institut Pierre-Simon Laplace (IPSL) No 27, ISSN No 1288-1619.

Marshall, A. G. and H. H. Hendon, 2014: Impacts of the MJO in the Indian Ocean and on the Western Australian coast. *Clim. Dyn.*, **42**, 579–595.

Masson, S., P. Terray, G. Madec, J.-J. Luo, T. Yamagata, and K. Takahashi, 2012: Impact of intra-daily SST variability on ENSO characteristics in a coupled model. *Clim. Dyn.*, **39**, 681–707.

Masumoto, Y. and T. Yamagata, 1996: Seasonal variations of the Indonesian throughflow in a general ocean circulation model. *J. Geophys. Res.*, **101**, 12 287–12 293.

Matsuno, T., 1966: Quasi- geostrophic motions in the equatorial area. *J. Meteorol. Soc. Jpn.*, **44**, 479–494.

McCreary, J. P., S. R. Shetye, and P. K. Kundu, 1986: Thermohaline forcing of eastern boundary currents: With application to the circulation off the west coast of Australia. *J. Mar. Res.*, **44**, 71–92.

Menezes, V. V., H. E. Phillips, A. Schiller, and C. M. Domingues, 2013: Salinity dominance on the Indian Ocean Eastern Gyral Current. *Geophys. Res. Lett.*, **40**, 5716–5721.

Merle, J., 1980: Variabilité thermique annuelle et interannuelle de l'océan Atlantique équatorial Est. L'hypothése d'un "El Niño" Atlantique. *Oceanol. Acta*, **3**, 209–220.

Meyers, G., 1996: Variation of the Indonesian throughflow and the El Niño Southern Oscillation. *J. Geophys. Res.*, **101**, 12 255–12 263.

Miyasaka, T. and H. Nakamura, 2010: Structure and mechanism of the Southern Hemisphere summertime subtropical anticylones. *J. Climate*, **23**, 2115–2130.

Morioka, Y., T. Tozuka, and T. Yamagata, 2010: Climate variability in the southern Indian Ocean as revealed by self-organizing maps. *Clim. Dyn.*, **35**, 1059–1072.

Morioka, Y., T. Tozuka, and T. Yamagata, 2011: On the growth and decay of the subtropical dipole mode in the South Atlantic. *J. Climate*, **24**, 5538–5554.

Nigam, S. and H.-S. Shen, 1993: Structure of oceanic and atmospheric low-frequency variability over the tropical Pacific and Indian Oceans. Part I: COADS observations. *J. Climate*, **6**, 657–676.

Nitta, T., 1987: Convective activities in the tropical western Pacific and their impact on the Northern Hemisphere summer circulation. *J. Meteorol. Soc. Jpn.*, **65**, 373–390.

Nordeng, T. E., 1994: Extended versions of the convective parameterization scheme at ECMWF and their impact on the means and transient activity of the model in the tropics. *ECMWF Research Department, Tech. Memo*, **206**, 41pp, European Centre for Medium Range Weather Forecasts.

North, G. R., T. L. Bell, R. F. Cahalan, and F. J. Moeng, 1982: Sampling errors in the estimation of empirical orthogonal functions. *Mon. Wea. Rev.*, **110**, 699–706.

Ogata, T. and S.-P. Xie, 2011: Semiannual Cycle in zonal wind over the equatorial Indian Ocean. *J. Climate*, **24**, 6471–6485.

Pacanowski, R. C. and S. M. Griffies, 1999: *MOM 3.0 manual*. NOAA/GFDL.

Pacanowski, R. C. and S. G. H. Philander, 1981: Parameterization of vertical mixing in numerical models of tropical oceans. *J. Phys. Oceanogr.*, **11**, 1443–1451.

Palmer, T. N., G. J. Shutts, and R. Swinbank, 1986: Alleviation of systematic westerly bias in general circulation and numerical weather prediction models through an orographic gravity wave drag parameterization. *Q. J. R. Meteorol. Soc.*, **112**, 1001–1039.

Pariwano, J. I., J. A. Bye, and G. W. Lennon, 1986: Long-period variations of sea-level in Australia. *Geophys. J. R. Astron.*, **87**, 43–54.

Paulson, C. A. and J. J. Simpson, 1977: Irradiance measurements in the upper ocean. *J. Phys. Oceanogr.*, **7**, 952–956.

Pearce, A. F. and M. Feng, 2013: The rise and fall of the "marine heat wave" off Western Australia during the summer of 2010/2011. *J. Mar. Syst.*, **111-112**, 139–156.

Philander, S. G. H., T. Yamagata, and R. C. Pacanowski, 1984: Unstable air-sea interaction

in the tropics. *J. Atmos. Sci.*, **41**, 604–613.

Picaut, J. and T. Delcroix, 1995: Equatorial wave sequence associated with warm pool displacements during the 1986-1989 El Niño-La Niña. *J. Geophys. Res.*, **100**, 18 393–18 408.

Picaut, J., M. Ioualalen, C. Menkes, T. Delcroix, and M. J. McPhaden, 1996: Mechanism of the zonal displacements of the Pacific Warm Pool: Implications for ENSO. *Science*, **274**, 1486–1489.

Prodhomme, C., P. Terray, S. Masson, B. G., and T. Izumo, 2014: Oceanic factors controlling the Indian summer monsoon onset in a coupled model. *Clim. Dyn.*, doi:10.1007/s00382-014-2200-y, in press.

Rasmusson, E. M. and T. H. Carpenter, 1982: Variations in tropical sea surface temperature and surface wind fields associated with the Southern Oscillation/El Niño. *Mon. Wea. Rev.*, **110**, 354–384.

Reason, C. J. C., R. J. Allan, J. A. Lindesay, and T. J. Ansell, 2000: ENSO and climatic signals across the Indian Ocean basin in the global context: part I, interannual composite patterns. *Int. J. Climatol.*, **20**, 1285–1327.

Reynolds, R. W., N. A. Rayner, T. M. Smith, D. C. Stokes, and W. Wang, 2002: An improved in situ and satellite SST analysis for climate. *J. Climate*, **15**, 1609–1625.

Richter, I., S. K. Behera, Y. Masumoto, B. Taguchi, N. Komori, and T. Yamagata, 2010: On the triggering of Benguela Niños: Remote equatorial versus local influences. *Geophys. Res. Lett.*, **37**, doi:10.1029/2010GL044461.

Ridgway, K. R., J. R. Dunn, and J. L. Wilkin, 2002: Ocean interpolation by four-dimensional weighted least squares-Application to the waters around Australia. *J. Atmos. Oceanic Technol.*, **19**, 1357–1375.

Roeckner, E., G. Bäuml, L. Bonaventura, R. Brokopf, M. Esch, M. Giorgetta, S. Hagemann, I. Kirchner, L. Kornblueh, E. Manzini, A. Rhodin, U. Schlese, U. Schulzweida, and

A. Tompkins, 2003: The atmospheric general circulation model ECHAM 5, Part I, Model description. Tech. Rep. Report No. 349, Max Planck Institute for Meteorology, Hamburg.

Roeckner, E., R. Brokopf, M. Esch, M. Giorgetta, S. Hagemann, L. Kornblueh, E. Manzini, U. Schlese, and U. Schulzweida, 2004: The atmospheric general circulation model ECHAM 5, Part II, Sensitivity of simulated climate to horizontal and vertical resolution. Tech. Rep. Report No. 354, Max Planck Institute for Meteorology, Hamburg.

Saji, N. H., B. N. Goswami, P. N. Vinayachandran, and T. Yamagata, 1999: A dipole mode in the tropical Indian Ocean. *Nature*, **401**, 360–363.

Saji, N. H. and T. Yamagata, 2003a: Possible impacts of Indian Ocean Dipole mode events on global climate. *Clim. Res.*, **25**, 151–169.

Saji, N. H. and T. Yamagata, 2003b: Structure of SST and surface wind variability during Indian Ocean Dipole mode events: COADS observations. *J. Climate*, **13**, 2735–2751.

Schneider, U., A. Becker, P. Finger, A. Meyer-Christoffer, B. Rudolf, and M. Ziese, 2011: GPCC full data reanalysis version 6.0 at 1.0°S: Monthly land-surface precipitation from rain-gauges built on GTS-based and historic data. doi:10.5676/DWD_GPCC/FD_M_V6_100.

Schott, F. A., S.-P. Xie, and J. P. McCreary, 2009: Indian Ocean circulation and climate variability. *Rev. Geophys.*, **47**, doi:10.1029/2007RG000245.

Shannon, L. V., A. J. Boyd, G. B. Brundrit, and J. Taunton-Clark, 1986: On the existence of an El Niño-type phenomenon in the Benguela system. *J. Mar. Res.*, **44**, 495–520.

Smagorinsky, J., 1963: General circulation experiments with the primitive equations. Part I: The basic experiment. *Mon. Wea. Rev.*, **91**, 99–164.

Smith, R. L., A. Huyer, J. S. Godfrey, and J. A. Church, 1991: The Leeuwin Current off Western Australia, 1986-1987. *J. Phys. Oceanogr.*, **21**, 323–345.

Smith, T. M., R. W. Reynolds, T. C. Peterson, and J. Lawrimore, 2008: Improvements to NOAA's historical merged land-ocean surface temperature analysis (1880-2006). *J.*

Climate, **21**, 2283–2296.

Sprintall, J., A. L. Gordon, A. Koch-Larrouy, T. Lee, J. T. Potemra, K. Pujiana, and S. E. Wijffels, 2014: The Indonesian seas and their role in the coupled ocean-climate system. *Nat. Geosci.*, **7**, 487–492.

Sprintall, J., S. E. Wijffels, R. Molcard, and I. Jaya, 2009: Direct estimates of the Indonesian Tthroughflow entering the Indian Ocean: 2004-2006. *J. Geophys. Res.*, **114**, doi:10.1029/2008JC005257.

Sun, C., M. Feng, R. J. Matear, M. A. Chamberlain, P. Craig, K. R. Ridgway, and A. Schiller, 2012: Marine downscaling of a future climate scenario for Australian boundary currents. *J. Climate*, **25**, 2947–1962.

Suzuki, R., S. K. Behera, S. Iizuka, and T. Yamagata, 2004: Indian Ocean subtropical dipole simulated using a coupled general circulation model. *J. Geophys. Res.*, **109**, doi:10.1029/2003JC001974.

Sverdrup, H. U., 1947: Wind-driven currents in a baroclinic ocean, with application to the equatorial currents of the eastern Pacific. *Proc. Natl. Acad. Sci. (USA)*, **22**, 318–326.

Thompson, R. O. R. Y., 1984: Observations of the Leeuwin Current off Western Australia. *J. Phys. Oceanogr.*, **14**, 623–628.

Tiedtke, M., 1989: A comprehensive mass flux scheme for cumulus parameterization in large-scale models. *Mon. Wea. Rev.*, **117**, 1779–1800.

Timmermann, R., H. Goosse, G. Madec, T. Fichefet, C. Ethe, and V. Duliere, 2005: On the representation of high latitude processes in the ORCA-LIM global coupled sea ice-ocean model. *Ocean Modell.*, **8**, 175–201.

Tozuka, T., B. J. Abiodun, and F. A. Engelbrecht, 2014: Impacts of convection schemes on simulating tropical-temperate troughs over southern Africa. *Clim. Dyn.*, **42**, 433–451.

Tozuka, T., T. Doi, T. Miyasaka, N. Keenlyside, and T. Yamagata, 2011: Key factors in simulating the equatorial Atlantic zonal SST gradient in a coupled GCM. *J. Geophys. Res.*,

116, 10.1029/2010JC006 717.

Tozuka, T., T. Miyasaka, A. Chakraborty, M. Mujumdar, S. K. Behera, Y. Masumoto, H. Nakamura, and T. Yamagata, 2006: University of Tokyo Coupled General Circulation Model (UTCM1.0). *Ocean-Atmos. Res. Rep.*, **7**, 44pp.

Turner, N. C. and S. Asseng, 2005: Productivity, sustainability, and rainfall-use efficiency in Australian rainfed Mediterranean agricultural systems. *Aus. J. Agric. Res.*, **56**, 1123–1136.

Uppala, S. M., P. Kallberg, A. Simmons, U. Andrae, V. da Costa Bechtold, M. Fiorino, J. Gibson, J. Haseler, A. Hernandez, G. Kelly, X. Li, K. Onogi, S. Saarinen, N. Sokka, R. Allan, E. Andersson, K. Arpe, M. Balmaseda, A. Beljaars, L. van de Berg, J. Bidlot, N. Bormann, S. Caires, F. Chevallier, A. Dethof, M. Dragosavac, M. Fisher, M. Fuentes, S. Hagemann, E. Holm, B. Hoskins, L. Isaksen, P. Janssen, R. Jenne, A. McNally, J.-F. Mahfouf, J.-J. Morcrette, N. Rayner, R. Saunders, P. Simon, A. Sterl, K. Trenberth, A. Untch, D. Vasiljevic, P. Viterbo, and J. Woollen, 2005: The ERA-40 re-analysis. *Q. J. R. Meteorol. Soc.*, **131**, 2961–3012.

Vialard, J. and P. Delecluse, 1998: An OGCM study for the TOGA decade. Part I: Role of salinity in the Physics of the western Pacific fresh pool. *J. Phys. Oceanogr.*, **28**, 1071–1088.

Vialard, J., K. Drushka, H. Bellenger, M. Lengaigne, S. Pous, and J. P. Duvel, 2013: Understanding Madden-Julian-induced sea surface temperature variations in the north western Australian Basin. *Clim. Dyn.*, **41**, 3203–3218.

Viterbo, P. and A. C. M. Beljaars, 1995: An improved land surface parameterization scheme in the ECMWF model and its validation. *Res. Dep. Tech. Rep.*, **75**.

Watanabe, M. and T. Hibiya, 2013: Assessment of mixed layer models embedded in an ocean general circulation model. *J. Oceanogr.*, **69**, 329–338.

Weaver, A. J. and J. H. Middleton, 1989: On the dynamics of the Leeuwin Current. *J. Phys. Oceanogr.*, **19**, 626–648.

Webster, P. J., A. M. Moore, J. P. Loschnigg, and R. R. Leben, 1999: Coupled

ocean-atmosphere dynamics in the Indian Ocean during 1997-98. *Nature*, **401**, 356–360.

Wernberg, T., D. A. Smale, F. Tuya, M. S. Thomsen, T. J. Langlois, T. de Bettignies, S. Bennett, and C. S. Rousseaux, 2012: An extreme climatic event alters marine ecosystem structure in a global biodiversity hotspot. *Nat. Clim. Change*, **3**, 78–82.

Wijffels, S. and G. Meyers, 2003: An intersection of oceanic waveguides: Variability in the Indonesian Throughflow region. *J. Phys. Oceanogr.*, **34**, 1232–1253.

Xie, P. and P. A. Arkin, 1997: Global precipitation: A 17-year monthly analysis based on gauge observations, satellite estimates and numerical model outputs. *Bull. Am. Meteorol. Soc.*, **78**, 2539–2558.

Xie, S.-P., C. Deser, G. A. Vecchi, J. Ma, H. Teng, and A. T. Wittenberg, 2010: Global warming pattern formation: sea surface temperature and rainfall. *J. Climate*, **23**, 966–986.

Xie, S.-P., K. Hu, J. Hafner, H. Tokinaga, Y. Du, G. Huang, and T. Sampe, 2009: Indian Ocean capacitor effect on Indo-Western Pacific climate during the summer following El Niño. *J. Climate*, **22**, 730–747.

Yamagami, Y. and T. Tozuka, 2014: Interdecadal changes of the Indian Ocean subtropical dipole mode. *Clim. Dyn.*, doi:10.1007/s00382-014-2202-9, in press.

Yamagata, T., 1985: Stability of a simple air-sea coupled model in the tropics. *Coupled Ocean-Atmosphere Models*, J. C. J. Nihoul, Ed., Elsevier Science, Amsterdam, Elsevier Oceanography Series, Vol. 40, 637–657.

Yamagata, T., S. K. Behera, J.-J. Luo, S. Masson, M. R. Jury, and S. A. Rao, 2004: Coupled ocean-atmosphere variability in the tropical Indian Ocean. *Earth's Climate: The Ocean-Atmosphere Interaction*, C. Wang, S.-P. Xie, and J. A. Carton, Eds., American Geophysical Union, Washigton DC, USA, Geophys. Monographs, Vol. 147, 189–211.

Yamagata, T., S. K. Behera, S. A. Rao, and H. N. Saji, 2003: Comments on "Dipoles, temperature gradients, and tropical climate anomalies". *Bull. Am. Meteorol. Soc.*, **84**, 1418–1422.

Yang, J., Q. Liu, S.-P. Xie, Z. Liu, and L. Wu, 2007: Impact of the Indian Ocean SST basin mode on the Asian summer monsoon. *Geophys. Res. Lett.*, **34**, doi:10.1029/2006GL028571.

Yoshida, K., 1959: A theory of the Cromwell Current (the equatorial undercurrent) and of the equatorial upwelling -An interpretation in a similarity to a coastal circulation-. *J. Oceanogr. Soc. Japan*, **15**, 159–170.

Yu, L., S. Jin, and R. A. Weller, 2008: Multidecade global flux datasets from the Objectively Analyzed Air-Sea Fluxes (OAFlux) Project: Latent and sensible heat fluxes, ocean evaporation, and related surface meteorological variables. *Woods Hole Oceanographic Institution OAFlux Project Tech. Rep. OA-2008-01*, 64pp.

Yuan, C., T. Tozuka, and T. Yamagata, 2012: IOD Influence on the early winter Tibetan Plateau snow cover: Diagnostic analyses and an AGCM simulation. *Clim. Dyn.*, **39**, 1643–1660.

Yuan, C. and T. Yamagata, 2014: California Niño/Niña. *Sci. Rep.*, **4**, doi:10.1038/srep04801.

Zinke, J., A. Rountrey, M. Feng, S.-P. Xie, D. Dissard, K. Rankenburg, J. M. Lough, and M. T. McCulloch, 2014: Corals record long-term Leeuwin current variability including Ningaloo Niño/Niña since 1795. *Nat. Comm.*, **5**, doi:10.1038/ncomms4607.

Zubair, L., S. A. Rao, and T. Yamagata, 2003: Modulation of Sri Lankan Maha rainfall by the Indian Ocean Dipole. *Geophys. Res. Lett.*, **30**, doi:10.1029/2002GL015639.